Earth Observing System

Multi-angle Imaging Spectro- Radiometer

Level 2 Ancillary Products and Datasets Algorithm Theoretical Basis

David J. Diner[1]
Wedad A. Abdou[1]
Howard R. Gordon[2]
Ralph A. Kahn[1]
Yuri Knyazikhin[3]
John V. Martonchik[1]
Duncan McDonald[1]
Stuart McMuldroch[1]
Ranga Myneni[3]
Robert A. West[1]

[1]Jet Propulsion Laboratory, California Institute of Technology
[2]University of Miami
[3]Boston University

JPL

Jet Propulsion Laboratory
California Institute of Technology

December 1, 1999

JPL D-13402, Rev. B

Multi-angle Imaging SpectroRadiometer (MISR)

Level 2 Ancillary Products and Datasets Algorithm Theoretical Basis

Approval:

David J. Diner

MISR Principal Investigator

The MISR web site should be consulted to determine the latest released version
of this document (http://www-misr.jpl.nasa.gov).
Approval signatures are on file with the MISR Project.

JPL

Jet Propulsion Laboratory
California Institute of Technology

TABLE OF CONTENTS

GLOSSARY OF ACRONYMS

A

ACP (Aerosol Climatology Product)
AGP (Ancillary Geographic Product)
ATB (Algorithm Theoretical Basis)
AVHRR (Advanced Very High Resolution Radiometer)
AZM (Azimuthal Model)

B

BOA (Bottom-of-Atmosphere)
BRF (Bidirectional Reflectance Factor)

D

DAAC (Distributed Active Archive Center)
DAO (Data Assimilation Office)
DDV (Dense Dark Vegetation)
DEM (Digital Elevation Model)
DID (DEM Intermediate Dataset)

E

EOS (Earth Observing System)

G

GSFC (Goddard Space Flight Center)

I

IAMAP (International Association for Meteorology and Atmospheric Physics)
IR (Infrared)
ISCCP (International Satellite Cloud Climatology Project)

J

JPL (Jet Propulsion Laboratory)

L

LBID (Land Biome Intermediate Dataset)
LUT (Look-up Table)

M

MISR (Multi-angle Imaging SpectroRadiometer)

N

NDVI (Normalized Difference Vegetation Index)
NSIDC (National Snow and Ice Data Center)

R

RH (Relative Humidity)
RT (Radiative Transfer)

S

SAGE (Stratospheric Aerosol and Gas Experiment)
SCF (Science Computing Facility)
SeaWiFS (Sea-viewing, Wide-Field-of-View Sensor)
SMART (Simulated MISR Ancillary Radiative Transfer)
SOM (Space Oblique Mercator)

T

TASC (Terrestrial Atmosphere and Surface Climatology)
TOA (Top-of-Atmosphere)
TOAC (Tropical Ocean Atmospheric Correction)
TOMS (Total Ozone Mapping Spectrometer)

W

WCP (World Climate Programme)
WGS (World Geodetic System)

1.   INTRODUCTION

1.1 PURPOSE

This Algorithm Theoretical Basis (ATB) document describes the algorithms used to generate the parameters of certain ancillary products and datasets used during Level 2 processing of Multi-angle Imaging SpectroRadiometer (MISR) data. These ancillary products and datasets are summarized in Table 1. In particular, this document identifies sources of input data, both MISR and non-MISR, and provides the physical theory and mathematical background underlying the usage of this information in deriving the parameters.

Table 1: Level 2 Ancillary Products and Datasets

Product/Dataset name	Contents
Terrestrial Atmosphere and Surface Climatology (TASC) Dataset	• Standard values of meteorological variables, ozone abundances, and snow/ice cover to be used as defaults during data processing if data from external sources are unavailable
Aerosol Climatology Product (ACP)	• Aerosol model size distributions, refractive indices, scattering and extinction coefficients, scattering phase functions, particle densities, particle shape and hygroscopic model parameters • Definition of aerosol mixtures to be used during retrievals and information to be used during retrievals • Climatological likelihood indicators for each model
Simulated MISR Ancillary Radiative Transfer (SMART) Dataset	• Top-of-atmosphere equivalent reflectances, downwelling irradiances, atmospheric transmission and backscatter data for the aerosol models to be used during Level 2 retrievals
Tropical Ocean Atmospheric Correction (TOAC) Dataset	• Atmospheric model information to be used for ocean color retrieval
Ancillary Land Biome (ALB) Dataset	• Canopy Architecture Radiative Transfer (CART) file contains radiative transfer parameters associated with biome-dependent complex canopy/soil models used in the retrieval of LAI/FPAR with the primary algorithm • NDVI-FPAR Regression Coefficients file used in retrieval of FPAR with the default algorithm • Biome Classification Map file contains biome type of each 1.1-km subregion of the land surface into one of six categories, for use during retrieval of FPAR with default algorithm

1.2 SCOPE

This document covers the algorithm theoretical basis for the parameters to be included in certain Level 2 ancillary products and datasets in the at-launch time frame. These products and datasets are to be generated at the MISR Science Computing Facility (SCF), and then delivered to the DAAC for use during routine processing of MISR data. The theoretical basis for the Azimuthal Model (AZM) Dataset, used during Level 2 processing for generation of the albedo parameters of

the TOA/Cloud Product, is described in *[M-10]*.

Chapter 1 describes the purpose and scope of the document. Chapter 2 is concerned with the TASC Dataset, Chapter 3 with the ACP, Chapter 4 with the SMART Dataset, Chapter 5 with the TOAC Dataset, and Chapter 6 with the ALB Dataset. References to publications cited in the text are provided in Chapter 7. Within the text, these references are indicated by a number in italicized square brackets, e.g., *[1]*.

1.3   MISR DOCUMENTS

References to MISR Project and reference documents are indicated by a number in italicized square brackets as follows, e.g., *[M-1]*. The MISR web site (http://www-misr.jpl.nasa.gov) should be consulted to determine the latest released version of each of these documents.

[M-1] Experiment Overview, JPL D-13407.

[M-2] Data Product Description, JPL D-11103.

[M-3] Level 1 Radiance Scaling and Conditioning Algorithm Theoretical Basis, JPL D-11507.

[M-4] Level 1 Georectification and Registration Algorithm Theoretical Basis, JPL D-11532.

[M-5] Level 1 Cloud Detection Algorithm Theoretical Basis, JPL D-13397.

[M-6] Level 1 In-flight Radiometric Calibration and Characterization Algorithm Theoretical Basis, JPL D-13398.

[M-7] Level 1 Ancillary Geographic Product Algorithm Theoretical Basis, JPL D-13400.

[M-8] Level 1 In-flight Geometric Calibration Algorithm Theoretical Basis, JPL D-13399.

[M-9] Level 2 Cloud Detection and Classification Algorithm Theoretical Basis, JPL D-11399.

[M-10] Level 2 Top-of-Atmosphere Albedo Algorithm Theoretical Basis, JPL D-13401.

[M-11] Level 2 Aerosol Retrieval Algorithm Theoretical Basis, JPL D-11400.

[M-12] Level 2 Surface Retrieval Algorithm Theoretical Basis, JPL D-11401.

[M-13] Algorithm Development Plan, JPL D-11220.

[M-14] In-flight Radiometric Calibration and Characterization Plan, JPL D-13315.

[M-15] In-flight Geometric Calibration Plan, JPL D-13228.

[M-16] Science Data Validation Plan, JPL D-12626.

[M-17] Science Data Processing Sizing Estimates, JPL D-12569.

1.4 TERMINOLOGY

The following terms are used within this document:

Standard Product: A product generated routinely at the DAAC.

Ancillary Dataset: A dataset generated at the SCF and delivered to the DAAC for use as input during routine processing. Ancillary Datasets may be updated either on a regular or sporadic basis at the SCF and new versions delivered to the DAAC, or in some cases, automated updating may occur at the DAAC. Ancillary Datasets are not required by users of MISR data to interpret the contents of Standard Products.

Ancillary Product: A product generated at the SCF and delivered to the DAAC for use during routine processing or as a supportive product necessary for the interpretation of Standard Products. Ancillary Products may be updated either on a regular or sporadic basis at the SCF and new versions delivered to the DAAC. Ancillary Products are distinguished from Ancillary Datasets in that they are needed by users of MISR data to interpret the contents of Standard Products.

Parameter: A variable contained within a product or dataset.

1.5 PROCESSING FLOW CONVENTIONS

Processing flow concepts are shown diagrammatically throughout the document. The convention for the various elements displayed in these diagrams is shown in Figure 1.

○ Input   ⊘ Intermediate Dataset   ● Output

☐ Process*   ***Numbers next to process boxes refer to sections in the text describing the algorithm**

◇ Decision or Branch
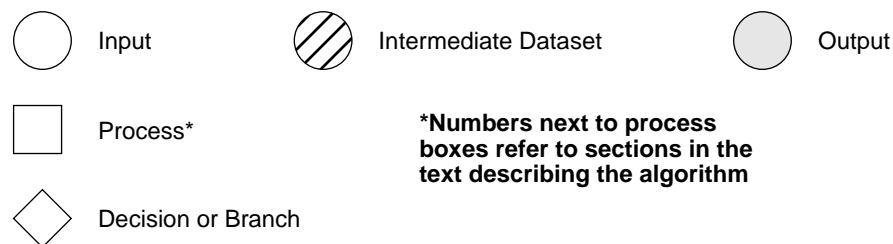
Figure 1. Conventions used in processing flow diagrams

1.6 EXPERIMENT OVERVIEW

An overview of the MISR science objectives, instrument, calibration approach, and data products, is provided in *[M-1]*.

1.7 ALGORITHM VALIDATION

Details on planned field campaigns, experimental methodologies, and instrument calibration and data reduction procedures are documented in *[M-16]*.

1.8 ALGORITHM DEVELOPMENT SCHEDULE

A strategy for time-phased development of the algorithms for the products and datasets described in this document, and a listing of key development milestones, are provided in *[M-13]*.

1.9 PRACTICAL CONSIDERATIONS

Requirements on data processing and storage are described in *[M-17]*. Software guidelines to be followed during algorithm development are described in *[M-13]*.

1.10 REVISIONS

The original version of this document was dated August 15, 1996. This version is Revision A. Changes from the original document are indicated through the use of change bars, as shown at the left.

2. TERRESTRIAL ATMOSPHERE AND SURFACE CLIMATOLOGY DATASET

2.1 PURPOSE

The Level 2 Terrestrial Atmosphere and Surface Climatology (TASC) Dataset consists of monthly and spatially-dependent climatological variables needed by various algorithms during routine processing. These parameters are used as default inputs to the Level 2 TOA/Cloud and Aerosol/Surface retrievals (see *[M-9], [M-10], [M-11], [M-12]*). The TASC Dataset will be used when measured meteorological and surface data are unavailable.

2.2 CONTENTS

Table 2 gives a detailed description of the TASC Dataset. It will be stored on a cylindrical equal angle grid. During routine processing, values obtained from the TASC will access the nearest bin value, i.e., no interpolation will be used. The grid is comprised of a set of bins measuring 1.0° in latitude and longitude (64,800 bins), and in monthly intervals representing an average value for the month. The mean surface altitude above sea level, z_0, is reported. The surface level referred to in the following table corresponds to this altitude. Atmospheric temperature is given as vertical profiles, as a function of altitude, z, above sea level. The vertical grid has a spacing of 0.5 km from sea level to 20 km altitude. For heights above 20 km, the value of atmospheric temperature at 25 km altitude is used. Thus, there are 42 values of z at which $T(z)$ is reported.

Table 2: Contents of the TASC Dataset

Parameter	Description	Units
z_0	Mean surface altitude	km
U	Climatological surface wind speed (zonal)	m sec^{-1}
V	Climatological surface wind speed (meridional)	m sec^{-1}
w	Climatological column precipitable water above surface level	cm
P_0	Climatological atmospheric surface pressure	hPa
T_0	Climatological atmospheric surface temperature	K
$T(z)$	Climatological atmospheric temperature vs. height profile	K
C_{O_3}	Climatological column ozone abundance	Dobsons
H_t	Climatological tropopause height	km
H_{hc}	Climatological high-cloud height	km
SI	Climatological snow/ice cover mask	none

The climatological high-cloud height is established to be equal to 80% of the climatological tropopause height. The justification for this is based on a study by Dowling and Radke *[16]* who show that cirrus cloud-center heights typically occur at an altitude of 70 - 80% of the tropopause height anywhere on Earth. Additionally, a study by Baum et al. *[4]* shows that high cloud altitudes in the International Satellite Cloud Climatology Project (ISCCP) database are biased low, making them unreliable for deriving a high cloud climatology. Should a different strategy for setting the climatological high-cloud height be adopted in the future, this field of the TASC Dataset will be replaced with the updated values.

2.3   PROCESSING OUTLINE

Figure 2 shows conceptually the processes involved in the generation of the TASC Dataset.
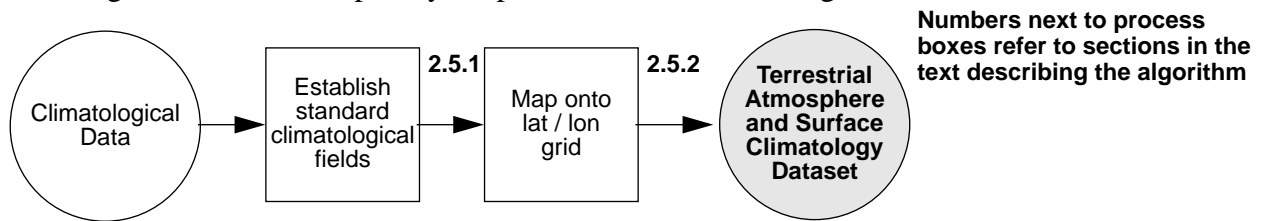
Figure 2. Conceptual processing flow for generation of the TASC Dataset

2.4   INPUT DATA

Parameters will be acquired from various sources, including the EOS Data Assimilation Office (DAO), the GSFC DAAC (for TOMS ozone data), the National Snow and Ice Data Center (NSIDC), and other sources.

2.5   THEORETICAL BASIS

2.5.1   Establish standard climatological fields

This step involves identifying the sources of input data, and determining the spatial and temporal averaging to be applied prior to mapping onto the MISR grid.

2.5.2   Map onto latitude/longitude grid

This step involves a resampling and binning of the appropriate parameters onto the cylindrical grid.

3. AEROSOL CLIMATOLOGY PRODUCT

3.1 PURPOSE

The Aerosol Climatology Product consists of three parts:

(1) *Aerosol physical and optical properties file*: This contains the microphysical and scattering characteristics of the pure aerosol models upon which the routine retrievals are based. The physical properties (size distribution, index of refraction, and tendency to adsorb water) are based upon current knowledge. The effective optical properties are calculated using Mie theory for spherical particles, and ellipsoid approximations/geometric optics for non-spherical cases, for a range of relative humidities. Size statistics and indices of refraction are calculated, and optical properties are reported for all MISR bands.

(2) *Aerosol mixture file*: During routine aerosol retrievals at the DAAC, it is necessary to establish the mixtures of pure aerosols included in the ACP that will be compared to the MISR observations. For each region of the globe, the ACP defines those mixtures, for each of the retrieval pathways that may occur (i.e., dark water, DDV, or heterogeneous land).

(3) *Aerosol "clim-likely" file*: It is possible that more than one of these models may meet the retrieval convergence criteria for a given region. Thus, the third purpose of the ACP is to assign a likelihood value to each of the selected aerosol models, based on reasonable climatological expectations. As such, it will provide a mechanism for finding anomalous conditions, which may indicate the discovery of unexpected aerosol distributions, or limitations of the algorithm.

3.2 CONTENTS

The present compilation of the individual (i.e., "pure") aerosol components to be contained in the ACP is presented in Table 3. Each pure particle type has a single composition (given by the indices of refraction), and a single size distribution (log-normal or power law with specified size parameters). Accumulation and coarse mode refer to physical mechanisms generally associated with the formation of particles of specified composition and size range. Nucleation mode particles are not included as the small size of the particles results in very low extinction cross sections relative to the accumulation and coarse modes under natural conditions, and thus are expected to have a negligible effect on the radiances as observed by MISR. The particles in Table 3 were selected because they are among the most common, and they capture a significant range of the variability of particle properties observed in the atmosphere. The indices of refraction shown are for all MISR bands. The column labeled RH is the relative humidity at which the properties shown in the table are reported. The treatment of relative humidity is discussed in the next section. The degree to which particles hydrate with increasing RH is based on Hanel *[24]*.

Table 3: Pure particle types in the ACP

Aerosol	r_1 (µm)	r_2 (µm)	r_c (µm)	σ	α	n_r (band)	n_i (band)	ξ (g/cm³)	RH (%)	Vary with RH?	h_b (km)	h_t (km)	h_s (km)	Shape
Sulfate/nitrate 1 (Accum.)	0.007	0.7	0.07	1.86	n/a	1.53 (all)	0.0 (all)	1.7	0	Yes	0	15	2	Spheres
Sulfate/nitrate 2 (Accum.)	0.05	2.0	0.45	1.30	n/a	1.43 (all)	0.0 (all)	1.7	0.3	No	15	30	10	Spheres
Mineral dust 1 (Accum.)	0.47	0.47	0.47	1.00	n/a	1.53 (all)	0.0085 (1) 0.0055 (2) 0.0045 (3) 0.0012 (4)	2.6	0	No	0	5	2	Prolate/ oblate spheroids
Mineral dust 2 (Accum.)											5	10	10	
Mineral dust (Coarse)	0.5	15.0	1.90	2.60							0	2	10	
Sea salt (Accum.)	0.05	1.0	0.35	2.51	n/a	1.50 (all)	0.0 (all)	2.2	0	Yes	0	5	2	Spheres
Sea salt (Coarse)	1.0	20.0	3.30	2.03							0	2	10	
Black carbon	0.001	0.5	0.012	2.00	n/a	1.75 (all)	0.455 (1) 0.440 (2) 0.435 (3) 0.430 (4)	2.3	0	No	0	8	10	Spheres
Carbonaceous particles	0.007	2.0	0.13	1.80	n/a	1.43 (all)	0.0035 (all)	1.8	97	No	0	5	2	Spheres
Near-surface fog	0.5	50.0	n/a	n/a	2.5	1.33 (all)	0.0 (all)	1.0	100	No	0	1	10	Spheres
Thin cirrus	3.0	200.0	see text	see text	see text	1.316 (1) 1.311 (2) 1.308 (3) 1.304 (4)	1.91e-9 (1) 3.11e-9 (2) 1.89e-8 (3) 2.15e-7 (4)	1.0	100	No	10	11	10	Fractal

Table 3 is an attempt at putting together a general-purpose global set of most common aerosol types. Under natural conditions, there will be exceptions to this baseline, and that the MISR instrument may have greater sensitivity to some particle types than others. We plan to revise this Table after launch in order to optimize the climatology to the actual performance of the instrument.

All aerosols in Table 3 are modeled using a log-normal particle size distribution, except for near-surface fog, which follows a power law. Both types of distributions are characterized by minimum and maximum radius (r_1, r_2). The log-normal size distribution is also parameterized by the characteristic radius (r_c) and characteristic width (σ), defined in Eqs. (6) and (7), whereas the power-law distribution is parameterized by an exponent (α) defined by Eq. (9). The cirrus size distribution is based on cirrostratus observations *[73]*. All aerosol particles are assumed spherical, except for mineral dust, which is modeled as randomly oriented prolate and oblate spheroids with a uniform distribution of aspect ratios between 1.2 and 2.4 *[47]*, and thin cirrus, which employs a fractal model. Carbonaceous (also referred to as biomass burning) particles are hygroscopic, but the humidity conditions near fires vary on length scales short compared to the MISR instrument resolution. Thus, for these particles we do not vary the properties as a function of RH as is done for the other hygroscopic particles; instead, we fix the values of index of refraction at the values shown in Table 3, which are for 97% RH, and use radius values that favor particles away from the source *[56]*. The particles denoted as sulfate/nitrate 1 are typical of those found in the troposphere. The particles denoted sulfate/nitrate 2 are adopted as the "standard" stratospheric particle type, and are assumed to have a size distribution in equilibrium with the ambient humidity values of the stratosphere *[79]*. Table 3 also provides real and imaginary refractive indices (n_r, n_i) and particle densities (ξ).

Each pure particle is also characterized by vertical distribution information, captured by three parameters: h_b, the base height of the aerosol layer; h_t, the top height of the aerosol layer; and h_s, the scale height of the layer. Values for these are also provided in Table 3.

During retrievals, mixtures of these pure particles are generated and compared to the MISR observations. The rules used to obtain the properties of mixtures from those of the pure particle types are given in §3.5.3 and §3.5.4. The aerosol mixture file in the ACP contains data for the entire suite of mixtures to be included in the retrievals. The relative abundances of each component of the mixtures are defined in terms of fraction of total optical depth (*not* by numbers of particles). As part of the tabulation of aerosol mixtures, the retrieval pathway indicator is a bit flag that establishes whether the particular aerosol mixture is to be used for dark water and/or DDV and/or heterogeneous land retrievals.

Table 4 shows the suite of tropospheric mixtures to be used in the ACP. The relative abundances, expressed as percentages of the total aerosol extinction optical depth, are wavelength and relative humidity dependent, due to the dependence of extinction cross section on wavelength and RH. Thus, the entries in Table 4 are for band 2 and RH = 70% as the reference. To generate the

data contained in the ACP, the relative abundances are converted to other wavelengths and relative humidities using the extinction cross sections contained in the aerosol physical and optical properties file. Note that in some MISR documentation, the carbonaceous particles are referred to as biomass burning particles, and black carbon is referred to as soot.

Table 4: Tropospheric particle mixtures contained in the ACP

Conditions	Components	Minimum relative abundance	Maximum relative abundance
Clean maritime	Sulfate mode 1	10%	80%
	Sea salt accumulation	10%	80%
	Sea salt coarse	0%	20%
Industrial maritime	Sulfate mode 1	10%	80%
	Sea salt accumulation	10%	80%
	Black carbon	10%	20%
Carbonaceous maritime	Sulfate mode 1	10%	70%
	Sea salt accumulation	10%	70%
	Carbonaceous	20%	80%
Dusty maritime	Sulfate mode 1	10%	70%
	Sea salt accumulation	10%	70%
	Mineral dust accumulation 2	20%	60%
Clean continental	Sulfate mode 1	10%	90%
	Mineral dust accumulation 1	10%	80%
	Black carbon	0%	10%
Industrial continental	Sulfate mode 1	10%	70%
	Mineral dust accumulation 1	0%	70%
	Black carbon	20%	40%
Carbonaceous continental	Sulfate mode 1	10%	70%
	Mineral dust accumulation 1	10%	70%
	Carbonaceous	20%	80%
Dusty continental	Sulfate mode 1	10%	80%
	Mineral dust accumulation 2	10%	80%
	Mineral dust coarse	10%	20%

The third part of the ACP provides climatological likelihoods of each aerosol mixture, stored on a cylindrical equal angle grid. The grid is set to 1.0° in latitude and longitude (64,800 bins), and provides climatological likelihoods in monthly intervals. These climatological likelihood values range from 0 to 3, with a value of 0 indicating that it would be very surprising to see a particular compositional mixture in the region at that season, whereas a value of 3 would indicate that the occurrence would be commonplace. In each region, the value of the likelihood is based on an assessment of the available data (AVHRR ocean aerosol retrievals, global and mesoscale aerosol modeling, and in situ aerosol measurements). The quality of the available data will vary greatly from region to region, and a quality indicator, ranging from 0 (good) to 3 (poor) is included.

The detailed contents of the ACP are provided in Table 5. Within the aerosol physical and optical properties file, each aerosol (including tropospheric, stratospheric, and cirrus) is identified by a single model number (m), corresponding to a "pure" particle type. "Effective" properties, where indicated, refer to averages weighted by the particle cross sectional areas and the size distribution function.

Table 5: Contents of the ACP

Parameter	Description	Units
Aerosol physical and optical properties file		
Model identifiers		
name	Aerosol pure particle name, which is unique for each particle composition/size distribution, relative humidity, and atmospheric layer identifier	none
m	Aerosol pure particle model number	none
m_{wa}	Water activity model number	none
ihygro	Indicates whether the particle hydrates as atmospheric relative humidity increases. For particles that hydrate, a particular model for water activity is specified	none
ishape	Particle shape parameter (spherical, polyhedral, prolate/oblate spheroidal, or fractal)	none
RH	Relative humidity (decimal fraction 0.0 for particles that do not hydrate; 0.7, 0.8, 0.9, 0.99 for particles that hydrate)	none
Particle size distribution parameters, vertical distribution parameters, and other physical properties		
m_{sd}	Size distribution model identifier (log-normal or power-law)	none

11

Table 5: Contents of the ACP (continued)

Parameter	Description	Units
r_1	Smallest particle radius in the particle size distribution to be considered	μm
r_2	Largest particle radius in the particle size distribution to be considered	μm
r_c	Characteristic radius for log-normal size distributions	μm
σ	Characteristic width of the log-normal particle size distribution (fill value used if not applicable)	μm
α	Exponent of the power-law size distribution (fill value used if not applicable)	none
$<r>$	Arithmetic mean particle radius	μm
G	Mean geometric cross sectional area per particle, weighted by the particle size distribution	$μm^2$
V	Mean volume per particle, weighted by the particle size distribution	$μm^3$
r_{eff}	Effective particle radius = $(3/4)(V/G)$	μm
v_{eff}	Effective variance of the size distribution	μm
r_{vw}	Volume-weighted mean particle radius	μm
ξ	Aerosol particle density	$g\ cm^{-3}$
h_b	Aerosol layer base height	km
h_t	Aerosol layer top height	km
h_s	Aerosol layer scale height	km
Optical properties		
n_r	Index of refraction (real part), weighted by the size distribution, at 4 MISR wavelengths	none
n_i	Index of refraction (imaginary part), weighted by the size distribution, at 4 MISR wavelengths	none
k_{sca}	Effective scattering cross section at 4 MISR wavelengths	$μm^2$
k_{ext}	Effective extinction cross section at 4 MISR wavelengths	$μm^2$
ω	Effective single scattering albedo at 4 MISR wavelengths	none

12

Table 5: Contents of the ACP (continued)

Parameter	Description	Units
g	Effective scattering anisotropy parameter at 4 MISR wavelengths	none
$p(\Omega)$	Effective scattering phase function on a fixed grid at 205 scattering angles (Ω), ranging from 0 to 180°, at 4 MISR wavelengths	sr^{-1}
Aerosol mixture file		
mix	Model number of the aerosol mixture	none
m_1, m_2, m_3	Aerosol pure particle model identifiers for up to 3 components in the aerosol mixture	none
f_1, f_2, f_3	Relative abundances (as fractions of total optical depth) of the 3 aerosol components, specified in each spectral band	none
τ_1, τ_3, τ_4	Optical depth of the mixture in MISR bands 1, 3, and 4, when the optical depth in band 2 equals unity	none
ϖ_{mix}	Single-scattering albedo of the aerosol mixture, specified in each spectral band	none
path	Retrieval pathway indicator flag	none
Aerosol "clim-likely" file (on cylindrical equal angle grid)		
mix	Model number of the aerosol mixture	none
τ_{555}	Climatological column optical depth at 555 nm	
CL	Climatological likelihood of the aerosol mixture, month-by-month (values range from 0 to 3)	none
DQ	Confidence level for the climatological likelihoods (values range from 0 to 3)	none

3.3 PROCESSING OUTLINE

The ACP is generated pre-launch at the MISR SCF and delivered to the DAAC. Figure 3 shows conceptually the processes involved in its generation.
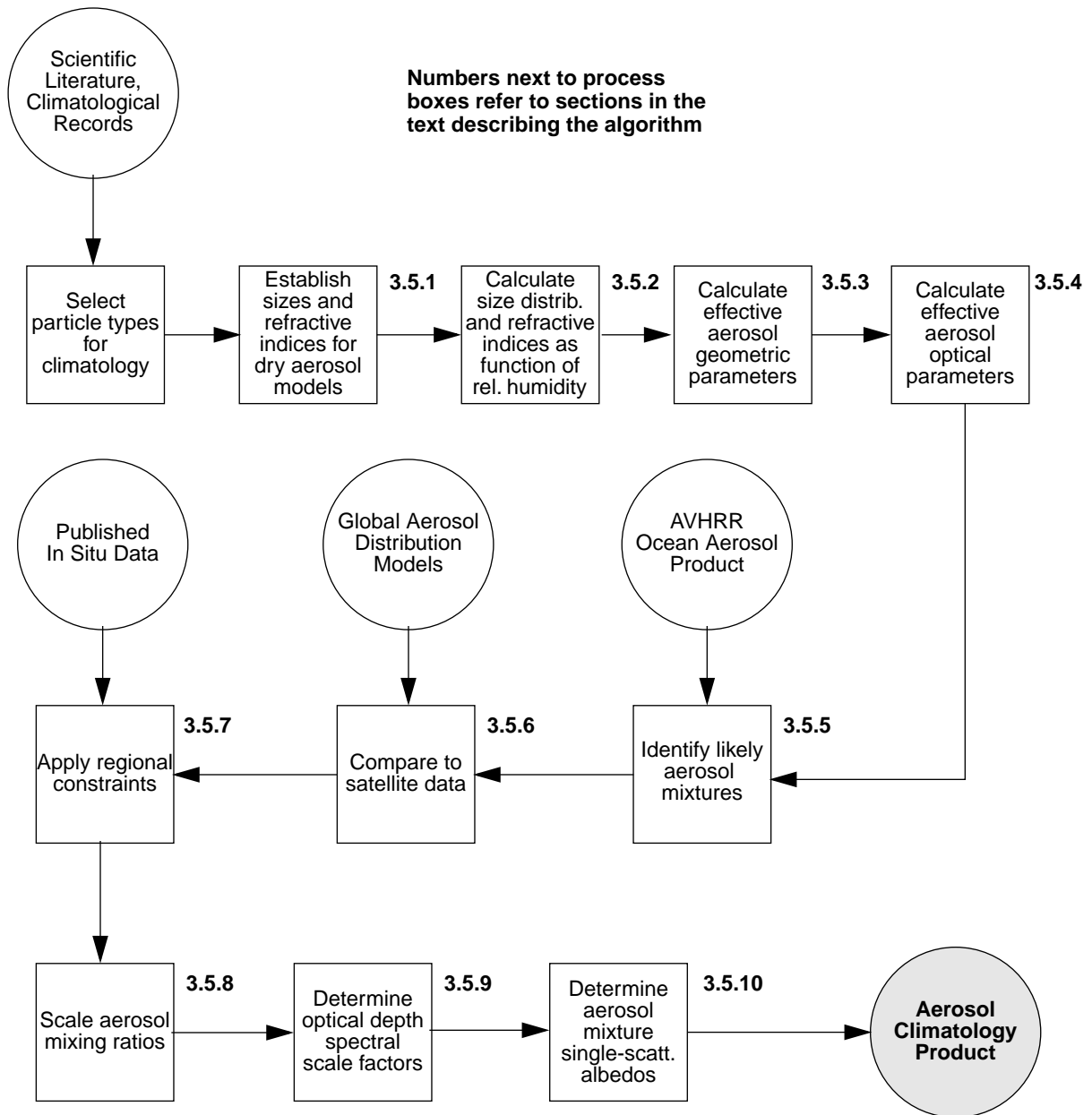
Figure 3. Conceptual processing flow for generation of the ACP

3.4 INPUT DATA

Input data for the aerosol physical and optical properties file within the ACP are primarily obtained from the scientific literature. Cirrus particle single-scattering properties were calculated by Takano and Liou *[73]* (see also *[44]*). The near-surface fog properties are taken from Pruppacker and Klett *[61]*, and the particle size distribution is modeled by a power-law function (e.g., *[25]*), with $\alpha = 2.5$ [see Eq. (9)]. The properties of the carbonaceous particles are from *[17]*. Mode 2 sulfates are based on analysis of SAGE II data *[79]*. Mineral dust optical properties come from the

14

work of Mishchenko et al. *[47]*. For the other particle types in the ACP, data are taken from *[1]*, *[11]*, *[69]*, *[81]*, and other sources.

Sources of information that are used as input for generating the ACP climatological likelihood parameters are summarized in Table 6. Coverage in all cases is global, with the exception of the total column optical depth, derived from the AVHRR Ocean Aerosol Product, which ranges between +70° and -70° latitude.

Table 6: Global-scale input data for the ACP

Aerosol	Source	Spatial resolution	Temporal resolution	Parameter	Units
Total (assumes sulfate)	*[30]*, *[62]*, *[71]*	1° x 1°	Weekly/monthly (07/89 to 12/93)	Total column optical depth (at 0.55 μm)	none
Sulfates	*[8]*, *[35]*	2.8° x 2.8°	Monthly	Column mass loading	g m^{-2}
				Column optical depth (0.5 to 0.7 μm)	none
Sulfates, carbonaceous smoke, black carbon	*[56]*	4.5° x 7.5°	Monthly	Column mass loading	g m^{-2}
Mineral dust	*[75]*, *[76]*	7.5° x 10.0°	Seasonally	Column mass loading	kg dust/ kg air

In addition, in situ observations of particle properties and surface measurements of column optical depth are used where available. Among these are relatively large efforts associated with the Laramie balloon program *[12]*, *[27]*, the Mauna Loa station *[9]*, a network of global sun-photometer observations *[28]*, and several multi-instrument comparative studies *[66]*, *[67]*, *[68]*, *[79]*. Other published sources include air mass aerosol composition mixing analyses (e.g., *[54]*), the conjoint statistical analysis of air mass trajectories and aerosol samples *[43]*, *[74]*, and many local measurement efforts.

A geographic information system (ERDAS Imagine) is used to facilitate comparison, reprojection, and storage of the data. Initially we will work with data that are not affected by the Pinatubo eruption.

3.5   THEORETICAL BASIS

Figure 3 shows those processes which occur at the MISR SCF prior to launch with respect to generation of the ACP. In the following sections, the physical basis and a mathematical description of the algorithm which is used to implement each process is presented.

3.5.1   Establish sizes and refractive indices for pure aerosol models

Establishment of the size distributions and optical constants for the pure aerosols involves two steps. First, the scientific literature is examined to establish a set of particles, and their associated properties, which form the basis of the MISR retrievals. In the second step, we verify that these particles are distinguishable from one another by the MISR observations, using sensitivity studies. Adjustments to the size distributions or particle list are made as result of this activity. For example, sensitivity studies have shown that the component commonly denoted "water soluble" *[11]* is not distinguishable by MISR from the sulfate accumulation mode 1 in Table 3. We accordingly use the sulfate particles in their place.

3.5.2   Calculate size distributions and refractive indices as function of RH

3.5.2.1   Physics of the problem

The relative humidity (RH) is known to have an important influence on aerosol properties, affecting both the particle size distribution and the indices of refraction. The magnitude of the hydration varies greatly with particle composition *[24]*, *[69]*. For common hygroscopic aerosol types, most of the increase in particle radius takes place as RH increases above 70%, and can increase the particle radius by factors of 5 as RH approaches 99% (particularly for typical sulfate and sea-salt particle types).

Particle growth due to changes in RH is often reported using a ratio of the radii at relative humidities of 85% and 35%. Popular values of this ratio for "global average" conditions are 1.7 ± 0.3, which are characteristic for maritime aerosols *[24]*. Tropospheric continental aerosols apparently are less hygroscopic, with the ratio typically ~ 1.55 *[24]*, and tend to be multi-modal, with some components more hygroscopic than others *[72]*. The most common conditions assumed when little else is known about ambient conditions is an ammonium sulfate composition, with accumulation mode size distribution, in 80 or 85% RH.

The net effect of RH on optical properties depends on the initial particle size distribution as well as on the magnitude of hydration: if the size distribution shifts from small sizes, where the particle scattering cross-section is small, into a region where the particle scattering efficiency at the wavelengths of interest is much greater, hydration will make a large difference, whereas if the particles are already in a regime where scattering is efficient, hydration will have a much smaller effect *[26]*. The difference amounts to factors of two to three in scattering efficiency for some common aerosol models.

3.5.2.2   Mathematical description of the algorithm

The relative humidity dependence of sizes and refractive indices for the MISR aerosol re-

trieval sensitivity studies uses the method now standard in most models, which was first developed by Hanel [24] and refined by Shettle and Fenn [69]. The approach includes both the surface tension and solute effects on particle vapor pressure in a semi-empirical way. The basic equations are:

$$r(hydrated) = r(dry)\left[1 + \frac{\xi(dry)}{\xi(water)} \cdot M(a_w)\right]^{\frac{1}{3}}$$

(1)

which can be derived from simple geometric considerations. In Eq. (1), $r(dry)$ and $\xi(dry)$ are the dry particle radius and density, M is the ratio $m(water)/m(dry)$, where $m(water)$ is the mass of condensed water and $m(dry)$ is the dry particle mass, $\xi(water)$ is the density of water, and r is the net particle radius. The ratio M is obtained from experimental data as a function of the water activity a_w. The largest uncertainty in this model is that $M(a_w)$ varies with particle properties. We are following current research in this area and will use the best available data. Water activity is related to the vapor pressure over the particle, and is given in terms of RH for typical atmospheric aerosols as:

$$a_w = RH \cdot \exp\left(-\frac{0.001056}{r}\right)$$

(2)

Because of the non-linear dependence of Eqs. (1) and (2) on r and a_w, they are solved iteratively, as per [69]. The final particle density and indices of refraction are obtained by volume weighting, according to:

$$\xi(hydrated) = \xi(water) + [\xi(dry) - \xi(water)] \cdot \left[\frac{r(dry)}{r(hydrated)}\right]^3$$

(3)

$$n_{r,i}(hydrated) = n_{r,i}(water) + [n_{r,i}(dry) - n_{r,i}(water)] \cdot \left[\frac{r(dry)}{r(hydrated)}\right]^3$$

(4)

where the subscript r, i on the refractive index indicates real or imaginary.

These equations describe the changes in particle properties for a given particle size. In actuality, the dry particles will have a variety of sizes represented by a distribution. A commonly used distribution, and the one adopted by MISR, is the log-normal distribution. Letting $n(r)\,dr$ be the number of particles per unit volume in the size range r to $r + dr$, the log-normal distribution states:

$$n(r) = \frac{N}{(2\pi)^{1/2} r \cdot \ln\sigma} \cdot \exp\left(\frac{-(\ln r - \ln r_c)^2}{2(\ln\sigma)^2}\right)$$

(5)

where

$$ln\,r_c = \frac{1}{N}\int_{r_1}^{r_2} ln\,r \cdot n(r)\,dr \tag{6}$$

$$(ln\,\sigma)^2 = \frac{1}{N}\int_{r_1}^{r_2} (ln\,r - ln\,r_c)^2 \cdot n(r)\,dr \tag{7}$$

where N is the total number of particles per unit volume, given by

$$N = \int_{r_1}^{r_2} n(r)\,dr \tag{8}$$

For each particle type in the climatology which is modeled as hydrating with increasing RH, the dry size distribution parameters r_c and σ are first specified. The size distribution to which the particles evolve under hydration is then fitted to a new log-normal distribution, which serves as input for the Mie calculations (the appropriate theory because hydrated particles are taken as spherical) of their single-scattering properties. This approach retains the full effect of hydration on the particle optical properties.

The surface fog and mineral dust models in the ACP use a power-law size distribution, as discussed in §3.5.1. In this case,

$$n(r) = C \cdot r^{-\alpha} \tag{9}$$

where the normalization constant C is determined by integrating Eq. (9) between limits r_1 and r_2 (see Table 5) and applying Eq. (8).

3.5.3   Calculate effective aerosol geometric parameters

3.5.3.1   Physics of the problem

As described above, the size distribution of the particles which hydrate with increasing relative humidity is assumed to follow a log-normal distribution for each aerosol component. It is assumed that humidity will change the size distribution according to the above theory. The hydrated size distribution will then be parameterized by a new log-normal distribution with a modified mean and standard deviation.

3.5.3.2 Mathematical description of the algorithm

The moments of the size distribution of the aerosol mixture can be determined:

$$\text{mean radius } \langle r \rangle = \frac{\int_{r_1}^{r_2} r \cdot n(r)dr}{\int_{r_1}^{r_2} n(r)dr} \tag{10}$$

$$\text{effective radius } r_{eff} = \frac{\int_{r_1}^{r_2} \pi r^2 \cdot r \cdot n(r)dr}{\int_{r_1}^{r_2} \pi r^2 \cdot n(r)dr} \tag{11}$$

$$\text{effective variance } v_{eff} = \frac{\int_{r_1}^{r_2} \pi r^2 \cdot (r - r_{eff})^2 \cdot n(r)dr}{r_{eff}^2 \int_{r_1}^{r_2} \pi r^2 \cdot n(r)dr} \tag{12}$$

$$\text{volume-weighted radius } r_{vw} = \frac{\int_{r_1}^{r_2} \frac{4}{3}\pi r^3 \cdot r \cdot n(r)dr}{\int_{r_1}^{r_2} \frac{4}{3}\pi r^3 \cdot n(r)dr} \tag{13}$$

In addition, we define the parameters G and V as follows:

$$G = \frac{\int_{r_1}^{r_2} \pi r^2 \cdot n(r)dr}{\int_{r_1}^{r_2} n(r)dr} \tag{14}$$

19

$$V = \frac{\int_{r_1}^{r_2} \frac{4}{3}\pi r^3 \cdot n(r)dr}{\int_{r_1}^{r_2} n(r)dr} \tag{15}$$

from which we can see that an alternate expression for Eq. (11) is

$$r_{eff} = \frac{3V}{4G} \tag{16}$$

3.5.4 Calculate effective aerosol optical parameters

3.5.4.1 Physics of the problem

The theory to be used for calculation of the single scattering properties of the aerosols depends on whether the particles are spherical or nonspherical. Mie theory describes the scattering from homogeneous spheres. The theory for nonspherical particles is more complex, not only from a computational standpoint but because of the wide variety of shapes that particles can take. For MISR, it is assumed that dust particles are a mixture of randomly oriented prolate and oblate spheroids. Scattering properties of such particles are obtained by the T-matrix method *[45]*, *[47]*. Ice particle scattering is calculated using ray tracing *[73]*.

3.5.4.2 Mathematical description of the algorithm

Using a polydisperse distribution of particle sizes, the single-particle theories provide effective single-scattering albedo, ϖ_{eff}, the effective single scattering phase function, p_{eff}, effective phase function asymmetry parameter, g_{eff}, and effective scattering and extinction cross sections k_{sca} and k_{ext}. Each of these is calculated as an average over the particle size distribution, weighted by the geometric cross sectional area of each particle, i.e.:

$$X_{eff} = \frac{\int_{r_1}^{r_2} \pi r^2 \cdot n(r) \cdot X(r)dr}{\int_{r_1}^{r_2} \pi r^2 \cdot n(r)dr} \tag{17}$$

where *X* represents one of the variables described above.

3.5.5 Identify likely aerosol mixtures

Aerosol retrievals will use as candidate models mixtures of the basic components shown in Table 3, with mixing ratios specified on a quantized grid as determined from sensitivity studies currently in progress. Certain filters will be used on the climatology to eliminate unreasonable cases (e.g., elimination of sea salt over mid-continents; upper bounds to the possible mixing ratio of black carbon, etc.). Sensitivity studies are being performed to determine which mixtures are distinguishable by the MISR instrument under the illumination and viewing conditions of the EOS orbit. Models which are observationally indistinguishable to within the measurement uncertainties of MISR will be binned together, thus limiting the number of distinct combinations. When complete, the climatology will provide various mixtures to be used in the retrieval process, yielding a substantial improvement over previous satellite-based retrievals of tropospheric aerosols, which have assumed a fixed, single aerosol type for all situations *[62]*.

The aerosol models to be compared with MISR observations during the retrievals consist of tropospheric models generated from mixtures of the pure particles contained in the ACP, plus fog, cirrus, and a stratospheric aerosol. Each tropospheric mixture contains up to three pure particles, and the relative abundances are specified in the mixture file of the ACP. Tropospheric aerosols are divided into marine and continental, and each of these two groupings is subdivided into four categories: clean, industrial, carbonaceous, and dusty. All maritime mixtures contain accumulation mode 1 sulfate and accumulation mode sea salt plus a third component which is either coarse mode sea salt, black carbon, carbonaceous aerosol, or accumulation mode mineral dust. All continental mixtures contain accumulation mode 1 sulfate and accumulation mode mineral dust plus a third component which is either black carbon, carbonaceous aerosol, or coarse mode mineral dust.

The starting points for generation of the "clim-likely" part the ACP are spatial and temporal patterns in the column optical depths reported in the AVHRR Ocean Aerosol Product to infer particle composition and source region in some instances. For example, the northern tropical maximum in optical depth has been attributed to Sahara dust over the Atlantic, whereas a smaller, late-summer increase in northern mid-latitudes is attributed to dust from the Gobi desert blown eastward over the Pacific *[41]*, *[71]*. A number of other seasonal patterns in aerosols have been interpreted in terms of whether the aerosols originate from land or from ocean sources, based on prevailing wind patterns, and whether the plumes appear to be attached to land regions or not *[30]*.

3.5.6 Compare distribution models to satellite data

To determine climatological likelihoods of the various aerosol mixtures, the sulfate, carbonaceous particles and black carbon, and mineral dust global distribution models are compared on a region-by-region basis with the AVHRR results over oceans, identifying locations where the particle composition is likely to be different from that assumed in the AVHRR analysis, and noting the respective values of optical depth. Over land, we will rely on a comparison among model re-

sults alone, plus assumptions about the continuity of results across coastal regions. From these comparisons, we will produce separate data layers for aerosol optical depth and aerosol type, and a third data layer indicating the constraint used at each grid point.

3.5.7   Apply regional in situ constraints

Contingent upon available time and resources, we will then apply the constraints of the in situ data, placing emphasis on those studies that provide (1) simultaneous measurements of multiple parameters, such as aerosol composition, column optical depth, and size distribution, (2) long time series of consistent measurements, and (3) measurements at locations where surface properties are relatively well-characterized, since they can serve as validation sites for the solar radiation flux budget. If there are suitable sunphotometer observations in ocean regions sampled by the AVHRR product, we will perform a statistical comparison using either an optimal sub-sampling technique (e.g., *[31]*), or if the in situ observations are dense enough in space and time, an analysis based on spatial coherence. The in situ data are used to fill in gaps and resolve discrepancies where possible. In particular, these observations are used to test the assumptions of about particle composition, modality, and width of size distribution made to varying degrees by each of the global-scale studies.

3.5.8   Scale aerosol mixing ratios

Relative abundances of the components are defined in the ACP in terms of fraction of total optical depth (*not* by numbers of particles). Since these relative abundances are wavelength and relative humidity dependent, due to the dependence of extinction cross section on wavelength and RH, we first specify a reference wavelength and relative humidity in establishing mixing ratios. The reference conditions used are band 2 (555 nm) and RH = 70%. The tabulated extinction cross sections as a function of wavelength and RH, contained in the aerosol physical and optical properties file of the ACP, are then used to calculate optical depth fractions for any other wavelength or relative humidity.

Starting with the relative contributions to the total extinction optical depth of the three components in each tropospheric aerosol mixture in band 2 and the reference relative humidity, we denote these reference relative amounts as f_{1r}, f_{2r}, and f_{3r}. Let k_{1r}, k_{2r}, and k_{3r} be the extinction cross sections of the three components at the reference wavelength and RH. The relative abundances at a different wavelength and RH, denoted f_1, f_2, and f_3, are then calculated from the extinction cross sections at that wavelength and RH, k_1, k_2, and k_3 and the above quantities by:

$$f_n = \frac{(k_n/k_{nr})f_{nr}}{\sum\limits_{n=1}^{3} (k_n/k_{nr})f_{nr}} \tag{18}$$

where the summation over n is for each of the three components in the aerosol mixture.

3.5.9 Determine optical depth spectral scale factors

For a given optical depth in band 2, which is used as the reference band during aerosol retrievals, it is necessary to determine the optical depth at the other MISR wavelengths and RH for a given aerosol mixture. Denoting the optical depth in the reference band and RH as τ_r, the optical depth in a different band and RH, τ, is given by

$$\tau = \tau_r \sum_{n=1}^{3} (k_n / k_{nr}) f_{nr} \qquad (19)$$

where the summation is over the (up to) three aerosol components in the mixture. If there is just a single aerosol component, as in the case of fog, cirrus, and stratospheric aerosol, Eq. (19) reduces to a simple scaling by the spectral extinction cross section.

3.5.10 Determine aerosol mixture single-scattering albedos

Calculation of the radiative properties of mixtures of aerosols requires knowledge of the single-scattering albedo of the mixture. For a mixture of n particle types, with ϖ_n defined to be the single-scattering albedo of the nth particle, the single-scattering albedo of the mixture is given by

$$\varpi_{mix} = \sum_{n} f_n \varpi_n \qquad (20)$$

4. SIMULATED MISR ANCILLARY RADIATIVE TRANSFER DATASET

4.1 PURPOSE

The Simulated MISR Ancillary Radiative Transfer (SMART) Dataset contains radiation fields to which the MISR observations are compared during the retrievals and is generated by performing radiative transfer calculations on stratified atmospheric models containing the pure aerosols found in the ACP. The calculations contained in the SMART Dataset include two surface boundary condition cases: (1) spectrally black surface, providing the path radiance field for all retrieval situations, and (2) the surface-leaving field for oceans or large dark water bodies.

We assume a stratified atmosphere with three distinct strata plus a surface model as shown in Figure 4. The top stratum is a single, homogeneous layer composed solely of Rayleigh scatterers. The middle stratum is a combination of tropospheric aerosol, stratospheric aerosol, or cirrus cloud plus Rayleigh scatterers. This stratum can be broken up into a number of homogeneous layers to simulate the density variation of its components with altitude. The aerosol or cirrus component is characterized by the altitudes of the base and top of the stratum (stratospheric aerosol base and top altitudes are above the tropopause, tropospheric aerosol or cirrus cloud base and top altitudes are below the tropopause). For the aerosol or cirrus the vertical variation of particle density within the stratum is described by a scale height. The bottom atmospheric stratum extends from the surface to the base of the middle stratum and can also be broken up into a number of homogeneous layers containing both Rayleigh scatterers and absorbing water vapor, each with a vertical variation of density described by its own scale height. Note that for those tropospheric aerosol models with a layer base at the surface, the bottom and middle strata are combined into one stratum which contains aerosols, Rayleigh scatterers, and water vapor. It is assumed that this stacking of strata as shown in Figure 4 is adequate to represent the real atmosphere for the purposes of MISR aerosol retrievals.

Rayleigh	Top atmospheric stratum
Tropospheric Aerosol, Stratospheric Aerosol, or Cirrus Cloud + Rayleigh	Middle atmospheric stratum
Rayleigh + Water Vapor	Bottom atmospheric stratum
///////////////////////////////////////	Surface Model (Black or Dark water)
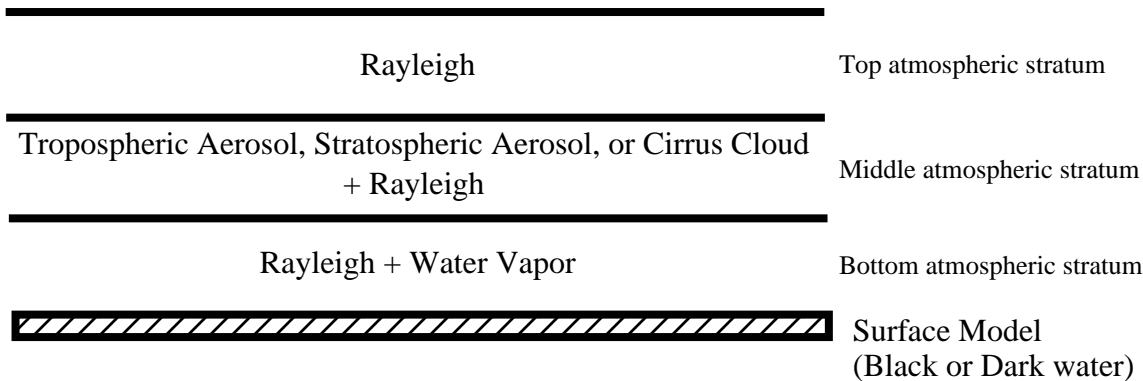
Figure 4. Stratified models assumed in the SMART Dataset

All of the strata depicted in Figure 4 are not populated simultaneously with the various types of atmospheric scatterers. That is, the tropospheric aerosol models do not contain any cirrus or stratospheric aerosol, the cirrus model has no tropospheric or stratospheric aerosol, and the stratospheric aerosol model does not contain any tropospheric aerosol or cirrus. At-launch retrievals will consider mixtures of tropospheric aerosol models, but mixtures of tropospheric aerosols, cirrus, and stratospheric aerosols will not be considered until the post-launch era, when we have had the opportunity to examine the results of retrievals on actual MISR data. The optical depth of the water vapor contained in the bottom stratum is established using a standard atmosphere.

4.2 CONTENTS

Each entry in the SMART dataset is specified by the parameters listed in Table 7. The last five parameters in the table are not used for aerosol retrievals but they are used for surface reflectance retrievals. All parameters with angular dependence use a common set of angle grids. For cosine of solar zenith angle μ_0 the grid point number is 81 with values ranging from 0.2 -1.0 (0.01), where the number in parenthesis indicates the grid point separation. The grid of cosine of view zenith angle μ is partitioned into five segments, each corresponding to a symmetric pair of MISR cameras (Df and Da, Cf and Ca, etc.). The D, C, B, and off nadir A camera segments cover the ranges 0.31-0.35 (0.01), 0.47-0.51 (0.01), 0.66-0.71 (0.01), and 0.85-0.90 (0.01), respectively, and the fifth segment, corresponding to the nadir A camera, covers the range 0.95-1.0 (0.01). Thus, there are 5 grid points in each of the first two segments and 6 grid points in each of the last three segments, resulting in a total of 28 view zenith angle grid points. Instead of relative azimuth angle $\phi-\phi_0$, an equivalent representation in terms of scattering angle Ω is used in the SMART dataset. The scattering angle range is partitioned into 4 contiguous segments, 0°-120° (2.5°), 120°-150°(1°), 150°-175° (2.5°), and 175°-180°(1°), totaling 94 grid points. In general, a selection of any particular (μ, μ_0) combination will not allow the complete range of scattering angles to exist. Thus, the 94 scattering angle grid is supplemented by two additional points, representing the minimum and maximum allowable scattering angles for a particular (μ, μ_0) pair, bringing the total number of scattering angle grid points to 96.

Following launch, it will probably be necessary to update the ACP and the SMART Dataset, to adjust for systematic behavior noted in the early retrieval results, to account for new types of aerosols. However, changes to the SMART Dataset may result in systematic changes to the retrieved aerosol models, and possibly to the retrieved optical depths. Thus, any changes being considered to the ACP or SMART Dataset after routine production of the MISR Aerosol/Surface Product begins will first be studied at the MISR SCF. Any resulting changes to the baseline will be documented, and a decision will be made whether to implement the change, and whether it is necessary

to reprocess part or all of the prior MISR Aerosol/Surface Product.

Table 7: Contents of the SMART Dataset

Parameter	Description	Units
m	Aerosol model number, including composition/size type identifier, relative humidity (%), and atmospheric layer identifier	none
τ	Aerosol optical depth in the four MISR bands	none
P	Ambient pressure	hPa
μ, μ_0	Cosines of view and solar angles	none
Ω	Scattering angle	deg
Radiation parameters for black surface		
ρ_{ss}	Single-scattered top-of-atmosphere equivalent reflectance in each MISR spectral band for the model conditions and geometries specified above	none
ρ_{ms}	Multiple-scattered top-of-atmosphere equivalent reflectance in each MISR spectral band for the model conditions and geometries specified above	none
$e_{b,ss}^{diff}$	Single-scattered diffuse irradiance at the bottom of the atmosphere in each MISR spectral band for the model conditions specified above, normalized to the exo-atmospheric solar irradiance	none
$e_{b,ms}^{diff}$	Multiple-scattered diffuse irradiance at the bottom of the atmosphere in each MISR spectral band for the model conditions specified above, normalized to the exo-atmospheric solar irradiance	none
$T_{0,ss}$	Single-scattered upward-directed diffuse atmospheric transmittance, integrated over azimuth angle, in each MISR spectral band for the model conditions and geometries specified above	none
$T_{0,ms}$	Multiple-scattered upward-directed diffuse atmospheric transmittance, integrated over azimuth angle, in each MISR spectral band for the model conditions and geometries specified above	none

Table 7: Contents of the SMART Dataset (continued)

Parameter	Description	Units
$T_{1,ss}$	Single-scattered upward-directed diffuse atmospheric transmittance, weighted by the cosine of the azimuth angle and integrated over azimuth angle, in each MISR spectral band for the model conditions specified above	none
$T_{1,ms}$	Multiple-scattered upward-directed diffuse atmospheric transmittance, weighted by the cosine of the azimuth angle and integrated over azimuth angle, in each MISR spectral band for the model conditions specified above	none
t_{ss}	Single-scattered upward-directed diffuse atmospheric transmittance, integrated over azimuth and illumination zenith angle, in each MISR spectral band for the model conditions specified above	none
t_{ms}	Multiple-scattered upward-directed diffuse atmospheric transmittance, integrated over azimuth and illumination zenith angle, in each MISR spectral band for the model conditions specified above	none
s_{ss}	Single-scattered bottom-of-atmosphere bihemispherical albedo in each MISR spectral band for the model conditions specified above	none
s_{ms}	Multiple-scattered bottom-of-atmosphere bihemispherical albedo in each MISR spectral band for the model conditions specified above	none
Additional parameters for dark water surfaces		
W	Surface wind speed	m sec^{-1}
ρ_{surf}	Component of top-of-atmosphere equivalent reflectance corresponding to radiation that has interacted with the surface in each MISR spectral band for the model conditions and geometries specified above	none

4.3 PROCESSING OUTLINE

Figure 5 shows conceptually the processes involved in generation of the SMART Dataset.

Numbers next to process boxes refer to sections in the text describing the algorithm
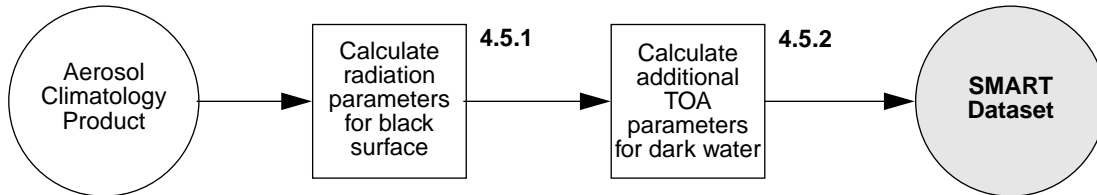
Figure 5. Conceptual processing flow for generation of the SMART Dataset

4.4 INPUT DATA

The primary source of input data for generation of the SMART Dataset is the ACP. Using the optical properties of the aerosols contained in the ACP, forward radiative transfer calculations are performed at the MISR SCF, as outlined in Figure 5, to calculate the parameters in Table 7. These are calculated for a variety of view and illumination geometries, corresponding to the range of values relevant to the MISR experiment. The results are provided over ranges of total aerosol optical depth, aerosol type, and relative humidity.

4.5 THEORETICAL BASIS

For the aerosol retrievals over dark water, the pre-calculated radiation fields in the SMART Dataset are provided assuming a surface model that accounts for the effects of wind speed on sun glint and whitecaps. In the case of homogenous land regions identified as being covered by Dense Dark Vegetation (DDV), the portion of the SMART Dataset containing the black surface top-of-atmosphere radiation fields, as well as the atmospheric transmittance and bottom-of-atmosphere irradiance data are used, and the TOA equivalent reflectances assuming a prescribed surface bidirectional reflectance model are calculated during the retrieval processing at the DAAC. Finally, for the retrievals over heterogeneous land surfaces the radiation fields also use the black surface field, and the effects of surface reflectance are accounted for during the actual retrievals.

4.5.1 Calculate radiation parameters for black surface

4.5.1.1 Physics of the problem

The physical basis for describing the transport of radiation in the atmosphere, its interaction with aerosols, and its interaction between the atmosphere and the surface is radiative transfer (RT) theory (e.g., *[7]*). The radiative transfer equation can be solved for a variety of surface boundary

conditions, including non-lambertian and heterogeneous (in reflectance) terrain. Retrievals over regions of complex topography are not envisioned at launch, so the underlying theory behind the aerosol retrievals assumes a flat lower boundary. Extinction of radiation occurs via two processes: absorption and scattering. Attenuation of the incident and reflected beams is offset by diffuse radiation that has been (1) reflected by the atmosphere without reaching the surface, (2) subjected to multiple reflections between the atmosphere and surface, and (3) scattered into the line-of-sight from neighboring terrain. With regard to the latter process, often referred to as the "adjacency effect", the horizontal photon diffusion (or "blurring") scale length is of the order of the effective scale height of the atmospheric scatterers. Thus, images of a surface overlain by an atmosphere with an optical depth dominated by tropospheric aerosols in the lower few kilometers will have a non-negligible blurred component if the image spatial resolution is coarser than ~ 1 km. This is the 3-D radiative transfer regime *[13]*, *[14]*, *[34]*. On the other hand, when the image spatial resolution is greater than ~ 1 km no significant blurring is expected. This is the standard 1-D radiative transfer regime.

Forward radiative transfer calculations, which will form the basis for the MISR aerosol retrieval, are based on the doubling/adding method of solving the RT equation for plane-parallel geometry. The principle behind doubling/adding is to calculate an exact solution for horizontally homogeneous layers of extremely small optical thickness, and then to use a recipe to describe the combined effect of pairs of layers. This process is repeated to build up layers of arbitrary optical thickness. When the subsequent layers have the same optical properties as the initial layers, a geometric doubling process builds up the atmospheric model. For vertically inhomogeneous atmospheres, subsequent layers are added. Further description of this method is found in Hansen and Travis *[25]*.

The MISR approach is to consider the atmosphere to be vertically stratified into three strata (see Figure 4). A high altitude, purely absorbing layer consisting of ozone, is not included in the forward calculations; rather, a correction is made during the retrieval process. Forward radiative transfer calculations are performed using the matrix operator technique of Grant and Hunt *[22]* for a number of different tropospheric aerosol types, and for a range of optical depths of tropospheric aerosol, cirrus cloud, and stratospheric aerosol. The minor water vapor absorption affecting the MISR band 4 radiances is included in the forward calculations. We use standard atmospheric temperature and water vapor profiles to establish the water vapor optical depth. Although this procedure is not strictly accurate, the water vapor optical depth in band 4 is only on the order of a few thousandths, as determined from convolution of MODTRAN spectra with the predicted MISR spectral response. The Rayleigh scattering will be described by a single value for the optical depth, specified for a reference surface pressure. Since Rayleigh optical depth is proportional to the surface pressure, the computed TOA equivalent reflectances in all four bands will need to allow for any variations in surface pressure. Over land the pressure variations can be significant due to changes in terrain elevation. This is handled by performing the calculations in the SMART Dataset

for several pressure values, and interpolating to the appropriate value during the retrievals.

The parameters in the SMART Dataset corresponding to the black surface case are split into their contributions due to single scattering and multiple scattering. The reason for this is that during aerosol and surface retrievals, mixtures of the pure aerosols contained in the ACP will be employed, and the radiation parameters for the mixtures are calculated from the fields for the pure particles, and combined according to a newly developed linear mixing approach (see *[M-11]* and *[M-12]*). This modified linear mixing approach is more accurate than standard linear mixing when there is a large variation in the single scattering albedos of the component aerosols. However, this improved accuracy is achieved at the expense of requiring the single and multiple-scattered fields to be considered separately.

Polarization of scattered light can affect the radiances measured by MISR. The difference in the radiance field as computed by a vector code from that computed by a scalar code is dominated by the highly polarized Rayleigh-scattered light from gas molecules. Aerosols have smaller polarization over most angles and the radiance field can be calculated adequately for the purpose of interpreting MISR observations with a scalar code. To include the effects of polarization we correct radiances in our scalar calculations by subtracting the contribution due to the Rayleigh scattering, including its interaction with the surface. We then add back this contribution as calculated with a vector code. The interaction of the polarized Rayleigh scattering from the atmosphere and the polarizing Fresnel reflection from the water surface is important. Initially, we implement a correction only to the atmospheric path radiance. A correction to the surface term corresponding to water-leaving radiances is deferred to a later time.

A wide variety of surface reflectance properties can be handled by the adding method; however, our retrieval approach requires storing in the SMART Dataset only the radiation fields for a black surface and a surface glitter/whitecap model. In the case of calm ocean (no wind), the reflection function for specular reflection is Fourier decomposed in azimuth. Instead of integrating over zenith angle as is done for diffuse radiation, atmosphere-surface interactions are formed by multiplying the surface reflection matrix by the reflection matrix for the atmosphere. For a smooth surface the reflection matrix is a diagonal one with the magnitude of each element given by the Fresnel reflection law. For a rough surface (e.g., when wind is present) off-diagonal terms become important. The magnitude of the off-diagonal terms can be estimated from Cox-Munk theory *[10]*, *[80]* (see §4.5.2). Complex surfaces consisting of Fresnel and diffuse reflection can be added as well, weighted by their fractional areas.

4.5.1.2 Mathematical description of the algorithm

4.5.1.2.1 *General background*

The dependence of Rayleigh optical depth on surface pressure and wavelength is given as

follows [68]:

$$\tau_{Rayleigh} = \frac{P}{P_0} \cdot (0.00864 + 6.5x10^{-6} \cdot z) \cdot \lambda^{-\left(3.916 + 0.074 \cdot \lambda + \frac{0.050}{\lambda}\right)} \qquad (21)$$

where P is the ambient pressure in millibars, P_0 is the standard surface pressure of 1013.25 mbar, z is the height above sea level in km, and λ is the wavelength expressed in μm. We plan to ignore the z dependence in Eq. (21), as it results in an increase in Rayleigh optical depth at the shortest MISR wavelength of only 0.0016 at 9 km altitude (the height of Mt. Everest), and this is an extreme case. The equation differs slightly from an inverse fourth power law due to the wavelength dependence of the index of refraction of air. This formulation will be used to produce data in the SMART Dataset corresponding to two values of pressure. The pressure values chosen span the range that will be encountered during aerosol retrievals at any altitude above the surface.

The 865 nm MISR channel is nearly centered on a window region where there is little absorption by water vapor. Nevertheless, some water lines do overlap the passband. We estimate that the absorption optical depth for water vapor varies from 0.002 for a standard atmosphere model to 0.005 for a saturated tropical atmosphere model. The standard atmosphere Rayleigh scattering optical depth at 865 nm is 0.016, and MISR expects to retrieve aerosol optical depths of a few hundredths, so water vapor absorption is considered important enough to warrant inclusion in the radiative transfer calculations.

As described above, water vapor is modeled as being confined to the lowest layer of the atmosphere. The simplest way to incorporate it into the forward radiative transfer calculation is to add its absorption optical depth to that of the Rayleigh atmosphere and any aerosol considered to be concentrated in the lowest stratum. Then, the combined optical depth for aerosol, Rayleigh, and water vapor would be

$$\tau_t = \tau_a + \tau_R + \tau_w \qquad (22)$$

and the effective single scattering albedo of any layer in the bottom atmospheric stratum would be

$$\omega = \frac{\tau_{as} + \tau_R}{\tau_t} = \frac{\omega_{eff}\tau_a + \tau_R}{\tau_a + \tau_R + \tau_w} \qquad (23)$$

where ω_{eff} is defined by Eq. (17), τ_a is the aerosol extinction optical depth, τ_{as} is the aerosol scattering optical depth, τ_R is the Rayleigh scattering optical depth, and τ_w and is the water vapor optical depth. The optical depth of water is an average over the MISR passband. It is computed by convolving the results of MODTRAN with the sensitivity function for the instrument. The water

vapor optical depth will be determined using a standard atmosphere temperature profile. Errors in the temperature profile produce errors in water vapor optical depth of approximately 0.001 or less, which is small compared to the effects of other uncertainties.

As discussed in §3.2, aerosol layers are characterized by three vertical distribution parameters: h_b, the base height of the aerosol layer; h_t, the top height of the aerosol layer; and h_s, the scale height of the layer. Using these parameters, aerosol extinction coefficient κ varies with altitude z as

$$\kappa(z) = 0, \ 0 \leq z < h_b$$

$$\kappa(z) = \kappa(h_b)\exp\left(-\frac{z}{h_s}\right), \ h_b \leq z \leq h_t$$

$$\kappa(z) = 0, z > h_t \tag{3a}$$

and

$$\tau_a = \int_0^\infty \kappa(z)dz = \kappa(h_b)\int_{h_b}^{h_t}\exp\left(-\frac{z}{h_s}\right)dz = \kappa(h_b)h_s \cdot \left[\exp\left(-\frac{h_b}{h_s}\right) - \exp\left(-\frac{h_t}{h_s}\right)\right] \tag{3b}$$

Note that when it is desired to make the aerosol layer vertically uniform, we choose h_s to be a large number (e.g., 1000 km), and Eq. (3b) reduces to

$$\tau_a = \kappa(h_b) \cdot [h_t - h_b] \tag{3c}$$

The radiance L leaving the top of the atmosphere can be written as

$$L_{x,y}(-\mu, \mu_0, \phi - \phi_0) = L^{atm}(-\mu, \mu_0, \phi - \phi_0) +$$

$$+ \exp(-\tau/\mu) \cdot \frac{1}{\pi}\int_0^1\int_0^{2\pi} R_{x,y}^{surf}(-\mu, \mu', \phi - \phi')L_{x,y}^{inc}(\mu', \mu_0, \phi' - \phi_0)\mu'd\mu'd\phi' +$$

$$+ \frac{1}{\pi}\int_0^1\int_0^{2\pi}\int_0^1\int_0^{2\pi} T_{x,y}(-\mu, -\mu'', \phi - \phi'') \otimes R_{x,y}^{surf}(-\mu'', \mu', \phi'' - \phi')L_{x,y}^{inc}(\mu', \mu_0, \phi' - \phi_0)\mu'd\mu''d\phi''d\mu'd\phi' \tag{24}$$

where x, y are the image spatial coordinates in a Cartesian coordinate system in which $+z$ points toward the center of the Earth and is normal to the surface ellipsoid (not the local topographically-defined surface orientation), $+x$ points toward the north pole, θ and θ_0 are the view and Sun angles with respect to the $+z$ axis, $\mu = |\cos\theta|$, $\mu_0 = |\cos\theta_0|$, ϕ_0 is the azimuthal angle of the solar illumination

32

vector, and ϕ is the azimuthal angle of a vector pointing toward the MISR instrument, also in the ellipsoid reference system. These definitions lead to the convention of using $-\mu$ and μ for upwelling and downwelling radiation respectively. The properties of the atmosphere are assumed to be horizontally homogeneous. On the right-hand-side of Eq. (24), L^{atm} is the radiance field scattered by the atmosphere to space without interacting with the surface (i.e., the path radiance), τ is the optical depth of the total atmosphere, $L^{inc}_{x,y}$ is the direct and diffuse downward radiance field incident on the surface, $T_{x,y}$ is the upward diffuse transmittance, and $R^{surf}_{x,y}$ is the spatially variable surface bidirectional reflectance factor (BRF). The BRF of a surface target is defined as the bidirectional reflectance distribution function of the target ratioed to the bidirectional reflectance distribution function from a non-absorbing lambertian surface with all measurements made under identical atmospheric conditions *[53]*.

In the general three-dimensional solution to the radiative transfer problem with a horizontally uniform atmosphere over a spatially varying and flat surface, the transmittance $T_{x,y}$ can be thought of as a point-spread function and with the convolution operation $\otimes$ describes the blurring effect of the atmosphere on the surface reflectance $R^{surf}_{x,y}$ *[15]*. When the image spatial resolution is comparable to the atmospheric scattering scale height (defined by the vertical distribution of the aerosols and/or Rayleigh scattering molecules), Eq. (24) reduces to the standard one-dimensional radiative transfer regime, and $T_{x,y}$ is effectively a delta function in the spatial coordinates. In this case, Eq. (24) simplifies to:

$$L_{x,y}(-\mu, \mu_0, \phi - \phi_0) = L^{atm}(-\mu, \mu_0, \phi - \phi_0) +$$

$$+ \exp(-\tau/\mu) \cdot \frac{1}{\pi} \int_0^1 \int_0^{2\pi} R^{surf}_{x,y}(-\mu, \mu', \phi - \phi') L^{inc}_{x,y}(\mu', \mu_0, \phi' - \phi_0) \mu' d\mu' d\phi' +$$

$$+ \frac{1}{\pi} \int_0^1 \int_0^{2\pi} \int_0^1 \int_0^{2\pi} T(-\mu, -\mu'', \phi - \phi'') R^{surf}_{x,y}(-\mu'', \mu', \phi'' - \phi') L^{inc}_{x,y}(\mu', \mu_0, \phi' - \phi_0) \mu' d\mu'' d\phi'' d\mu' d\phi'$$

$$\tag{25}$$

MISR data will be acquired in various averaging modes. The 3-D radiative transfer regime is appropriate for the high-resolution channels (1 x 1 or 1 x 4) and the 1-D regime is appropriate for 4 x 4-averaged samples.

A further simplification of Eq. (25) occurs over surfaces which are uniform in reflectance. For such cases, Eq. (25) is simplified by eliminating the *x, y* subscripts from the equation. Finally, in the case where the surface is black, only the path radiance term survives.

The polarization correction is implemented according to the following equation:

$$\tilde{L} = L - L_{Rayleigh} + \tilde{L}_{Rayleigh} \qquad (26)$$

where $\tilde{L}$ is the radiance including the effects of polarization, L is the radiance computed by the scalar radiative transfer code, and the last two terms on the right-hand-side of Eq. (26) are the radiances for a model with clear atmosphere only and no aerosols, from scalar and polarization codes, respectively.

4.5.1.2.2 TOA equivalent reflectances

The general relationship between equivalent reflectance and radiance is:

$$\rho_{equiv} = \pi L_\lambda / E_{0\lambda} \qquad (27)$$

where L_λ is the spectral radiance incident at the sensor, and $E_{0\lambda}$ is the spectral exo-atmospheric solar irradiance at wavelength λ. The use of equivalent reflectance permits radiance levels to be expressed in terms of a single band-independent parameter. Equivalent reflectance conceptually represents an arbitrary radiance level in terms of the particular value of reflectance of an exo-atmospheric lambertian target, illuminated by the Sun at normal incidence, that would yield the same radiance at the sensor.

For a black surface, the TOA equivalent reflectances stored in the SMART Dataset are, for each spectral band,

$$\rho_{ss} = \pi L_{ss}^{atm} / E_0$$

$$\rho_{ms} = \pi L_{ms}^{atm} / E_0 \qquad (28)$$

where the subscripts indicate that the radiation field has been separated into its single- and multiple-scattered components. Equivalent reflectance calculations performed in generating the SMART Dataset are monochromatic, with the exception that the water vapor optical depth included in the band 4 calculations is an average for the MISR passband.

Equivalent reflectances are stored in the SMART Dataset as a function of the geometric variables μ, μ_0, and Ω, where Ω is the scattering angle, given by

$$\cos\Omega = -\mu\mu_0 + (1 - \mu^2)^{\frac{1}{2}}(1 - \mu_0^2)^{\frac{1}{2}}\cos(\phi - \phi_0) \qquad (29)$$

The storage in terms of μ, μ_0, and Ω, rather than the more conventional μ, μ_0, and ϕ - ϕ_0, is done so

that the grid in Ω can be tailored to enable finer coverage in angular regions where the aerosol single-scattering phase functions vary rapidly, e.g., in the presence of rainbows.

4.5.1.2.3 BOA diffuse irradiance

The radiance field incident upon the surface at the bottom of the atmosphere (BOA), denoted L^{inc} in Eq. (25), may be separated into direct and diffuse components, that is,

$$L^{inc}(\mu', \mu_0, \phi' - \phi_0) = L^{dir}(\mu', \mu_0, \phi' - \phi_0) + L^{diff}(\mu', \mu_0, \phi' - \phi_0)$$

$$= \frac{\mu_0}{\pi} E_0 \exp(-\tau / \mu_0) + L^{diff}(\mu', \mu_0, \phi' - \phi_0) \tag{30}$$

If we now integrate L^{diff} over solid angle to obtain an irradiance, and normalize to the exo-atmospheric solar irradiance E_0, and further separate the diffuse field into its single- and multiple-scattered components, we obtain:

$$e_{b, ss}^{diff} = \frac{1}{E_0} \int_0^1 \int_0^{2\pi} L_{ss}^{diff}(\mu', \mu_0, \phi' - \phi_0) \mu' d\mu' d\phi'$$

$$e_{b, ms}^{diff} = \frac{1}{E_0} \int_0^1 \int_0^{2\pi} L_{ms}^{diff}(\mu', \mu_0, \phi' - \phi_0) \mu' d\mu' d\phi' \tag{31}$$

4.5.1.2.4 Upward diffuse transmittance

The upward diffuse transmittance, T, may be expanded in a Fourier series in azimuth angle. If we retain only the first two terms of the expansion, the mathematical representation of this is

$$T(-\mu', -\mu, \phi' - \phi) \cong T_0(-\mu', -\mu) + T_1(-\mu', -\mu)\cos(\phi' - \phi) \tag{32}$$

with

$$T_0(-\mu', -\mu) = \frac{1}{2\pi} \int_0^{2\pi} T(-\mu', -\mu, \phi' - \phi) d\phi' \tag{33}$$

and

$$T_1(-\mu', -\mu) = \frac{1}{\pi} \int_0^{2\pi} T(-\mu', -\mu, \phi' - \phi) \cos(\phi' - \phi) d\phi' \qquad (34)$$

The integrated diffuse transmittance, t, is related to T_0 by the following equation:

$$t(-\mu) = 2\pi \int_0^1 T_0(-\mu', -\mu) d\mu' \qquad (35)$$

The terms defined by Eqs. (33) - (35) are then separated in to their single-scattered and multiple-scattered components.

4.5.1.2.5 BOA bihemispherical albedo

The bottom-of-atmosphere bihemispherical albedo for isotropic incident radiation, s, is defined according to the following equation:

$$s = \frac{1}{\pi^2} \int_0^1 \int_0^{2\pi} \int_0^1 \int_0^{2\pi} \rho^{atm}(\mu, -\mu', \phi - \phi') \mu \, d\mu \, d\phi \, d\mu' \, d\phi' \qquad (36)$$

where $\rho^{atm}(\mu, -\mu', \phi - \phi')$ is the underside atmospheric path radiance expressed as an equivalent reflectance. We also separate s into its single-scattered and multiple-scattered components.

4.5.2 Calculate additional TOA parameters for dark water

4.5.2.1 Physics of the problem

Referring to Eq. (25), this step involves calculating the sum of the second and third terms on the right-hand-side, that is, the radiation field corresponding to photons which have interacted with the surface. Unlike the parameters contained in the SMART Dataset for the black surface case, we do not require a separation into single- and multiple-scattered components, as standard linear mixing theory will be used for these terms during the retrieval process.

Under conditions when there is no surface wind, the water surface is flat and acts as a Fresnel reflector. Sunlight incident on the surface is reflected only in the specular direction. However, it is more common that there is some surface wind. The long-term annual mean wind speed over the oceans varies from about 5 - 9 m/sec *[29]*. The wind roughens the water surface, which can then

be modeled as an array of facets with a distribution of slopes. A basic theory was worked out by Cox and Munk *[10]*. As wind speed increases, the wave slopes increase and the glitter pattern increases in angular width. Over dark water, this model will be used to establish the lower boundary condition for the RT calculations. In addition, it will be used to determine which cameras cannot be used in the aerosol retrieval due to contamination by glitter.

At viewing geometries away from the sunglint pattern, the water surface is nearly black at 670 and 865 nm, though a small surface brightness resulting from the presence of whitecaps is assumed. The fraction of the sea surface that is covered by whitecaps is a function of wind speed *W*; however it is also related to the atmospheric stability, and possibly to the water temperature itself *[6]*, *[48]*. Gordon and Wang *[20]* have shown that for wind speeds less than 10 - 12 m/sec present models relating whitecap reflectance to wind speed are sufficient for SeaWiFS atmospheric corrections when the aerosol scattering is weakly dependent on wavelength. Since the equivalent reflectance of the sea surface due to whitecaps is small for these wind speeds (e.g., < 0.007 for $W <$ 14 m/sec), the model adopted for MISR uses only wind speed as an input parameter, and is based on Monahan and O'Muircheartaigh *[49]* and Koepke *[38]*. The dark water surface parameters are evaluated for three wind speeds, 2, 5, and 10 m/sec, in the SMART dataset.

4.5.2.2   Mathematical description of the algorithm

We begin by describing the mathematical form of the surface BRF, R^{surf}, for reflection from the ocean surface.

The contribution to the MISR-measured radiance from sun glitter (the specular reflection of sunlight from the sea surface) is modeled according to the formulation of Cox and Munk *[10]* and modified by Mishchenko and Travis *[46]*. In this development the sea surface is modeled as a collection of facets with individual slope components z_x and z_y. In a coordinate system with the $+y$ axis pointing toward the Sun (such that the projection of the Sun's rays on the sea surface is along the $-y$ axis), given the solar zenith angle and the angles θ and ϕ specifying the reflected ray, the orientation (β, α) of the facet normal n_f (see Figure 6) required for the facet to reflect sunlight in the direction of (θ, ϕ) is found from:

$$\cos(2\gamma) = \cos\theta\cos\theta_0 - \sin\theta\sin\theta_0\cos\phi$$

$$\cos\beta = (\cos\theta + \cos\theta_0)/2\cos\gamma$$

$$\cos\alpha = (\cos\phi\sin\theta - \sin\theta_0)/2\cos\gamma\sin\beta$$

$$\sin\alpha = (\sin\phi\sin\theta)/2\cos\gamma\sin\beta$$

$$z_x = \sin\alpha\tan\beta$$

$$z_y = \cos\alpha\tan\beta$$

$$(37)$$

Note that for a flat (smooth) surface, $\phi = 0$.
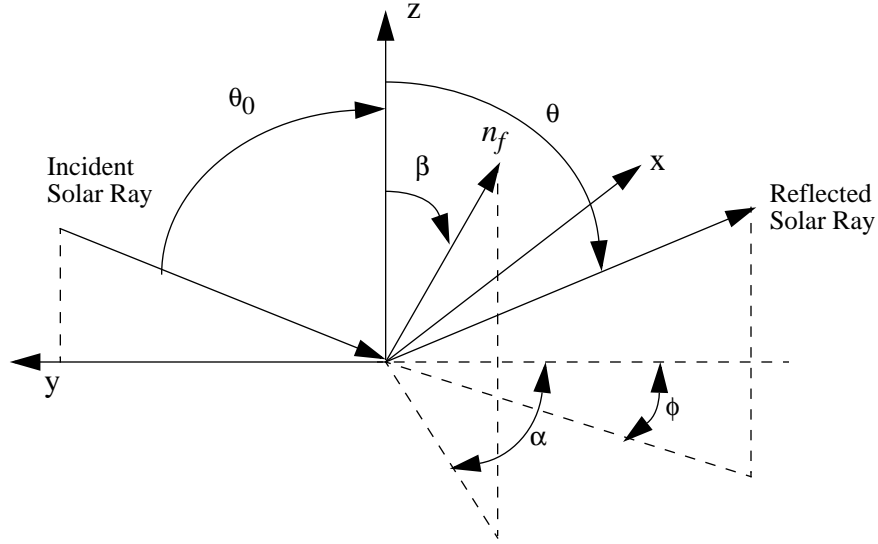
Figure 6. Geometry of reflection from a rough sea surface. n_f is the unit normal to the facet that is oriented properly to reflect the sunlight as shown

The BRF of the surface due to sun glitter, in the absence of an atmosphere, is

$$R^{glitter} = \frac{\pi r(\gamma)}{4\mu\mu_0(\cos\beta)^4} p(z'_x, z'_y) S(\mu, \mu_0) \tag{38}$$

where $r(\gamma)$ is the Fresnel reflectance for unpolarized light incident at an angle γ, and $p(z'_x, z'_y)$ is the probability density of surface slopes for isotropic wind given by *[46]*:

$$p(z'_x, z'_y) = (2\pi s^2)^{-1} \exp[-(\xi^2 + \eta^2)/2] \tag{39}$$

where

$$\xi = z'_x/s$$

$$\eta = z'_y/s \tag{40}$$

and the mean square surface slope s^2 is related to the near-surface scalar wind speed by

$$2s^2 = 0.003 + 0.00512 \cdot W \tag{41}$$

with W in m/sec. In Eq. (38), S is a shadowing function given by *[46]*:

38

$$S(\mu, \mu_0) \;=\; \frac{1}{1 + \Lambda(\mu) + \Lambda(\mu_0)} \tag{42}$$

where

$$\Lambda(\mu) \;=\; \frac{1}{2}\left(\left[\frac{2(1-\mu^2)}{\pi}\right]^{\frac{1}{2}} \cdot \frac{s}{\mu} \cdot \exp\left(-\frac{\mu^2}{2s^2(1-\mu^2)}\right) - \mathrm{erfc}\left(\frac{\mu}{s\sqrt{2(1-\mu^2)}}\right) \right) \tag{43}$$

and erfc is the complementary error function.

The BRF of the sea surface due to whitecaps, in the absence of an atmosphere, is

$$R^{whitecap} \;=\; (0.22) \cdot 2.95 \times 10^{-6} W^{3.52} \tag{44}$$

where the factor 0.22 is the effective reflectance of a whitecap, taken to be lambertian [38]. The fraction of the sea surface covered by whitecaps enters into this equation and is expressed as an empirical power law in the wind speed W.

A different algorithm to calculate whitecap reflectance is given by Gregg and Carder [23], and is a formulation based on wind stress. This algorithm includes the density of air, the drag coefficient as a function of wind speed, and a number of coefficients relating wind stress to foam reflectance. A comparison of Eq. (44) with Gregg and Carder's algorithm shows negligible differences for wind speeds up to 18 m/sec.

The BRF for the surface is then taken to be the sum of the glitter and whitecap contributions. Putting these expressions into the second and third terms on the right-hand-side of Eq. (25), then converting the resulting field to equivalent reflectance according to Eq. (27), provides the parameter to be incorporated into the SMART Dataset.

5. TROPICAL OCEAN ATMOSPHERIC CORRECTION DATASET

5.1 PURPOSE

The Tropical Ocean Atmospheric Correction (TOAC) Dataset contains components of the reflectance of the atmosphere-ocean surface combination relating to the aerosol and its interaction with molecular scattering. It is used in atmospheric correction of MISR imagery over the tropical oceans in a manner similar to that described in *[21]*. This use is also described in considerable detail in *[19]*. It is generated by radiative transfer (RT) calculations performed for a two-layer atmosphere with aerosol scattering in the lower layer and molecular scattering in the upper layer. The radiative properties of the aerosol are presently taken from the generic models of Shettle and Fenn *[69]*. In the computations, the sea surface is modeled as a flat Fresnel-reflecting surface that absorbs all of the radiance transmitted into the water. Thus, the vertical structure of the atmospheric model is similar to that in Figure 4 without the top two layers and without water vapor. Accounting for the effects of whitecaps and sun glitter on the radiation field is not required, as they are removed from the TOA reflectance before application of the TOAC Dataset.

5.2 CONTENTS

For a given aerosol model, the TOAC Dataset contains the coefficients $a^{(m)}(-\mu, \mu_0; \lambda)$, $b^{(m)}(-\mu, \mu_0; \lambda)$, and $c^{(m)}(-\mu, \mu_0; \lambda)$ defined by Eqs. (50) and (52) below, for $0 \leq m \leq 14$, 35 values of $-\mu$, 33 values of μ_0, and 4 MISR spectral bands. Presently the computations have been completed for 12 aerosol models of Shettle and Fenn *[69]*. During the ocean surface water-leaving equivalent reflectance retrievals to be performed during generation of the ocean surface parameters of the MISR Aerosol/Surface Product, these coefficients are used in conjunction with MISR-derived aerosol and Rayleigh-aerosol interaction components of the top-of-atmosphere radiation field to generate estimates of the aerosol single-scattering signature. This is then used in the atmospheric correction algorithm.

5.3 PROCESSING OUTLINE

Figure 7 shows conceptually the processes involved in the generation of the TOAC Dataset.
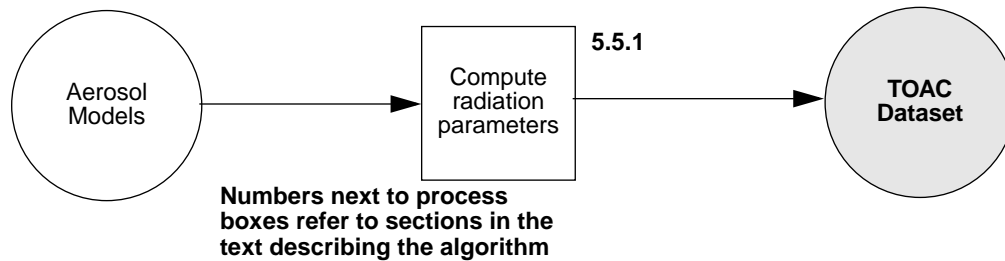
Figure 7. Conceptual processing flow for generation of the TOAC Dataset

5.4 INPUT DATA

The input data are the aerosol models. Basic generic models *[69]* have been used in generating the present TOAC Dataset; however, new models are expected to be available in the future.

5.5 THEORETICAL BASIS

5.5.1 Compute radiation parameters

5.5.1.1 General background

After removal of the components of the TOA reflectance due to whitecaps and sun glitter, and correcting for the two-way ozone absorption, the residual reflectance ρ_t can be written

$$\rho_t = \rho_r + \rho_a + \rho_{ra} + t\rho_w \tag{45}$$

where ρ_r is the reflectance resulting from scattering by air molecules (Rayleigh scattering) in the absence of the aerosol and ρ_a is the reflectance resulting from scattering by the aerosol in the absence of the air. The term ρ_{ra} is the interaction term between molecular and aerosol scattering. It accounts for photons first scattered by the air then scattered by aerosols, or photons first scattered by aerosols then air, etc. This term is zero in the single scattering case. In the last term, t is the diffuse transmittance of the atmosphere and ρ_w is the water-leaving reflectance (resulting from radiance backscattered out of the ocean). In producing the TOAC Dataset, $\rho_w = 0$, so $\rho_t = \rho_r + \rho_a + \rho_{ra}$. All of these reflectances are functions of the viewing-solar geometry (-μ, μ_0, ϕ - ϕ_0), where μ is a positive number, and the wavelength λ. If single scattering were the correct physics describing radiative transfer in the atmosphere, this equation would become

$$\rho_t = \rho_{rs} + \rho_{as} \tag{46}$$

where the additional subscript *s* signifies single scattering. Note that the term ρ_{ra} is missing, as this term results from multiple scattering. The single-scattered aerosol reflectance is given by

$$\rho_{as}(\lambda) = \frac{\varpi_a(\lambda)\tau_a(\lambda)p_a(-\mu, \mu_0, \phi - \phi_0;\lambda)}{4\mu} \tag{47}$$

where

$$p_a(-\mu, \mu_0, \phi - \phi_0;\lambda) = P_a(\Omega_1, \lambda) + [r(\mu_0) + r(\mu)](P_a(\Omega_2, \lambda)) \tag{48}$$

and

41

$$\cos\Omega_1 = -\mu\mu_0 + (1 - \mu^2)^{\frac{1}{2}}(1 - \mu_0^2)^{\frac{1}{2}}\cos(\phi - \phi_0)$$

$$\cos\Omega_2 = \mu\mu_0 + (1 - \mu^2)^{\frac{1}{2}}(1 - \mu_0^2)^{\frac{1}{2}}\cos(\phi - \phi_0) \tag{49}$$

and $r(\alpha)$ is the Fresnel reflectance of the interface for an incident angle $\cos^{-1}(\alpha)$. The parameters $\tau_a(\lambda)$, $\varpi_a(\lambda)$, and $P_a(\Omega,\lambda)$ are, respectively, the aerosol optical thickness, the aerosol single scattering albedo, and the aerosol scattering phase function for a scattering angle Ω.

5.5.1.2   Application to the TOAC Dataset

The TOAC Dataset relates $(\rho_a + \rho_{ra})/\mu_0$ to ρ_{as}/μ_0 for any given geometry ($-\mu$, μ_0, $\phi - \phi_0$) and MISR spectral band. As ρ_{as} is proportional to $\varpi_a\tau_a P_a$, it is seen that the TOAC Dataset provides the aerosol contribution to ρ_t as a function of the aerosol concentration (which is proportional to τ_a) and the aerosol model (specified by $\varpi_a P_a$).

To reduce the size of the TOAC Dataset, $\rho_a + \rho_{ra}$ is fitted using least squares to ρ_{as} according to

$$\log\frac{[\rho_a(\lambda) + \rho_{ra}(\lambda)]}{\mu_0} = a(\lambda) + b(\lambda)\log\frac{\rho_{as}(\lambda)}{\mu_0} + c(\lambda)\left[\log\frac{\rho_{as}(\lambda)}{\mu_0}\right]^2 \tag{50}$$

where $a(\lambda)$, $b(\lambda)$, and $c(\lambda)$ are functions of wavelength and the geometry, and the logarithms are base e. To further reduce storage, the azimuthal dependence of a, b, and c is handled using Fourier analysis, i.e.,

$$a(-\mu, \mu_0, \phi - \phi_0;\lambda) = a^{(0)}(-\mu, \mu_0;\lambda) + 2\sum_{m=1}^{M} a^{(m)}(-\mu, \mu_0;\lambda)\cos m(\phi - \phi_0) \tag{51}$$

where

$$a^{(m)}(-\mu, \mu_0;\lambda) = \frac{1}{\pi}\int_0^\pi a(-\mu, \mu_0, \phi - \phi_0;\lambda)\cos m(\phi - \phi_0)d\phi \tag{52}$$

with similar expressions for b and c.

Given a model of the aerosol, the required computations consist of the use of 1-D radiative transfer theory as described in §4.5.1.2.1. The vertical structure of the atmosphere consists of the

sea surface and the first two layers in Figure 4 in the absence of water vapor. Ozone is assumed to be in a separate absorbing layer above the second layer and is not included in the computations. Scalar RT theory is used, as polarization has a negligible effect on the relationship described by Eq. (50). (However, in application of the full atmospheric correction algorithm, ρ_r is required, and is computed using vector RT theory.) The molecular scattering optical depth τ_r is taken to be the sea-level value, as variations in τ_r induced by changes in the surface pressure ($\sim 1.5\%$) have a negligible effect on the fits obtained using Eq. (50). Unlike the computations described in §4.5.1.2.1, which use the doubling-adding method of solution of the RT equation, in preparation of the TOAC Dataset, the RT equation was solved using the successive-order-of-scattering method *[77]*. Typically, the pre-computed values of ρ_t (with $\rho_w = 0$) have uncertainties $\sim 0.1\%$. Given ρ_t, ρ_r is computed (also using scalar theory) to form

$$\rho_t - \rho_r = \rho_a + \rho_{ra} \tag{53}$$

This, along with ρ_{as} [see Eq. (47)], is then used to determine a, b, and c for the given geometry [see Eq. (50)]. Finally, the Fourier components $a^{(m)}(-\mu, \mu_0; \lambda)$, $b^{(m)}(-\mu, \mu_0; \lambda)$, and $c^{(m)}(-\mu, \mu_0; \lambda)$ are determined according to Eq. (52).

The parameter ρ_t is computed on a grid of $\tau_a(\lambda)$ values. For a given aerosol model, separate computations are required for each value of the geometric variables, the aerosol optical depth, and wavelength.

6. ANCILLARY LAND BIOME DATASET

6.1 PURPOSE

The Ancillary Land Biome Dataset consists of three files:

(1) *Biome Classification Map*: This file contains a geographic mapping of land surface classification into selected biome types, or barren. This classification is used as input to the default mode of the LAI/FPAR algorithm for the purpose of choosing the appropriate relationship for transforming Normalized Difference Vegetation Index (NDVI) into FPAR (see *[M-12]*).

(2) *Canopy Architecture Radiative Transfer (CART) file*: A look-up table (LUT) approach is used to rapidly model the radiative transfer process of complex canopy/soil models to determine hemispherically-integrated canopy/soil reflectances (used to determine LAI) and the corresponding FPAR's. This file contains radiative transfer parameters, describing transmittance and absorptance properties, for these canopy/soil models associated with the biome types of the Biome Classification Map.

(3) *NDVI-FPAR Regression Coefficients file:* This file contains the biome-dependent regression coefficients, relating the canopy NDVI to FPAR, and is used in conjunction with the Biome Classification Map to determine FPAR when in the default mode of the FPAR algorithm.

6.2 CONTENTS

The Biome Classification Map consists of 233 parts, corresponding to the 233 repeat orbits of the EOS spacecraft. The parameters in this product are reported in a Space-Oblique Mercator (SOM) map projection. The map scale of the projection is 1.1 km; this defines the horizontal sampling for each of the parameters. The horizontal datum, or surface-basis, for the projection is the WGS84 ellipsoid. This map projection and surface-basis is identical to what will be used for all the Level 1B2 and Level 2 parameters (see *[M-4]* and *[M-7]*).

Vegetated land covers are classified into six biome types, depending on their canopy structure. The biome structure attributes are parameterized in terms of variables used by radiative transfer models. The characteristics of the six biomes are as follows:

(1) Biome 1: Grasses and Cereal Crops. This biome is characterized by vertical and lateral homogeneity, large vegetation ground cover fraction, plant height less than a meter, erect leaf inclination, no woody material, leaf clumping and intermediate soil brightness.

(2) Biome 2: Shrublands. This biome is characterized by lateral heterogeneity, small to intermediate vegetation ground cover fraction, small leaves, woody material, and bright backgrounds. This land cover is typical of semi-arid regions with extreme hot or cold (tundra/taiga) temperature regimes and poor soils.

(3) Biome 3: Broadleaf Crops. This biome is characterized by lateral heterogeneity, large variations in fractional vegetation ground cover from crop planting to maturity, regular leaf spatial dispersion, photosynthetically active (i.e., green), stems, and dark backgrounds.

(4) Biome 4: Savanna. This biome is characterized by two distinct vertical layers, understory is grass (Biome 1), low fractional ground cover of overstory trees, canopy optics and structure therefore vertically heterogeneous. Savannas in the tropical and sub-tropical regions are characterized as mixtures of warm grasses and broadleaf trees. In the cooler regions at higher latitudes, they are described as mixtures of cool grass and needle trees.

(5) Biome 5: Broadleaf Forests. This biome is characterized by vertical and lateral heterogeneity, complete vegetation ground cover, green understory, mutual shadowing by crowns, foliage clumping, variable crown heights, and includes randomly oriented trunks and branches which make canopy structure spatially variable.

(6) Biome 6: Needle Forests. This biome is characterized by needle clumping on shoots, severe shoot clumping in whorls, dark vertical trunks, sparse green understory, crown mutual shadowing, branches randomly oriented.

Non-vegetated land is classified as barren. Finally, the Biome Classification Map, being a continuous pole-to-pole file, contains areas that are covered by ocean, inland water, or coastline. These are classified as not_land.

Table 8: Biome Classification Map Contents

Parameter name	Description	Units
Geographic latitude	Geodetic latitude coordinate of the center of the SOM grid location	deg
Geographic longitude	Geodetic longitude coordinate of the center of the SOM grid location	deg
Surface type	One of six vegetation classes, barren, or not_land	none

The parameters in the Canopy Architecture Radiative Transfer file are listed in Table 9. Those parameters dependent on solar zenith angle are evaluated at 4 angles, 15°, 30°, 45°, and 60°, and are representative values for the angle bins 0°-22.5°, 22.5°–37.5°, 37.5°–52.5°, and 52.5°-70°, respectively. Likewise, those parameters dependent on view zenith angle are evaluated at 6 angles, 4°, 15°, 30°, 45°, 60°, and 70°, representative of the angle bins 0°-8.5°, 8.5°-22.5°, 22.5°-37.5°, 37.5°-52.5°, 52.5°-67.5°, and 67.5°-72.5°. Finally, those parameters dependent on relative azimuth angle are also evaluated at 6 angles, 10°, 40°, 70°, 100°, 130°, and 160°, representative of the angle bins 0°-25°, 25°-55°, 55°-85°, 85°-115°, 115°-145°, and 145°-180°.

Table 9: Contents of CART file

Parameter	Description	Units
LAI parameters		
bio	Biome identification number	none
N_{LAI}	Number of LAI values per canopy model	none
LAI	N_{LAI} leaf area indices (between 0.1 and 9.85)	none
Reference soil model parameters		
bio	Biome identification number	none
N_{soil}	Number of soil models	none
soil	Soil identification number	none
ρ_{eff}^{q}	Effective soil reflectance in 4 MISR bands	none
Reference leaf albedos		
bio	Biome identification number	none
ϖ^{*}	Reference leaf albedo (= 0.02)	none
ϖ	Leaf albedos in 4 MISR bands	none
Reference canopy model parameters for a black soil and S problem		
N_{sun}	Number of solar zenith angles (= 4)	none
sun_zen	Solar zenith angles (15., 30., 45., 60.)	deg
N_{view}	Number of view zenith angles (= 6)	none
view_zen	View zenith angles (4., 15., 30., 45., 60., 70.)	deg
N_{azim}	Number of view-sun azimuth angle differences (= 6)	none
azimuth	Azimuth angles (10., 40., 70., 100., 130., 160.)	deg
bio	Biome identification number	none
lai	LAI identification number	none
$\mathbf{t}_{bs}^{dir^{*},\, q \equiv 1}$	Hemispherical downward transmittances for reference leaf albedo ϖ^{*} and direct incident irradiances at 4 solar zenith angles	none
$\mathbf{t}_{bs}^{diff^{*},\, q \equiv 1}$	Hemispherical downward transmittances for reference leaf albedo ϖ^{*} and diffuse incident irradiances at 4 solar zenith angles	none

Parameter	Description	Units
$\mathbf{t}_{bs}^{dir^*, q}$	Weighted hemispherical downward transmittances for the reference leaf albedo ϖ^* and direct incident irradiances at 4 solar zenith angles	none
$\mathbf{t}_{bs}^{diff^*, q}$	Weighted hemispherical downward transmittances for the reference leaf albedo ϖ^* and diffuse incident irradiances at 4 solar zenith angles	none
$\mathbf{a}_{bs}^{dir^*}$	Fraction of radiation absorbed by the canopy for the reference leaf albedo ϖ^* and direct incident irradiances at 4 solar zenith angles	none
$\mathbf{a}_{bs}^{diff^*}$	Fraction of radiation absorbed by the canopy for the reference leaf albedo ϖ^* and diffuse incident irradiances at 4 solar zenith angles	none
$\mathbf{t}^{q^*}$	Hemispherical upward transmittance for the reference leaf albedo ϖ^* and a source located at the canopy bottom	none
$\mathbf{a}^{q^*}$	Fraction of radiation absorbed by the canopy for the reference leaf albedo ϖ^* and a source located at the canopy bottom	none
$\mathbf{pt}_{bs}^{dir}$	Solution of the minimization problem described by Eq. (123) for the "black soil problem" with direct incoming solar radiation at 4 solar zenith angles	none
$\mathbf{pt}_{bs}^{diff}$	Solution of the minimization problem described by Eq. (123) for the "black soil problem" with direct incoming solar radiation at 4 solar zenith angles	none
$\mathbf{pt}$	Solution of the minimization problem described by Eq. (123) for the "S problem"	none
$\mathbf{pa}_{bs}$	Solution of the minimization problem described by Eq. (122) for the "black soil problem"	none
$\mathbf{pa}$	Solution of the minimization problem described by Eq. (122) for the "S problem"	none
$w_{bs, \lambda}^{dir}$	BRF weights in 4 MISR bands at 4 solar zenith angles, 6 view zenith angles, and 6 azimuth angles	none
w_{λ}^{q}	BRF weights in 4 MISR bands at 6 view zenith angles	none
Algorithm parameters for Biome/LAI determination		
bio	Biome identification number	none
N_{sat}	Number of saturation function values	none
L^*	N_{sat} mean LAI saturation function values, described by Eq. (135)	none
d^*	N_{sat} dispersion saturation function values, described by Eq. (136)	none

Parameter	Description	Units
lai	LAI identification number	none
$W_{1,\lambda}$	First component of BRF [defined in Eq. (161)] in 4 MISR bands, at 4 solar zenith angles, 6 view zenith angles and 6 azimuth angles	none
$W_{2,\lambda}$	Second component of BRF [defined in Eq. (162)] in 4 MISR bands and at 6 view zenith angles	none
soil	Soil identification number	none
$A_{model,\lambda}^{dir}$	Canopy/soil DHR [defined in Eq. (94)] in 4 MISR bands and at 4 solar zenith angles	none
$A_{model,\lambda}^{diff}$	Diffuse light component of canopy/soil BHR [defined in Eq. (157)] in 4 MISR bands and at 4 solar zenith angles	none
Algorithm parameters for FPAR determination		
bio	Biome identification number	none
lai	LAI identification number	none
$\mathbf{r}_{bs,\lambda}^{dir}$	Black soil direct irradiance canopy hemispherical reflectance [defined in Eq. (128)] in first 3 MISR bands and at 4 solar zenith angles	none
$\mathbf{r}_{bs,\lambda}^{diff}$	Black soil diffuse irradiance canopy hemispherical reflectance [defined in Eq. (158)] in first 3 MISR bands and at 4 solar zenith angles	none
T_{λ}^{dir}	Direct irradiance component of test parameter [defined in Eq. (172)] in first 3 MISR bands and at 4 solar zenith angles	none
T_{λ}^{diff}	Diffuse irradiance component of test parameter [defined in Eq. (173)] in first 3 MISR bands and at 4 solar zenith angles	none
$F_{1,\lambda}^{dir}$	Direct irradiance component of canopy absorptance [defined in Eq. (167)] in first 3 MISR bands and at 4 solar zenith angles	none
$F_{1,\lambda}^{diff}$	Diffuse irradiance component of canopy absorptance [defined in Eq. (168)] in first 3 MISR bands and at 4 solar zenith angles	none
$F_{2,\lambda}$	BRF-dependent component of canopy absorptance [defined in Eq. (169) in first 3 MISR bands	none
$\hat{w}_{\lambda}$	Solar spectrum weights in first 3 MISR bands	none

The identification number *bio* indexes biome types, defined as

bio = 1: grasses and cereal crops

bio = 2: shrublands

bio = 3: broadleaf crops

bio = 4: savanna

bio = 5: broadleaf forests

bio = 6: needle leaf forests.

The identification number *lai* indexes LAI values for biome-dependent canopy models.

The identification number *soil* indexes the biome-dependent effective soil/understory reflectances.

The parameters in the NDVI-FPAR Regression Coefficients file are listed in Table 10. The regression coefficients depend only on the biome type and the solar zenith angle. The three solar zenith angles are set at 30, 45, and 60°, covering most of the MISR sun geometry

Table 10: Contents of the NDVI-FPAR Regression Coefficients file

Parameter	Description	Units
bio	Biome identification number	none
F_0	1st regression coefficients at 3 solar zenith angles	none
F_1	2nd regression coefficients at 3 solar zenith angles	none

6.3 PROCESSING OUTLINE

Figure 8 shows conceptually the processes involved in the generation of the ALB Dataset.
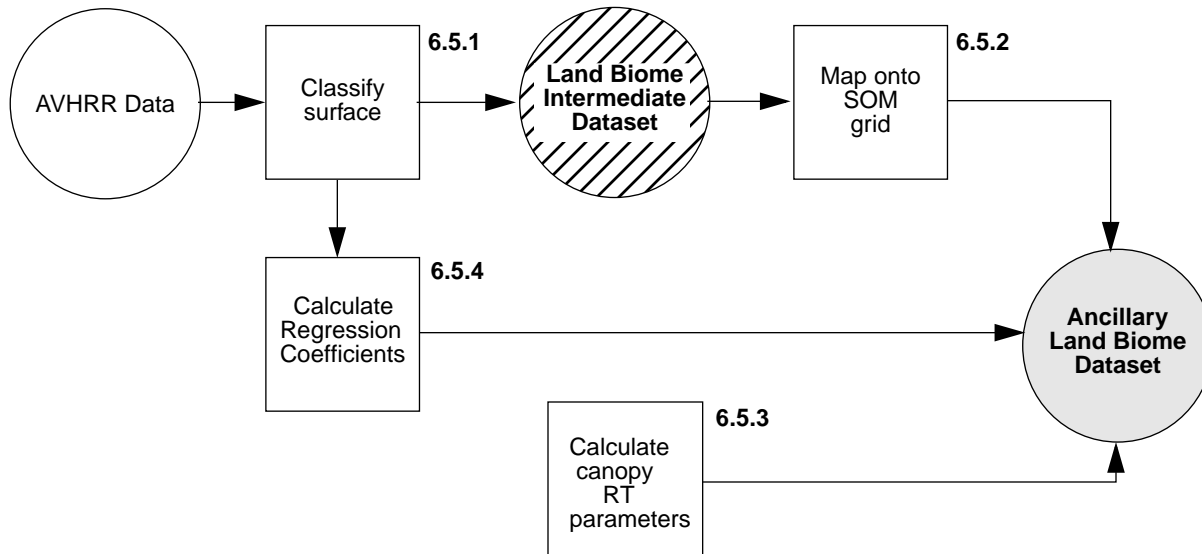
Figure 8. Conceptual processing flow for generation of the ALB Dataset

6.4 INPUT DATA

The Biome Classification Map of the Ancillary Land Biome Dataset is to be generated after launch once the specific geographic locations of the EOS orbit swaths are known. An intermediate, global dataset is created in the interim to store the land biome classification data. The Land Biome Intermediate Dataset (LBID) is currently generated from monthly composite 1-km AVHRR pathfinder data. The NDVI-FPAR regression coefficients file also requires the AVHRR dataset to compute the NDVI. The other files in the ALB require no input data.

6.5 THEORETICAL BASIS

6.5.1 Classify surface

The land cover classification used to generate the LBID is performed as follows. First, NDVI is determined and an NDVI threshold is used to separate vegetated and non-vegetated regions. Vegetated regions are then divided into tropical, temperate, and boreal zones, depending on the duration of the freezing period. Within each of these zones forested regions are separated from non-forested regions, based on the magnitude of the NDVI at maximum surface temperature. The forested regions in the temperate and boreal zones are further separated into leaf and needle forests, based on the magnitude of the near-IR reflectance at maximum NDVI. The non-forested regions, on the other hand, are classified as savanna, broadleaf crops, shrublands, and grasses/cereals, depending on the magnitude of the red reflectance at maximum NDVI. A classification map for the

50

conterminous U.S. generated by applying this methodology to 1-km AVHRR data was made and was found to be in good agreement with that of Loveland et al. *[42]*. The latter classification used an extensive amount of ancillary information and therefore can be considered as ground truth.

6.5.2   Map onto SOM grid

Once the actual SOM grid to be used for MISR Level 1B2 and Level 2 products is established, the LBID data are mapped onto the 233 orbits at 1.1-km sampling using a resampling procedure. The resulting datasets constitute the Ancillary Land Biome Dataset. The creation of the intermediate LBID and the mapping onto the SOM to create the ALB Dataset is analogous to the creation of the DEM Intermediate Dataset (DID), a global map of surface elevations, which is then mapped onto the SOM grid to generate certain parameters within the Ancillary Geographic Product (AGP). Further description of this process is presented in *[M-7]*.

6.5.3   Calculate canopy radiative transfer parameters

6.5.3.1   Physics of the problem

Fundamental to the operation of the LAI/FPAR retrieval algorithm is the ability to compute accurate spectral transmittances, reflectances and absorptances for the various biome/canopy models through the use of the Canopy Architecture Radiative Transfer (CART) file. In turn, the generation of this file requires the capability of simulating radiation scattering and absorption within the complex 3-dimensional canopies which are indicative of the six biome types. Initial modeling efforts were concerned with horizontally homogeneous canopies (i.e., one-dimensional radiative transfer) to simulate radiation interactions in broadleaf crops and grasslands. The governing transport equations were numerically evaluated by the modified discrete ordinates method with considerable attention being paid to the derivation of appropriate scattering phase functions. The methods were benchmarked by comparing model results with published solutions and with field measurements of vegetation canopy reflectance *[70]*. The model has also been numerically inverted with considerable success *[60]* and validated by Privette *[59]* with atmospherically corrected AVHRR data over FIFE sites. A formulation of the three-dimensional radiative transfer equation, the constituent interaction coefficients, its numerical solution, and results on model comparison with reflectance measurements of a hardwood forest are given in *[51]*. The 3-D method was also validated extensively against shrublands reflectance measurements from the HAPEX-SAHEL field experiment and found to reproduce well the non-linear canopy-soil interaction in sparse canopies *[5]*. More recent model developments allow for leaf clumping (the simulation of clumped, random and regular leaf dispersions in space) to be included in the formulation of the extinction and differential scattering coefficients. Also included in the current version of the model is the ability to simulate vertical tree trunks, randomly oriented branches, and the absence of light transmission through the trunks and branches, which imbues an asymmetry aspect critical to the simulation of surface HDRF's in forest canopies. Radiation interaction coefficients for the ensemble of leaves and

trunks/branches now are derived as linear mixtures with weighting proportional to their areal fraction. The hot spot model of Pinty et al. *[57]* also has been implemented in the radiative transfer formulation. This is perhaps the most realistic model of the hot spot effect and is driven by the average gap size between leaves in a canopy. In forest canopies, however, where tree crowns mutually shade one another, crown shadows according to Li and Strahler *[40]* have been implemented as the driver of the hot spot effect. Finally, for the case of coniferous canopies, geometric models of needle clumping on shoots and shoot clumping in whorls, are included according to a formulation developed by Oker-Blum et al. *[55]*. How these modeling techniques are used to compute the parameters in the CART file is described next.

6.5.3.2   Radiation transport in a canopy

The domain V in which a plant canopy is located is a parallelepiped of dimension $X_S = Y_S =$ 1.1 km and biome-dependent height Z_S. The domain V can contain sub-domains (or fine cells) whose size depends on the heterogeneity of the biome type. The top δV_t, bottom δV_b, and lateral δV_l surfaces of the parallelepiped form the canopy boundary, $\delta V = \delta V_t + \delta V_b + \delta V_l$. Note that the boundary δV is excluded from the definition of the domain V *[18]*. The function characterizing the radiation field is the monochromatic radiance L_λ which is a function of wavelength λ, location $r = (x, y, z)$, view direction Ω, and Sun direction Ω_0. In the absence of polarization, frequency shifting interactions, and emission processes within the canopy, the monochromatic radiance is given by the steady-state radiative transfer equation,

$$\Omega \bullet \nabla L_\lambda(r, \Omega, \Omega_0) + \sigma(r, \Omega)L_\lambda(r, \Omega, \Omega_0) = \int_{4\pi} \sigma_{s, \lambda}(r, \Omega' \to \Omega)L_\lambda(r, \Omega', \Omega_0)d\Omega'$$

$$+ F_\lambda(r, \Omega, \Omega_0)$$

(54)

where $\Omega \bullet \nabla$ is a derivative at r along the direction Ω. Note that there is a term F_λ in this equation which accounts for the hot spot effect: all current canopy radiation models are described by an equation of this form. A choice of F_λ depends on the model used to simulate the hot spot effect and it is assumed to be known. We should note that F_λ may take on negative values. Thus, Eq. (54) is a closed mathematical equation (not a "physical equation") used as a theoretical basis to build and justify an algorithm for LAI/FPAR retrieval. Such equations also arise in reactor problems and so we will closely follow some methods from this discipline *[18]*, *[78]*.

The position vector r denotes the Cartesian coordinates triplet (x, y, z) with $(0 < x < X_S)$, $(0 < y < Y_S)$ and $(0 < z < Z_S)$ with its origin, $O = (0, 0, 0)$, at the top of the canopy. A right-handed coordinate system is used in which the z-axis is aligned with the normal to the Earth's ellipsoid and pointing downward, and the x-axis is aligned with a great circle and points towards the north pole. The Sun angle is defined with respect to the outward normal to the surface ellipsoid. The same normal is used as the polar axis to express a unit direction, $\Omega = (\mu, \phi)$, within the vegetation layer. This

means that within the vegetation layer, the cosine of the polar (zenith) angle takes on negative values for the downward direction and positive ones for the upward direction of radiation travel.

The function σ (in m^{-1}) is the total interaction cross-section which does not depend on wavelength and $\sigma_{s,\lambda}$ (in m^{-1}sr^{-1}) is the differential scattering cross-section from the direction Ω' into a differential solid angle about Ω at r. In canopy transport theory these coefficients are defined as [50], [63]

$$\sigma(r, \Omega) = u_L(r)G(r, \Omega) = u_L(r)\frac{1}{2\pi}\int_{2\pi+} g_L(r, \Omega_L)|\Omega \bullet \Omega_L| d\Omega_L \tag{55}$$

$$\sigma_{s,\lambda}(r, \Omega' \to \Omega) = u_L(r)\frac{1}{\pi}\Gamma_\lambda(r, \Omega' \to \Omega)$$

$$= u_L(r)\frac{1}{2\pi}\int_{2\pi+} g_L(r, \Omega_L)|\Omega' \bullet \Omega_L|\gamma_{L,\lambda}(r, \Omega_L, \Omega' \to \Omega)d\Omega_L \tag{56}$$

where u_L (in m^{-1}) is the leaf area density distribution function, G (dimensionless) is the mean projection of leaf normals at r onto a plane perpendicular to the direction Ω, g_L is the probability density of the leaf normal distribution over the upper hemisphere $2\pi+$, $\gamma_{L,\lambda}$ (in sr^{-1}) is the leaf scattering phase function, and Γ_λ is the area scattering phase function. The precise description of these variables can be found in the literature [50], [63]. The leaf area index LAI is defined as

$$LAI = \frac{1}{X_S \cdot Y_S}\int_V u_L(r)dr \tag{57}$$

Equation (54) alone does not provide a full description of the transport process. It is necessary to specify the incident radiance at the canopy boundary δV, i.e., specification of the boundary conditions. Because our plant canopy is adjacent to the atmosphere, neighboring canopies, and the soil, all which have different reflection properties, the following boundary conditions will be used to describe the incoming radiation [65]:

$$L_\lambda(r_t, \Omega, \Omega_0) = L_{d,\lambda}^{top}(r_t, \Omega, \Omega_0) + L_{m,\lambda}^{top}(r_t)\delta(\Omega - \Omega_0), \qquad r_t \in \delta V_t, \ \Omega \bullet n_t < 0 \tag{58}$$

$$L_\lambda(r_l, \Omega, \Omega_0) = \frac{1}{\pi}\int_{\Omega' \bullet n_l > 0} R_{l,\lambda}(\Omega', \Omega)L_\lambda(r_l, \Omega', \Omega_0)|\Omega' \bullet n_l| d\Omega'$$

$$+ L_{d,\lambda}^{lat}(r_l, \Omega, \Omega_0) + L_{m,\lambda}^{lat}(r_l)\delta(\Omega - \Omega_0), \qquad r_l \in \delta V_l, \ \Omega \bullet n_l < 0 \tag{59}$$

53

$$L_\lambda(r_b, \Omega, \Omega_0) = \frac{1}{\pi} \int\limits_{\Omega' \bullet n_b > 0} R_{b,\lambda}(\Omega', \Omega) L_\lambda(r_b, \Omega', \Omega_0) |\Omega' \bullet n_b| d\Omega, \qquad r_b \in \delta V_b, \ \Omega \bullet n_b < 0$$

$$(60)$$

where $L_{d,\lambda}^{top}$ and $L_{m,\lambda}^{top}$ are the diffuse and monodirectional components of solar radiation incident on the top surface of the canopy boundary δV_t; $\Omega_0 = (\mu_0, \phi_0)$ is the direction of the monodirectional solar component; δ is the Dirac delta-function; $L_{m,\lambda}^{lat}$ is the intensity of the monodirectional solar radiation arriving at a point $r_l \in \delta V_l$ along Ω_0 without experiencing an interaction with the neighboring canopies; $L_{d,\lambda}^{lat}$ is the diffuse radiation penetrating through the lateral surface δV_l; $R_{l,\lambda}$ and $R_{b,\lambda}$ (in sr^{-1}) are the bidirectional reflectance factors of the lateral and the bottom surfaces, respectively; and n_t, n_l and n_b are the outward normals at points $r_t \in \delta V_t$, $r_l \in \delta V_l$ and $r_b \in \delta V_b$, respectively. A solution of the boundary value problem, expressed by Eqs. (54) - (60) describes the radiation regime in a plant canopy.

6.5.3.2.1 Assumptions

Conservativity. A radiative transfer model is defined to be conservative if the energy conservation law holds true for any elementary volume *[3]*. Within a conservative model, the radiation absorbed, transmitted and reflected by the canopy is always equal to the radiation incident on the canopy. A rather wide family of canopy-radiation models which account for the hot spot are equivalent to the solution of the above boundary value problem in which the function F_λ has the form,

$$F_\lambda(r, \Omega, \Omega_0) = [\sigma(r, \Omega) - \sigma_H(r, \Omega, \Omega_0)] L_{H,\lambda}(r, \Omega, \Omega_0) \tag{61}$$

Here, $L_{H,\lambda}$ is the upward directed, once-scattered radiance produced by the hot spot, and σ_H is a model-dependent, total interaction cross-section, introduced in canopy radiation models to account for the hot spot and to evaluate $L_{H,\lambda}$. The total interaction cross-section σ is used to evaluate the attenuation of both the direct solar radiance and the multi-scattered radiance. Because F_λ can take on negative values, it has no physical meaning in the sense of an energy conservation law. These types of canopy-radiation models are mainly used to fit simulated BRF's to measured BRF's. However, the capacity of a model to simulate the canopy reflection is not sufficient to solve the inverse problem. Inverted canopy-radiation models must also satisfy energy conservation and provide the correct proportions between canopy absorptance, transmittance and reflectance. Because our retrieval algorithm is based on energy conservation, we formulate the following "minimum" requirements of the canopy-radiation models used to generate the CART parameters,

$$\int\limits_V dr \int\limits_{4\pi} F_\lambda(r, \Omega, \Omega_0) d\Omega = 0, \qquad\qquad r \in V$$

$$(62)$$

for any λ. These equations do not allow a "non-physical source" F_λ to influence the canopy solar

energy balance. Currently we use a model for σ_H proposed in Myneni et al. *[52]* which is modified as described in §6.5.3.6. *A non-conservative canopy radiation model can not be used to generate the CART file parameters for our LAI/FPAR retrieval algorithm.*

Anisotropy of incoming diffuse radiation. A model of the clear sky proposed by Pokrowski *[58]* is used to simulate the ratio between the angular distribution of incoming diffuse radiation and its flux,

$$\frac{L_{d,\lambda}^{top}(r_t, \Omega, \Omega_0)}{\int\limits_{2\pi^-} L_{d,\lambda}^{top}(r_t, \Omega, \Omega_0)|\mu|d\Omega} = \left[1 - \exp\left(\frac{-0.32}{|\mu|}\right)\right]\frac{1 + \Omega \bullet \Omega_0}{1 - \Omega \bullet \Omega_0}, \qquad \mu < 0 \tag{63}$$

We assume that this ratio does not depend on wavelength. The diffuse radiation $L_{d,\lambda}^{top}$ also does not depend on the top boundary space point $r_t \in \delta V_t$.

Optical properties of the foliage. The leaf scattering phase function $\gamma_{L,\lambda}$ is assumed to be bi-Lambertian *[64]*, i.e. a fraction of the energy intercepted by the foliage element is reflected or transmitted in a cosine distribution about the leaf normal,

$$\gamma_{L,\lambda}(r, \Omega_L, \Omega' \to \Omega) = \frac{1}{\pi}r_{D,\lambda}(r)|\Omega \bullet \Omega_L|, \qquad (\Omega \bullet \Omega_L)(\Omega' \bullet \Omega_L) < 0$$

$$= \frac{1}{\pi}t_{D,\lambda}(r)|\Omega \bullet \Omega_L|, \qquad (\Omega \bullet \Omega_L)(\Omega' \bullet \Omega_L) > 0 \tag{64}$$

Here $r_{D,\lambda}$ and $t_{D,\lambda}$ are the spectral reflectance and transmittance, respectively, of the leaf element and they depend on wavelength and the space point r. Figure 9 shows an example of the sensitivity of the one-year shoot (*Picea abies* (L) Karst) spectral reflectance $r_{D,\lambda}$ to its location in space. In spite of this spatial variation, shapes of the spectral reflection and the spectral transmittance are rather stable. For example, if we compare the spectral curves of Figure 9 with its mean spectral variations taken over space points, then the deviation is, on average, about 12-15% which does not exceed the accuracy of the models *[37]*. Therefore, we ignore the spatial variation of foliage optical properties in our calculations. Our algorithm will be parameterized in terms of spectral leaf albedo,

$$\varpi(\lambda) = r_{D,\lambda} + t_{D,\lambda} \tag{65}$$

For each biome, the mean spectral leaf albedo is assumed to be known and archived in the CART file.
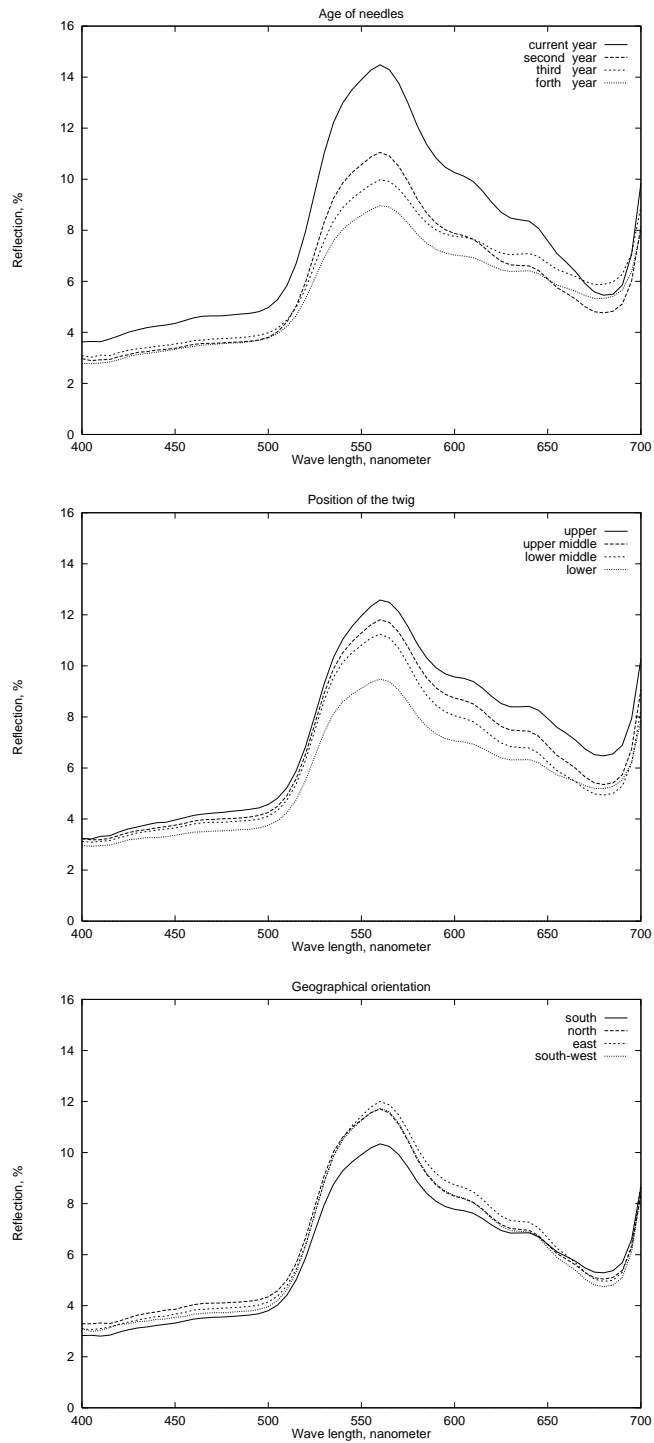
Figure 9. The spectral reflectance of spruce one-year shoots derived from measurements. Three characteristics of the shoots were chosen to study the spatial variations of foliage spectral properties - age of the needles on the one-year shoot (top), position within the tree crown (middle), and geographical orientation with respect to the tree stem (bottom)

Grasses/cereal crops and broad leaf crops. We idealize these vegetation canopies as a horizontally homogeneous medium. The total interaction cross-section σ, the differential scattering cross-section $\sigma_{s,\lambda}$, and the function F_λ [defined by Eq. (61)] depend only on the vertical coordinate and direction and are given by

$$\sigma(r, \Omega) = u_L(z)G(\Omega) \tag{66}$$

$$\sigma_{s,\lambda}(r, \Omega' \to \Omega) = u_L(z)\frac{1}{\pi}\Gamma_\lambda(z, \Omega' \to \Omega) \tag{67}$$

$$LAI = \int_0^{z_s} u_L(z)dz \tag{68}$$

The area scattering phase function Γ_λ describes erectophile (grasses/cereal crops) or uniform (broadleaf crops) types of leaf orientation. The boundary condition described by Eq. (59) for the lateral surface δV_l can be omitted and the operator $\Omega \bullet \nabla$ takes the form $-\mu \cdot \partial/\partial z$ in this case.

Remaining biome types. The radiation penetrating through the lateral sides of the canopy depends on the neighboring environment. Its influence on the radiative field within the canopy is especially pronounced near the lateral canopy boundary. Therefore, inaccuracies in the lateral boundary conditions may cause distortions in the simulated radiation field in this domain. These distortions, however, decrease with distance from this boundary towards the center of the domain *V*. The size dependence of the "distorted area" on adjoining vegetation, on the atmospheric conditions, and the model resolution, induced by utilizing our current approach, was studied by Kranigk *[39]*. In particular, it has been shown that these lateral side effects can be neglected when the radiative regime is analyzed in a rather extended canopy. Therefore, we idealize our canopy as a horizontally infinite region. We will use the "vacuum" boundary condition for the lateral surface to numerically evaluate a solution for the case of horizontally infinite domain,

$$L_\lambda(r_l, \Omega, \Omega_0) = 0, \qquad r_l \in \delta V_l, \ \Omega \bullet n_l < 0 \tag{69}$$

Soil reflectance. The bidirectional soil reflectance factor $R_{b,\lambda}$ is horizontally homogeneous, i.e., it does not depend on the space point r_b.

All calculations to evaluate the parameters in the CART file were made under the above assumptions. We note that these assumptions were verified by comparison of our three-dimensional simulation results with field measurements *[37]*.

6.5.3.3 Soil reflectance

To parameterize the contribution of soil to the canopy-radiation regime, we introduce an effective soil reflectance as

$$
\rho_{eff,\lambda}^{q}(r_b) = \frac{1}{\pi} \cdot \frac{\dfrac{1}{\pi} \displaystyle\int_{2\pi-}\int_{2\pi+} R_{b,\lambda}(\Omega',\Omega)|\mu\mu'|L_\lambda(r_b,\Omega',\Omega_0)d\Omega d\Omega'}{\dfrac{1}{\pi}\displaystyle\int_{2\pi-} q(\Omega')|\mu'|L_\lambda(r_b,\Omega',\Omega_0)d\Omega'}, \qquad r_b \in \delta V_b, \ \Omega \bullet n_b < 0
$$
.(70)

Here L_λ is the solution of the boundary value problem for the transport equation. The function q is a configurable function to "tune" the CART file parameters without modifying the algorithm. Note that the effective soil reflection depends on the canopy structure as well as on the incoming radiation. However, as follows from the above definition, the variation of $\rho_{eff,\lambda}^{q}$ satisfies the following inequality,

$$
\min_{\Omega' \in 2\pi-} \frac{1}{\pi} \cdot \frac{\displaystyle\int_{2\pi-} R_{b,\lambda}(\Omega',\Omega)|\mu|d\Omega}{q(\Omega')} \leq \rho_{eff,\lambda}^{q}(r_b) \leq \max_{\Omega' \in 2\pi-} \frac{1}{\pi} \cdot \frac{\displaystyle\int_{2\pi-} R_{b,\lambda}(\Omega',\Omega)|\mu|d\Omega}{q(\Omega')} \tag{71}
$$

i.e., the range of variations depends on the integrated bidirectional soil reflectance factor only. This property in part allows us to formulate the following assumptions.

6.5.3.3.1 *Assumptions*

Effective soil reflectance homogeneity. For each biome, the effective soil reflectance does not depend on the space point $r_b \in \delta V_b$.

Spectral dependence. The pattern of the effective soil reflectances $\rho_{eff,\lambda}^{q}$ for each biome in the MISR spectral bands can be found in the CART file. The current version contains 29 effective soil reflectance patterns shown in Fig. 10, evaluated from the model of Jacquemoud et al. *[33]* with model inputs from Baret et al. *[2]*, which represent dark, medium, and bright soils.
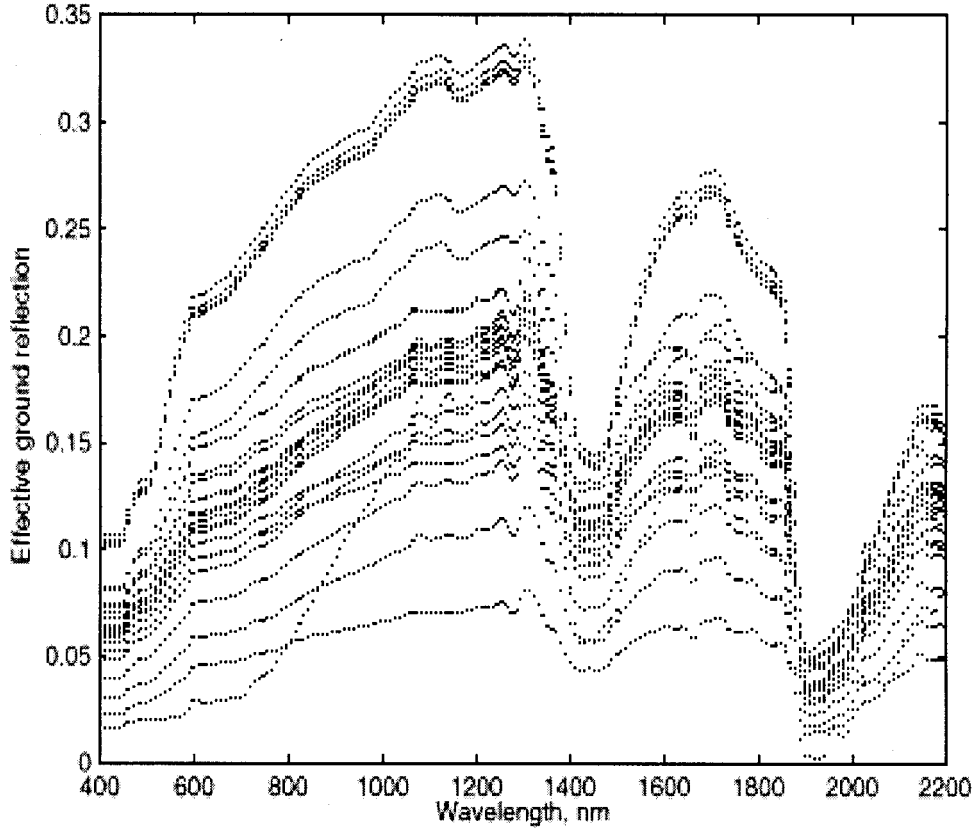
Figure 10. Spectral effective ground reflectance for 29 different soils. It includes three soil types described as mixtures of clay, sand, and peat. Each type is characterized by three moisture levels (wet, medium, and dry) and from two to three levels of soil roughness (rough, medium, smooth or rough and smooth).

Soil anisotropy. To account for soil anisotropy, we introduce an effective soil anisotropy,

$$S^q(r_b, \Omega) = \frac{1}{\rho^q_{eff,\lambda}(r_b)} \cdot \frac{1}{\pi} \cdot \frac{\frac{1}{\pi}\int\limits_{2\pi-} R_{b,\lambda}(\Omega', \Omega)|\mu'|L_\lambda(r_b, \Omega', \Omega_0)d\Omega'}{\frac{1}{\pi}\int\limits_{2\pi-} q(\Omega')|\mu'|L_\lambda(r_b, \Omega', \Omega_0)d\Omega'}, \qquad r_b \in \delta V_b, \ \Omega \bullet n_b < 0$$

$$(72)$$

The effective soil anisotropy S^q depends on the canopy structure as well as on the incoming radiation. We note the following property of this parameter:

59

$$\int\limits_{2\pi+} S^q(r_b, \Omega)|\mu|\,d\Omega \ = \ 1 \tag{73}$$

i.e., the integral in Eq. (73) depends neither on spatial nor spectral variables. For each biome type, the effective soil anisotropy does not depend on wavelength.

For grasses/cereal crops and broadleaf crops, the soil reflectance is assumed lambertian. We also set $q = 1$. The effective soil reflection and soil anisotropy then have the form,

$$\rho^q_{eff,\lambda}(r_b) \ = \ R_{lam,\lambda}$$
$$S^q(r_b, \Omega) \ = \ 1/\pi \tag{74}$$

For shrublands and savanna we represent the bidirectional soil reflectance factor as

$$R_{b,\lambda}(\Omega', \Omega) \ = \ R_1(\Omega')R_2(\Omega) \tag{75}$$

and we set

$$q(\Omega') \ = \ R_1(\Omega')/\rho_1^* \tag{76}$$

The effective soil reflection and soil anisotropy then have the form

$$\rho^q_{eff,\lambda}(r_b) \ = \ \rho_1^*\rho_2^*$$
$$S^q(r_b, \Omega) \ = \ \frac{1}{\pi} \cdot \frac{R_2(\Omega)}{\rho_2^*}$$
$$. \tag{77}$$

where

$$\rho_1^* \ = \ \frac{1}{\pi}\int\limits_{2\pi-} R_1(\Omega')|\mu'|\,d\Omega'$$
$$\rho_2^* \ = \ \frac{1}{\pi}\int\limits_{2\pi-} R_2(\Omega')|\mu'|\,d\Omega' \tag{78}$$

These biomes are characterized by a relative small value of ground cover (0.2 - 0.6 and 0.2 - 0.4). The use of the above model for the bidirectional soil reflectance factor means that only the incoming direct beam of solar radiation which reaches the soil can influence the anisotropy of the

radiation field in the plant canopy.

Finally, for needle forests and broadleaf forests, we must solve the transport equation, described by Eqs. (54) - (60), to evaluate the effective soil reflectance and soil anisotropy as a function of LAI and sun position. Note that these are intermediate calculations and are used to precompute some parameters stored in the CART file.

6.5.3.4   Basic algorithm equations

It follows from the linearity of Eq. (54) that its solution can be represented by the following sum

$$L_\lambda(r, \Omega, \Omega_0) = L_{bs, \lambda}(r, \Omega, \Omega_0) + L_{rest, \lambda}(r, \Omega, \Omega_0) \tag{79}$$

Here $L_{bs, \lambda}$ is the solution of the "black soil problem" which satisfies Eq. (54) with boundary conditions expressed by Eqs. (58) and (69), and

$$L_{bs, \lambda}(r_b, \Omega, \Omega_0) = 0, \qquad r_b \in \delta V_b, \ \Omega \bullet n_b < 0 \tag{80}$$

The function $L_{rest, \lambda}$ also satisfies Eq. (54) with $F_\lambda = 0$ and boundary conditions expressed by Eq. (69) and

$$L_{rest, \lambda}(r_t, \Omega, \Omega_0) = 0, \qquad r_t \in \delta V_t, \ \Omega \bullet n_t < 0 \tag{81}$$

$$L_{rest, \lambda}(r_b, \Omega, \Omega_0) = \frac{1}{\pi} \int_{\Omega' \bullet n_b > 0} R_{b, \lambda}(\Omega', \Omega) L_\lambda(r_b, \Omega', \Omega_0) \big| \Omega' \bullet n_b \big| d\Omega', \quad r_b \in \delta V_b, \ \Omega \bullet n_b < 0 \tag{82}$$

Note that $L_{rest, \lambda}$ depends on the solution of the "whole transport problem". Taking into account Eq. (72), we can rewrite Eq. (82) as

$$L_{rest, \lambda}(r_b, \Omega, \Omega_0) = \rho_{eff, \lambda}^q(r_b) \cdot S^q(r_b, \Omega) \cdot T_\lambda^q(r_b, \Omega_0) \tag{83}$$

where

$$T_\lambda^q(r_b, \Omega_0) = \int_{2\pi-} q(\Omega') |\mu'| L_\lambda(r_b, \Omega', \Omega_0) d\Omega'. \tag{84}$$

61

6.5.3.4.1 Assumptions

We replace T_λ^q in Eq. (83) by its mean over the soil surface. This implies that the variable T_λ^q is independent of the space point r_b. (This assumption is automatically fulfilled if a one-dimensional radiative transfer model is used to evaluate the radiation field in plant canopies). Thus, the boundary condition can be rewritten as

$$L_{rest,\,\lambda}(r_b, \Omega, \Omega_0) = \rho_{eff,\,\lambda}^q(r_b) \cdot S^q(r_b, \Omega) \cdot T_\lambda^q(\Omega_0) \tag{85}$$

Taking into account Eq. (85), we then can rewrite the solution of the transport problem, Eq. (79), as

$$L_\lambda(r, \Omega, \Omega_0) = L_{bs,\,\lambda}(r, \Omega, \Omega_0) + \rho_{eff,\,\lambda}^q(r_b) \cdot T_\lambda^q(\Omega_0) \cdot L_\lambda^q(r, \Omega) \tag{86}$$

where L_λ^q satisfies Eq. (54) with $F_\lambda = 0$, and with boundary conditions expressed by Eq. (69) and

$$L_\lambda^q(r_t, \Omega) = 0, \qquad\qquad r_t \in \delta V_t, \ \Omega \bullet n_t < 0$$

$$L_\lambda^q(r_b, \Omega) = S^q(r_b, \Omega), \qquad r_b \in \delta V_b, \ \Omega \bullet n_b < 0 \tag{87}$$

Thus, L_λ^q describes the radiative regime in the plant canopy generated by the anisotropic and heterogeneous source S^q located at the bottom of the canopy. We term the problem of finding L_λ^q an "S problem". Substituting Eq. (86) in Eq. (84) we get

$$
\begin{aligned}
T_\lambda^q(r_b, \Omega_0) &= \int\limits_{2\pi-} q(\Omega') \cdot L_{bs,\,\lambda}(r_b, \Omega', \Omega_0)|\mu'|d\Omega' \\
&\quad + \rho_{eff,\,\lambda}^q(r_b) \cdot T_\lambda^q(\Omega_0) \cdot \int\limits_{2\pi-} q(\Omega') \cdot L_\lambda^q(r_b, \Omega')|\mu'|d\Omega' \\
&= T_{bs,\,\lambda}^q(r_b, \Omega_0) + \rho_{eff,\,\lambda}^q(r_b) \cdot T_\lambda^q(\Omega_0) \cdot \mathbf{r}_\lambda^q(r_b)
\end{aligned}
\tag{88}
$$

where

$$T_{bs,\,\lambda}^q(r_b, \Omega_0) = \int\limits_{2\pi-} q(\Omega') \cdot L_{bs,\,\lambda}(r_b, \Omega', \Omega_0)|\mu'|d\Omega'$$

$$\mathbf{r}_\lambda^q(r_b) = \int\limits_{2\pi-} q(\Omega') \cdot L_\lambda^q(r_b, \Omega')|\mu'|d\Omega' \tag{89}$$

62

We then average Eq. (88) over the soil surface. This allows us to express T_λ^q via $T_{bs,\lambda}^q$, $\mathbf{r}_\lambda^q$, and $\rho_{eff,\lambda}^q$. Substituting the averaged T_λ^q into Eq. (86) we get

$$L_\lambda(r, \Omega, \Omega_0) \approx L_{bs,\lambda}(r, \Omega, \Omega_0) + \frac{\rho_{eff,\lambda}^q}{1 - \rho_{eff,\lambda}^q \mathbf{r}_\lambda^q} \cdot T_{bs,\lambda}^q(\Omega_0) L_\lambda^q(r, \Omega) \tag{90}$$

Here $T_{bs,\lambda}^q$, $\rho_{eff,\lambda}^q$ and $\mathbf{r}_\lambda^q$ are averages over the canopy bottom. Note that we can replace the approximate equality in Eq. (90) by exact equality if a one-dimensional canopy-radiation model is used to evaluate the radiative regime in plant canopy. It follows from Eq. (90) that the model BHR, $A_{model,\lambda}^{hem}$, the model HDRF, $r_{model,\lambda}$, and the fraction of incident direct and diffuse radiation absorbed by the vegetation, $\mathbf{a}_{model,\lambda}^{hem}$, at the wavelength λ can be expressed as

$$A_{model,\lambda}^{hem}(\Omega_0) \approx \mathbf{r}_{bs,\lambda}^{hem}(\Omega_0) + \mathbf{t}_\lambda^q \left(\frac{\rho_{eff,\lambda}^q}{1 - \rho_{eff,\lambda}^q \mathbf{r}_\lambda^q} \right) \mathbf{t}_{bs,\lambda}^{hem,q}(\Omega_0) \tag{91}$$

$$r_{model,\lambda}(\Omega, \Omega_0) \approx r_{bs,\lambda}(\Omega, \Omega_0) + \tau_\lambda^q(\Omega) \left(\frac{\pi \cdot \rho_{eff,\lambda}^q}{1 - \rho_{eff,\lambda}^q \mathbf{r}_\lambda^q} \right) \mathbf{t}_{bs,\lambda}^{hem,q}(\Omega_0) \tag{92}$$

$$\mathbf{a}_{model,\lambda}^{hem}(\Omega_0) \approx \mathbf{a}_{bs,\lambda}^{hem}(\Omega_0) + \mathbf{a}_\lambda^q(\Omega_0) \left(\frac{\rho_{eff,\lambda}^q}{1 - \rho_{eff,\lambda}^q \mathbf{r}_\lambda^q} \right) \mathbf{t}_{bs,\lambda}^{hem,q}(\Omega_0) \tag{93}$$

where $\mathbf{r}_{bs,\lambda}^{hem}$, $r_{bs,\lambda}$, and $\mathbf{a}_{bs,\lambda}^{hem}$ are the BHR, HDRF, and the fraction of radiation absorbed by the vegetation, respectively, when the soil reflectance is identically zero. Likewise, the model DHR, $A_{model,\lambda}^{dir}$, the model BRF, $R_{model,\lambda}$, and the fraction of direct incident radiation absorbed by the vegetation, $\mathbf{a}_{model,\lambda}^{dir}$, can be expressed as

$$A_{model,\lambda}^{dir}(\Omega_0) \approx \mathbf{r}_{bs,\lambda}^{dir}(\Omega_0) + \mathbf{t}_\lambda^q \left(\frac{\rho_{eff,\lambda}^q}{1 - \rho_{eff,\lambda}^q \mathbf{r}_\lambda^q} \right) \mathbf{t}_{bs,\lambda}^{dir,q}(\Omega_0), \tag{94}$$

$$R_{model,\lambda}(\Omega, \Omega_0) \approx R_{bs,\lambda}(\Omega, \Omega_0) + \tau_\lambda^q(\Omega) \left(\frac{\pi \cdot \rho_{eff,\lambda}^q}{1 - \rho_{eff,\lambda}^q \mathbf{r}_\lambda^q} \right) \mathbf{t}_{bs,\lambda}^{dir,q}(\Omega_0), \tag{95}$$

$$\mathbf{a}_{model,\lambda}^{dir}(\Omega_0) = \mathbf{a}_{bs,\lambda}^{dir}(\Omega_0) + \mathbf{a}_\lambda^q(\Omega_0) \left(\frac{\rho_{eff,\lambda}^q}{1 - \rho_{eff,\lambda}^q \mathbf{r}_\lambda^q} \right) \mathbf{t}_{bs,\lambda}^{dir,q}(\Omega_0). \tag{96}$$

Here

$$\mathbf{t}_{bs,\lambda}^{hem,q}(\Omega_0) = \frac{T_{bs,\lambda}^{q}(\Omega_0)}{\int\limits_{2\pi-} |\mu'| L_\lambda(r_t, \Omega', \Omega_0) d\Omega'} \tag{97}$$

$$\mathbf{t}_{bs,\lambda}^{dir,q}(\Omega_0) = \frac{T_{bs,\lambda}^{dir,q}(\Omega_0)}{\int\limits_{2\pi-} |\mu'| L_\lambda^{dir}(r_t, \Omega', \Omega_0) d\Omega'} \tag{98}$$

are the weighted canopy transmittances,

$$\mathbf{t}_\lambda^q = \int\limits_{2\pi+} |\mu'| L_\lambda^q(r_t, \Omega') d\Omega' \tag{99}$$

is the transmittance resulting from the anisotropic source S^q located at the canopy bottom,

$$\tau_\lambda^q(\Omega) = L_\lambda^q(r_t, \Omega) \tag{100}$$

is the radiance generated by S^q which leaves the top of the plant canopy, and $\mathbf{a}_\lambda^q$ is the radiance generated by S^q and absorbed by the vegetation. The radiation reflected, transmitted, and absorbed by the vegetation must be related via the energy conservation law:

$$\mathbf{r}_{bs,\lambda}^{hem}(\Omega_0) + k_\lambda^q(\Omega_0) \cdot \mathbf{t}_{bs,\lambda}^{hem,q}(\Omega_0) + \mathbf{a}_{bs,\lambda}^{hem}(\Omega_0) = 1, \qquad k_\lambda^q(\Omega_0) = \frac{\mathbf{t}_{bs,\lambda}^{hem,q\equiv 1}(\Omega_0)}{\mathbf{t}_{bs,\lambda}^{hem,q}(\Omega_0)}$$

$$\mathbf{r}_{bs,\lambda}^{dir}(\Omega_0) + k_\lambda^{dir,q}(\Omega_0) \cdot \mathbf{t}_{bs,\lambda}^{dir,q}(\Omega_0) + \mathbf{a}_{bs,\lambda}^{dir}(\Omega_0) = 1, \qquad k_\lambda^{dir,q}(\Omega_0) = \frac{\mathbf{t}_{bs,\lambda}^{dir,q\equiv 1}(\Omega_0)}{\mathbf{t}_{bs,\lambda}^{dir,q}(\Omega_0)}$$

$$\mathbf{r}_\lambda^q(\Omega_0) + \mathbf{t}_\lambda^q(\Omega_0) + \mathbf{a}_\lambda^q(\Omega_0) = 1 \tag{101}$$

Note that all variables in Eqs. (91)- (96) are mean values averaged over the top surface of the canopy.

It follows from Eq. (91) that

$$A_{model,\lambda}^{hem}(\Omega_0) - \mathbf{r}_{bs,\lambda}^{hem}(\Omega_0) \approx \mathbf{t}_\lambda^q(\Omega_0) \left(\frac{\rho_{eff,\lambda}^q}{1 - \rho_{eff,\lambda}^q \mathbf{r}_\lambda^q} \right) \mathbf{t}_{bs,\lambda}^{hem,q}(\Omega_0) \tag{102}$$

64

This equation shows that the contribution of the soil to the canopy-leaving radiance is proportional to the square of the canopy transmittance and the factor of proportionality depends on the effective soil reflectance. If the right side is sufficiently small, we can neglect this contribution by assigning the value zero to the effective soil reflection.

Thus, we have expressed the solution of the transport problem in terms of the effective soil reflectance and solutions of the "black-soil problem" and "S-problem." The solution of the "black-soil problem" depends on sun-view geometry, canopy architecture, and the spectral properties of the leaves. The "S problem" depends on the spectral properties of the leaves and canopy structure only. Our approach will be to focus on the solutions to these problems, using Eq. (90) as our basic algorithm equation. The next step is to specify the dependence of the basic algorithm equation on the wavelength.

6.5.3.5   Spectral variation of canopy absorptance, transmittance, and reflectance

The following results from eigenvector theory are required to derive a relationship between spectral leaf albedo and canopy absorptance, transmittance and reflectance.

An eigenvalue of the transport equation is a number γ such that there exists a function φ satisfying the equation

$$\gamma[\Omega \bullet \nabla\varphi(r, \Omega) + \sigma(r, \Omega)\varphi(r, \Omega)] \ = \ \int_{4\pi} \sigma_{s, \lambda}(r, \Omega' \to \Omega)\varphi(r, \Omega')d\Omega' \tag{103}$$

with boundary conditions

$$\varphi(r, \Omega) \ = \ 0, \qquad\qquad r \in \delta V, n_r \bullet \Omega < 0 \tag{104}$$

where n_r is the outward normal at a point $r \in \delta V$. The function φ is termed an eigenvector corresponding to the given eigenvalue γ.

The set of eigenvalues γ_k, $k = 0, 1, 2,...$, and eigenvectors φ_k, $k = 0, 1, 2,...$, of the transport equation is a discrete set *[78]*. The eigenvectors are mutually orthogonal, i.e.,

$$\int_V dr \int_{4\pi} \sigma(r, \Omega)\varphi_k(r, \Omega)\varphi_l(r, \Omega)d\Omega \ = \ \delta_{kl} \tag{105}$$

where δ_{kl} is the Kronecker symbol. The solution of the transport equation can be represented as a series in the eigenvectors of the transport equation. Coefficients of this series do not depend on either space or angular variables and they satisfy the boundary conditions of the radiative transfer

problem being studied.

The transport equation has a unique positive eigenvalue to which corresponds to a unique positive [normalized in the sense of Eq. (105)] eigenvector *[18]*. This eigenvalue is greater than the absolute magnitudes of the remaining eigenvalues. This means that only one eigenvector, say φ_0, takes on positive values for all $r \in V$ and Ω. This positive couple of eigenvector and eigenvalue plays an extremely important role in nuclear reactor theory. This positive eigenvalue alone determines if a reactor will work as a reactor, or as a bomb, or will simply not work. Its value successfully relates the reactor geometry to the absorption capacity of the active zone. Because the reactor is controlled by changing the absorption capacity of the active zone (by inserting or removing absorbents), this value is crucial to its functioning. There is a similar situation with our problem in that we need to relate canopy architecture ("similar" to reactor geometry) and leaf optical properties ("similar" to the absorption capacity of the active zone).

The expansion of the solution of the transport equation in eigenvectors has mainly theoretical value because the problem of finding these vectors is much more complicated than finding the solution of the transport equation. However, this approach is useful if we want to estimate some integrals of the solution. Therefore, we apply this technique to derive a relationship between spectral leaf albedo and canopy absorptance, transmittance, and reflectance.

It follows from Eqs. (69) and (87) that the boundary conditions of the "*S*-problem" do not depend on wavelength. Equation (63) allows us to reduce the "black soil" problem to one whose boundary conditions also do not depend on wavelength. This is achieved by dividing the transport equation and the boundary conditions which define the "black soil problem" by the irradiance (direct plus diffuse) incident on the top surface of the canopy boundary. Although the boundary conditions do not depend on wavelength, the solution to the transport equation is still wavelength dependent. Below, we use the variable φ to represent the normalized solution of the "black soil problem" and the solution of the "*S* problem." Because of Eq. (62), we can ignore the function F_λ when deriving radiation quantities which are integrated over spatial and angular variables. Expanding the solution φ in eigenvectors,

$$\varphi_\lambda(r, \Omega) = a_0(\lambda)\varphi_0(\lambda, r, \Omega) + \sum_{k=1}^{\infty} a_k(\lambda)\varphi_k(\lambda, r, \Omega), \qquad\qquad r \in V$$

(106)

where coefficients a_k do not depend on spatial or angular variables. Here, we separate the positive eigenvector φ_0 into the first summand. As described above, only this summand, $a_0\varphi_0$, takes on positive values for any $r \in V$ and Ω. Substituting Eq. (106) into the transport equation, Eq. (54), and differentiating with respect to the wavelength λ, we get

$$\sum_{k=0}^{\infty} \Omega \bullet \nabla u_k(\lambda, r, \Omega) + \sigma(r, \Omega) \sum_{k=0}^{\infty} u_k(\lambda, r, \Omega)$$

$$= \sum_{k=0}^{\infty} \frac{d}{d\lambda} \int_{4\pi} \sigma_{s,\lambda}(r, \Omega' \to \Omega) a_k(\lambda) \varphi_k(\lambda, r, \Omega') d\Omega' \tag{107}$$

where

$$u_k(\lambda, r, \Omega) = \frac{d}{d\lambda}[a_k(\lambda)\varphi_k(\lambda, r, \Omega)] \tag{108}$$

Because boundary conditions for the "black soil" and "S problem" do not depend on wavelength, we have

$$u_k(\lambda, r, \Omega) = 0 \qquad r \in \delta V, n_r \bullet \Omega < 0, \quad k = 0, 1, 2, \dots \tag{109}$$

Substituting Eq. (103) into Eq. (107), we get

$$\sum_{k=0}^{\infty} [\Omega \bullet \nabla + \sigma(r, \Omega)] \left\{ [1 - \gamma_k(\lambda)] u_k(\lambda, r, \Omega) - a_k(\lambda)\varphi_k(\lambda, r, \Omega) \frac{d}{d\lambda}\gamma_k(\lambda) \right\} = 0 \tag{110}$$

where γ_k is the eigenvalue corresponding to the eigenvector φ_k. It follows from this equation as well as from the orthogonality of the eigenvectors expressed in Eq. (105) and from the boundary conditions expressed in Eq. (109) that

$$\frac{d}{d\lambda}[a_k(\lambda)\varphi_k(\lambda, r, \Omega)] = \frac{\dfrac{d\gamma_k(\lambda)}{d\lambda} \cdot [a_k(\lambda)\varphi_k(\lambda, r, \Omega)]}{1 - \gamma_k(\lambda)} \tag{111}$$

Solving this ordinary differential equation we find

$$a_k(\lambda)\varphi_k(\lambda, r, \Omega) = \frac{1 - \gamma_k(\lambda_0)}{1 - \gamma_k(\lambda)} \cdot [a_k(\lambda_0)\varphi_k(\lambda_0, r, \Omega)] \tag{112}$$

Thus, if we know the nth summand of the expansion in Eq. (106) at a wavelength λ_0, we can easily find this summand for any other wavelength.

We introduce **e**, the monochromatic radiation at wavelength λ intercepted by the vegetation

canopy,

$$\mathbf{e}(\lambda) = \int_V dr \int_{4\pi} \sigma(r, \Omega)\varphi_\lambda(r, \Omega)d\Omega \tag{113}$$

and $\mathbf{e}_0$ as

$$\mathbf{e}_0(\lambda) = \int_V dr \int_{4\pi} \sigma(r, \Omega)\varphi_\lambda(r, \Omega)\varphi_0(\lambda, r, \Omega)d\Omega \tag{114}$$

Given $\mathbf{e}$, we can evaluate the fraction $\mathbf{a}$ of radiation absorbed by the vegetation at the wavelength λ as

$$\mathbf{a}(\lambda) = [1 - \varpi(\lambda)]\mathbf{e}(\lambda) \tag{115}$$

where ϖ is the leaf albedo. There is a technique which allows us to estimate $\mathbf{e}_0$, which is very close to $\mathbf{e}$, but we skip a precise mathematical proof of this fact here. An intuitive explanation is as follows. Putting Eq. (106) into Eq. (113) and performing an integration of the series, only the positive term containing $a_0\varphi_0$ "survives." As a result, we get

$$\frac{\mathbf{e}(\lambda)}{\mathbf{e}(\lambda_0)} = \frac{\mathbf{e}_0(\lambda)}{\mathbf{e}_0(\lambda_0)} \tag{116}$$

Let us derive the dependence of $\mathbf{e}_0$ on wavelength. Substituting Eq. (106) into Eq. (114) and taking into account Eq. (112) as well as the orthogonality of eigenvectors, Eq. (105), we get

$$\mathbf{e}_0(\lambda) = \frac{1 - \gamma_0(\lambda_0)}{1 - \gamma_0(\lambda)} \cdot \mathbf{e}_0(\lambda_0) \tag{117}$$

where γ_0 is the positive eigenvalue corresponding to the positive eigenvector φ_0. Taking into account Eq. (115), we can also derive the following estimation for $\mathbf{a}$,

$$\mathbf{a}(\lambda) = \frac{1 - \gamma_0(\lambda_0)}{1 - \gamma_0(\lambda)} \cdot \frac{1 - \varpi(\lambda)}{1 - \varpi(\lambda_0)} \cdot \mathbf{a}(\lambda_0) \tag{118}$$

Thus, given the canopy absorptance at the wavelength λ_0, we can evaluate this variable at any wavelength λ. At a fixed wavelength, $\mathbf{a}$ is a function of canopy structure and Sun position in the case of the "black soil problem", and only a function of canopy structure in the case of the "S problem." We store $\mathbf{a}$ at a fixed wavelength λ_0 in the CART file.

Similar arguments allow us to derive an expression for canopy transmittance,

$$\mathbf{t}\left(\lambda, \frac{r_{D,\lambda}}{\varpi(\lambda)}\right) = \frac{1 - \gamma_0(\lambda_0)}{1 - \gamma_0(\lambda)} \cdot \mathbf{t}\left(\lambda_0, \frac{r_{D,\lambda}}{\varpi(\lambda)}\right) \tag{119}$$

where $r_{D,\lambda}$ is the spectral reflectance of the leaf element. The ratio $r_{D,\lambda}/\varpi$ is assumed to be constant with respect to wavelength for each biome. Thus, given the canopy transmittance at the wavelength λ_0, we can evaluate this variable for any wavelength λ. At a fixed wavelength, $\mathbf{t}$ is a function of canopy structure and Sun position in the case of the "black soil problem", and a function only of canopy structure in the case of the "S problem." We store $\mathbf{t}$ at a fixed wavelength λ_0 in the CART file.

The canopy reflectance $\mathbf{r}$ is related to the absorptance and transmittance via the energy conservation law

$$\mathbf{r}(\lambda) = 1 - \mathbf{t}(\lambda) - \mathbf{a}(\lambda) \tag{120}$$

Thus, given canopy transmittance and absorptance at a fixed wavelength, we can obtain the canopy reflectance for any wavelength.

Recalling that we used the same notations for the "black soil problem" and the "S problem", $\mathbf{t}$ in Eq. (119) represents $\mathbf{t}_{bs,\lambda}^{hem,q}$ and $\mathbf{t}_{\lambda}^{q}$ for these two problems, respectively. Likewise for the canopy reflectance, where $\mathbf{r}$ represents $\mathbf{r}_{bs,\lambda}^{hem}$ and $\mathbf{r}_{\lambda}^{q}$, and for the canopy absorptance, where $\mathbf{a}$, represents $\mathbf{a}_{bs,\lambda}^{hem}$ and $\mathbf{a}_{\lambda}^{q}$ for the "black soil problem" and "S problem", respectively.

The unique positive eigenvalue γ_0, corresponding to the unique positive eigenvector, can be estimated as *[36]*

$$\gamma_0(\lambda) = \varpi(\lambda) \cdot [1 - e^{-K}] \tag{121}$$

where K is a coefficient which may depend on canopy structure (i.e., biome type, LAI, ground cover, etc.) and Sun position but not on wavelength or soil type. Its specification depends on the parameter (absorptance or transmittance) and type of transport problem ("black soil problem" or "S problem"). The coefficient K, however, does not depend on the transport problem and Sun position when it refers to canopy absorptance. We introduce coefficients $\mathbf{pt}_{bs}$, $\mathbf{pt}$ and $\mathbf{pa}$ which are equal to $[1 - e^{-K}]$ with the appropriate coefficients K for the transmittances of the "black soil problem" and the "S problem" and the canopy absorption. Note that the eigenvalue γ_0 depends on values of spectral leaf albedo which, in turn, depends on wavelength. It allows us to parameterize canopy absorption and transmittance in terms of canopy structure, Sun position and leaf albedo.

The coefficient **pa**, for a LAI equal to *lai,* is the value of p which minimizes the expression

$$\xi_{\mathbf{a}}(p, lai, \varpi^*) = \int_{0.01}^{0.9} \left[\frac{1 - \varpi^* \cdot p}{1 - \varpi \cdot p} \cdot \frac{1 - \varpi}{1 - \varpi^*} \mathbf{a}(lai, \varpi^*) - \mathbf{a}(lai, \varpi) \right]^2 d\varpi \tag{122}$$

Here **a** is the canopy absorptance which is a function of leaf albedo ϖ and leaf area index *lai* and is evaluated by solving the radiative transfer problem. ϖ^* is a reference leaf albedo which is specified below.

In a similar fashion, the coefficient $\mathbf{pt}_{bs}$ or **pt** is the value of p which minimizes the expression

$$\xi_{\mathbf{t}, x}(p, lai, \varpi^*) = \int_{0.01}^{0.9} \left[\frac{1 - \varpi^* \cdot p}{1 - \varpi \cdot p} \cdot \mathbf{t}_x(lai, \varpi^*) - \mathbf{t}_x(lai, \varpi) \right]^2 d\varpi$$

$$+ \int_{0.01}^{0.9} \left[1 - \frac{1 - \varpi^* \cdot p}{1 - \varpi \cdot p} \cdot \mathbf{t}_x(lai, \varpi^*) - \frac{1 - \varpi^* \cdot \mathbf{pa}(lai)}{1 - \varpi \cdot \mathbf{pa}(lai)} \cdot \frac{1 - \varpi^*}{1 - \varpi} \mathbf{a}(lai, \varpi^*) \right]^2 d\varpi \tag{123}$$

Here $\mathbf{t}_x$ is the canopy transmittance for the "black soil problem" ($x = bs$) or for the "S problem" ($x = S$) which is a function of leaf albedo ϖ and leaf area index *lai* and is evaluated by solving the radiative transfer problem. The values of p for which $\xi_{\mathbf{t}, bs}$ and $\xi_{\mathbf{t}, S}$ attain their minimum, $\mathbf{pt}_{bs}$ and **pt**, respectively, provide the best agreement to Eq. (119) and to the energy conservation law, Eq. (120).

As a reference leaf albedo, we find the value of ϖ^* which minimizes the expression

$$\xi(\varpi^*) = \int_{LAI_{min}}^{LAI_{max}} \xi_{\mathbf{a}}(\mathbf{pa}(lai), lai, \varpi^*) dlai$$

$$+ \int_{LAI_{min}}^{LAI_{max}} \xi_{\mathbf{t}, bs}(\mathbf{pt}_{bs}(lai), lai, \varpi^*) dlai$$

$$+ \int_{LAI_{min}}^{LAI_{max}} \xi_{\mathbf{t}, S}(\mathbf{pt}(lai), lai, \varpi^*) dlai \tag{124}$$

where LAI_{min} and LAI_{max} are specified in the CART file. A value of the reference leaf albedo for

biome1 and biome3 was found to be $\varpi^* = 0.1$.

Thus, we can express the BHR in terms of the optical properties of an individual leaf and the energy conservation law as well as in terms of solutions of the "black soil problem" and "S problem" at a leaf albedo value of ϖ^*. It allows us to compare spectral measurements of the BHR with spectral properties of individual leaves which is a rather stable characteristic of green leaves.

6.5.3.6 Conservativity as a tool to reduce number of retrieved solutions

As follows from Eqs. (91), (94) and (95), a very important procedure in the LAI/FPAR retrieval is to simulate the BHR, DHR, and BRF when the soil reflectance is identically zero. In spite of the diversity of canopy reflectance models, the direct use of these black soil models in an inversion algorithm is ineffective. In case of biomes 2 - 6, for example, the interaction of photons with the rough and rather thin surface of tree crowns and with the soil between crown openings are the most important factors causing the observed variation in the directional reflectance distribution of plant canopies. This property is characteristic of many canopy reflectance models. As a result, they are only slightly sensitive to the within-canopy radiative regime. Mathematically, this condition leads to the fact that a rather wide family of canopy radiation models can be a solution to Eq. (54), some of which can have a non-physical internal source F_λ. For such a model the radiation absorbed, transmitted, and reflected by the canopy may not be equal to the radiation incident on the canopy. The function F_λ can be chosen in such a way, however, that a model simulates the canopy reflectance correctly, i.e., such canopy radiation models account for photon interaction within a rather small domain of the vegetation canopy. On the other hand, just the within-canopy radiative regime is very sensitive to the canopy structure and, as a consequence, to LAI. The within-canopy radiative regime also determines the amount of solar energy absorbed by trees. Ignoring this fact in canopy radiation models leads to a large number of non-physical solutions when one inverts a canopy reflectance model. Therefore, Eq. (95) must be transformed before it can be used in a retrieval algorithm.

Let us introduce the weights

$$w_{bs,\lambda}^{dir}(\Omega, \Omega_0) = \frac{\pi^{-1}R_{bs,\lambda}(\Omega, \Omega_0)}{\mathbf{r}_{bs,\lambda}^{dir}(\Omega_0)}, \qquad \int_{2\pi+} w_{bs,\lambda}^{dir}(\Omega, \Omega_0)|\mu|\,d\Omega = 1 \tag{125}$$

$$w_\lambda^q(\Omega) = \frac{\tau_\lambda^q(\Omega)}{\mathbf{t}_\lambda^q}, \qquad \int_{2\pi+} w_\lambda^q(\Omega)|\mu|\,d\Omega = 1 \tag{126}$$

Taking into account these notations we can rewrite Eq. (95) as

71

$$R_{model, \lambda}(\Omega, \Omega_0) \approx \pi w_{bs, \lambda}^{dir}(\Omega, \Omega_0) \mathbf{r}_{bs, \lambda}^{dir}(\Omega_0) + \pi w_\lambda^q(\Omega) \mathbf{t}_\lambda^q \left(\frac{\rho_{eff, \lambda}^q}{1 - \rho_{eff, \lambda}^q \mathbf{r}_\lambda^q} \right) \mathbf{t}_{bs, \lambda}^{dir, q}(\Omega_0) \qquad (127)$$

Using Eq. (101), we then replace canopy reflectances $\mathbf{r}_{bs, \lambda}^{dir}$ and $\mathbf{r}_\lambda^q$ by

$$\mathbf{r}_{bs, \lambda}^{dir}(\Omega_0) = 1 - \mathbf{t}_{bs, \lambda}^{dir, q=1}(\Omega_0) - \mathbf{a}_{bs, \lambda}^{dir}(\Omega_0) = 1 \qquad (128)$$

$$\mathbf{r}_\lambda^q = 1 - \mathbf{t}_\lambda^q - \mathbf{a}_\lambda^q \qquad (129)$$

As a result of this transformation we have that Eq. (127) is sensitive both to factors determining the directional reflectance distribution of plant canopies (the weight $w_{bs, \lambda}^{dir}$) and to the within-canopy radiative regime ($\mathbf{t}_{bs, \lambda}^{dir, q=1}$, $\mathbf{a}_{bs, \lambda}^{dir}$, $\mathbf{t}_\lambda^q$, $\mathbf{a}_\lambda^q$). Equations (127) - (129) also allow us to formulate a test for the "eligibility" of a canopy radiation model to generate the CART file as follows. We evaluate the weight $w_{bs, \lambda}^{dir}$ as a function of sun-view geometry, wavelength, and LAI by using a tested canopy reflectance model. Then, using the same canopy radiation model we evaluate $\mathbf{r}_{bs, \lambda}^{dir}$ from Eq. (128) and put it into Eq. (125). A canopy radiation model is "eligible" to generate the CART file if Eq. (125) is fulfilled within a given accuracy for any sun-view combination, wavelength, and LAI. The satisfying of the condition expressed by Eq. (62) is sufficient to pass this test. However, it is not a necessary condition to provide the correct proportion between canopy absorptance, transmittance, and reflectance.

We are currently not familiar with a canopy reflectance model which can pass the above test. Therefore, we have to correct canopy radiation models for "eligibility" to be used within our approach. The algorithm expressed by Eqs. (122) - (124) satisfies this objective. Indeed, this algorithm needs a reference leaf albedo and the functions $\mathbf{pa}$, $\mathbf{pt}_{bs}$ ($= \mathbf{pt}_{bs}^{dir} + \mathbf{pt}_{bs}^{diff}$) and $\mathbf{pt}$ which provide the best agreement to the energy conservation law for any value of sun position, wavelength, and LAI. A canopy radiation model is recognize to be "eligible" if $\xi(\varpi)$ defined by Eq. (124) is less than 0.001 (we have reached this value by using our model). Note that there is no conflict with the energy conservation law in the case of the *S*-problem.

6.5.3.7 Saturation domains

Given the retrieved spectral BHR's (or DHR's) and the spectral BRF's (or HDRF's), it may be the case that the LAI algorithm admits a number of solutions, covering a wide range of LAI values, for a given biome type. When this happens, the retrieved reflectances and reflectance factors are said to belong to the saturation domain, being insensitive to the various parameter values of the canopy radiation model. Under this condition, the histograms which describe the number of times a solution has a particular LAI value will appear flat over the range of LAI, illustrating that the solutions all have equal probability of occurrence.

If the solutions are described by a normalized cumulative distribution function Φ,

$$\Phi(L^*, L) = \frac{\Psi(L^*, L)}{\Psi(L^*, L_{max})} \tag{130}$$

where Ψ is the number of solutions having LAI values between L^* and L, then $d\Phi$ represents the solution histogram. Here, L^* is the smallest LAI value (saturation point) at which saturation occurs. Thus, Ψ can be written as

$$\Psi(L^*, L) = 0, \qquad L < L^*$$

$$\Psi(L^*, L) = \int_{L^* \le LAI < L} dH_{LAI}(LAI), \qquad L^* \le L < L_{max}$$

$$= \int_{max\{L^*, LAI_{min}\}}^{min\{L, LAI_{max}\}} dH_{LAI}(LAI)$$

$$\Psi(L^*, L) = \Psi(L^*, L_{max}), \qquad L \ge L_{max}$$

$$= \int_{max\{L^*, LAI_{min}\}}^{LAI_{max}} dH_{LAI}(LAI) \tag{131}$$

with

$$H_{LAI}(LAI) = 0, \qquad LAI < LAI_{min}$$

$$= LAI, \quad LAI_{min} \le LAI < LAI_{max}$$

$$= L_{max}, \quad L \ge L_{max} \tag{132}$$

Under the condition of saturation, the LAI solution from the first comparison test (using retrieved BHR A_λ^{hem} and $A_{model, \lambda}^{hem}$, or retrieved DHR A_λ^{dir} and $A_{model, \lambda}^{dir}$) is formulated as,

$$\overline{LAI}_A(L_A^*) = \int_{L_{min}}^{L_{max}} L \cdot \left[\frac{d\Phi(L_A^*, L)}{dL} \right] dL \tag{133}$$

with a variance,

$$d_A(L_A^*) = \int\limits_{LAI_{min}}^{LAI_{max}} [L - \overline{LAI}_A(L_A^*)]^2 \cdot \left[\frac{d\Phi(L_A^*, L)}{dL}\right] dL \qquad (134)$$

Analogous expressions hold for the LAI solution from the second comparison test (using BRF, R_λ).

These expressions allow us to test if the retrieved reflectances belong to the saturation domain through the formulation of a necessary condition, derived as follows. We note that both the mean LAI and the variance, as defined by Eqs. (133) and (134), are determined from model canopy characteristics only and are independent of any retrieved or measured quantities. Therefore, $d\Phi/dL$ can be precomputed for each biome type and the following equation solved for L^*,

$$\overline{LAI}(L^*) = \int\limits_{L_{min}}^{L_{max}} L \cdot \left[\frac{d\Phi(L^*, L)}{dL}\right] dL, \qquad L_{min} \le \overline{LAI} \le L_{max} \qquad (135)$$

resulting in a function $L^*(\overline{LAI})$. The variance d^* associated with $\overline{LAI}$ then can be calculated from

$$d^*(\overline{LAI}) = \sqrt{\int\limits_{L_{min}}^{L_{max}} [L - \overline{LAI}]^2 \cdot \left[\frac{d\Phi(L^*(\overline{LAI}), L)}{dL}\right] dL} \qquad (136)$$

Now, if the retrieved reflectances belong to the saturation domain, then the solution from the first comparison test, $\overline{LAI}_1$ and its spread ΔLAI_1, and the solution from the second comparison test, $\overline{LAI}_2$ and its spread ΔLAI_2, must satisfy the conditions,

$$\begin{aligned}
\overline{LAI}_1 &= L^*(\overline{LAI}_1) \\
\overline{LAI}_2 &= L^*(\overline{LAI}_2) \\
\Delta LAI_1 &= d^*(\overline{LAI}_1) \\
\Delta LAI_2 &= d^*(\overline{LAI}_2)
\end{aligned} \qquad (137)$$

to within a configured accuracy. If these conditions are met, this implies that the reflectances belong to the saturated domain and that any value of LAI from $2\overline{LAI} - L_{max}$ to L_{max} must be considered a true solution with equal probability.

To facilitate the testing of these conditions, L^* and d^* vs. $\overline{LAI}$ are precomputed and stored in the CART file. For biome types 1 (grasses/cereal crops) and 3 (broadleaf crops) the evaluation

of L^* and d^* are particularly simple. It follows from Eqs. (130) - (131) that the solution distribution function for the saturation domain of these two biome types is

$$
\begin{aligned}
\Phi(L^*, L) &= 0, & L &< L^* \\
\Phi(L^*, L) &= \frac{L - L^*}{L_{max} - L^*}, & L^* &\leq L < L_{max} \\
\Phi(L^*, L) &= 1, & L &\geq L_{max}
\end{aligned}
\tag{138}
$$

Thus, from Eqs. (135) and (136)

$$
\begin{aligned}
L^* &= 2\overline{LAI} - L_{max} = L^*(\overline{LAI}) \\
d^* &= \frac{1}{\sqrt{3}}(L_{max} - \overline{LAI}) = d(\overline{LAI})
\end{aligned}
\tag{139}
$$

6.5.3.8 Canopy absorption and retrieved BRF uncertainty

How accurately canopy absorptance $\mathbf{a}_\lambda^{hem}$ can be determined, given the uncertainty ΔA_λ^{hem} in the retrieved BRF A_λ^{hem}, impacts the determination of FPAR which is defined as the fraction of photosynthetically active radiation absorbed by green elements of the vegetation canopy. We can write FPAR as

$$
FPAR(\Omega_0) = \frac{\displaystyle\int_{400}^{700} \mathbf{a}_\lambda^{hem}(\Omega_0) e_\lambda^{hem}(\Omega_0) E_{0,\lambda} d\lambda}{\displaystyle\int_{400}^{700} e_\lambda^{hem}(\Omega_0) E_{0,\lambda} d\lambda},
\tag{140}
$$

where $E_{0,\lambda}$ is the TOA solar irradiance spectrum and e_λ^{hem} is the normalized irradiance incident on the canopy. The model canopy absorptance, $\mathbf{a}_{model,\lambda}^{hem}$, can be expressed as

$$
\mathbf{a}_{model,\lambda}^{hem}(\Omega_0) = \mathbf{a}_{bs,\lambda}^{hem}(\Omega_0) + \frac{\mathbf{a}_\lambda^q}{\mathbf{t}_\lambda^q}[A_{model,\lambda}^{hem}(\Omega_0) - r_{bs,\lambda}^{hem}(\Omega_0)],
\tag{141}
$$

upon substituting Eq. (91) into (93) If we replace the model BRF, $A_{model,\lambda}^{hem}$, by the retrieved value, A_λ^{hem}, then Eq. (141) becomes an expression for $\mathbf{a}^{hem}$ as used in Eq. (140). However, the non-negativity of Eq. (141) can be violated when this replacement occurs, due to the uncertainty in the value of A_λ^{hem}. Therefore, we start our analysis by an examination of when A_λ^{hem} - $\mathbf{r}_{bs,\lambda}^{hem}$ takes on

75

negative values.

As described in *[M-12]*, determination of biome type and LAI requires that the candidate biome/canopy/soil model pass two merit tests, the first of which is a comparison of the retrieved BRF and the model BRF. This comparison can be described by testing whether

$$\left| A_\lambda^{hem}(\Omega_0) - A_{model, \lambda}^{hem}(\Omega_0) \right| \le \delta_\lambda(\Omega_0) \,, \tag{142}$$

where $\delta_\lambda = \Delta A_\lambda^{hem} \cdot \Delta_{1, thresh}$ and $\Delta_{1, thresh}$ is a configurable threshhold parameter. Using Eq. (91), this inequality can be rewritten as

$$
\mathbf{t}_\lambda^q \frac{\rho_{eff, \lambda}^q}{1 - \rho_{eff, \lambda}^q \mathbf{r}_\lambda^q} \cdot \mathbf{t}_{bs, \lambda}^{hem, q}(\Omega_0) - \delta_\lambda(\Omega_0)
$$
$$
\le A_\lambda^{hem}\Omega_0 - \mathbf{r}_{bs, \lambda}^{hem}(\Omega_0) \le
$$
$$
\mathbf{t}_\lambda^q \frac{\rho_{eff, \lambda}^q}{1 - \rho_{eff, \lambda}^q \mathbf{r}_\lambda^q} \cdot \mathbf{t}_{bs, \lambda}^{hem, q}(\Omega_0) + \delta_\lambda(\Omega_0) \tag{143}
$$

It follows from Eq. (143) that the difference A_λ^{hem} - $\mathbf{r}_{bs, \lambda}^{hem}$ can take on negative values only if the left side of the inequality is negative, i.e.,

$$\mathbf{t}_\lambda^q \frac{\rho_{eff, \lambda}^q}{1 - \rho_{eff, \lambda}^q \mathbf{r}_\lambda^q} \cdot \mathbf{t}_{bs, \lambda}^{hem, q}(\Omega_0) \le \delta_\lambda(\Omega_0) \,. \tag{144}$$

This means that the contribution of the ground (soil and/or understory) to the canopy-leaving radiation is comparable to the uncertainty in the retrieved BHR so that there is no reliable information to estimate the Q_2 term.

There is another problem encountered when one uses Eq. (141) to evaluate the canopy absorptance. The factor $1/\mathbf{t}^q$ may become arbitrarily large as LAI takes on large values. Although $(A_{model, \lambda}^{hem} - \mathbf{r}_{bs, \lambda}^{hem})/\mathbf{t}_\lambda^q$ theoretically tends to zero in these cases, Eq. (141), containing the retrieved A_λ^{hem} instead of the modeled BHR, will tend to infinity as LAI increases, namely,

$$\lim_{LAI \to \infty} \frac{A_\lambda^{hem}(\Omega_0) - \mathbf{r}_{bs,\lambda}^{hem}(\Omega_0)}{\mathbf{t}_\lambda^q} = \lim_{LAI \to \infty} \frac{[A_{model,\lambda}^{hem}(\Omega_0) + \delta_\lambda(\Omega_0)] - \mathbf{r}_{bs,\lambda}^{hem}(\Omega_0)}{\mathbf{t}_\lambda^q}$$

$$= \lim_{LAI \to \infty} \frac{\delta_\lambda(\Omega_0)}{\mathbf{t}_\lambda^q} = \infty$$

(145)

Thus, small variations in can cause numerical instabilities in the FPAR retrieval technique. Therefore, evaluation of FPAR for sufficiently dense canopies requires special attention if these instabilities are to be avoided.

We note from Eqs. (101) and (141) that the canopy absorptance can be written as

$$\mathbf{a}_{model,\lambda}^{hem}(\Omega_0) = 1 - A_{model,\lambda}^{hem}(\Omega_0) - \left\{ \mathbf{t}_{bs,\lambda}^{hem, q \equiv 1}(\Omega_0) \right.$$

$$\left. - \frac{\mathbf{t}_\lambda^q + \mathbf{a}_\lambda^q}{\mathbf{t}_\lambda^q}[A_{model,\lambda}^{hem}(\Omega_0) - \mathbf{r}_{bs,\lambda}^{hem}(\Omega_0)] \right\}$$

.
(146)

The expression in the braces describes the fraction of radiation absorbed by the ground (soil and/or understory). It takes on non-negative values when

$$A_{model,\lambda}^{hem}(\Omega_0) - \mathbf{r}_{bs,\lambda}^{hem}(\Omega_0) \le \frac{\mathbf{t}_{bs,\lambda}^{hem, q \equiv 1}(\Omega_0)\mathbf{t}_\lambda^q}{\mathbf{t}_\lambda^q + \mathbf{a}_\lambda^q}.$$

(147)

Because

$$\lim_{LAI \to \infty} \left\{ A_{model,\lambda}^{hem}(\Omega_0) - \mathbf{r}_{bs,\lambda}^{hem}(\Omega_0) - \frac{\mathbf{t}_{bs,\lambda}^{hem, q \equiv 1}(\Omega_0)\mathbf{t}_\lambda^q}{\mathbf{t}_\lambda^q + \mathbf{a}_\lambda^q} \right\} = 0$$

,
(148)

the inequality expressed by (147) can be violated due to the retrieval uncertainty when $A_{model,\lambda}^{hem}$ is replaced by A_λ^{hem}. This occurs when LAI is sufficiently large. It follows from Eq. (141) and expression (147) that

$$\mathbf{a}_{model,\lambda}^{hem}(\Omega_0) \le \mathbf{a}_{bs,\lambda}^{hem}(\Omega_0) + \frac{\mathbf{a}_\lambda^q}{\mathbf{t}_\lambda^q} \cdot \frac{\mathbf{t}_{bs,\lambda}^{hem, q \equiv 1}(\Omega_0)\mathbf{t}_\lambda^q}{\mathbf{t}_\lambda^q + \mathbf{a}_\lambda^q}$$

$$\le \mathbf{a}_{bs,\lambda}^{hem}(\Omega_0) + \mathbf{t}_{bs,\lambda}^{hem, q \equiv 1}(\Omega_0)$$

.
(149)

Thus,

$$\lim_{LAI \to \infty} \mathbf{a}^{hem}_{model, \lambda}(\Omega_0) = \mathbf{a}^{hem}_{bs, \lambda}(\Omega_0)$$

(150)

proving that the fraction of radiation absorbed by the ground becomes negligible for sufficiently large LAI. Thus, the violation of expression (147) due to the retrieval uncertainty indicates that the contribution of the ground to the canopy absorptance does not exceed the uncertainty in A^{hem}_{λ} and does not provide any reliable information to estimate the Q_2 term. We set $\mathbf{a}^{hem}_{model, \lambda} = \mathbf{a}^{hem}_{bs, \lambda}$ in this case.

It follows from the above discussion that the following formula can approximate $\mathbf{a}^{hem}_{\lambda}$, the estimate of the canopy absorptance using A^{hem}_{λ}, as accurately as A^{hem}_{λ} is retrieved:

$$\mathbf{a}^{hem}_{\lambda}(\Omega_0) = \mathbf{a}^{hem}_{bs, \lambda}(\Omega_0) + \frac{\mathbf{a}^q_{\lambda}}{\mathbf{t}^q_{\lambda}}[A^{hem}_{\lambda}(\Omega_0) - \mathbf{r}^{hem}_{bs, \lambda}(\Omega_0)]$$

$$\text{if } 0 < A^{hem}_{\lambda}(\Omega_0) - \mathbf{r}^{hem}_{bs, \lambda}(\Omega_0) < \frac{\mathbf{t}^{hem, q \equiv 1}_{bs, \lambda}(\Omega_0)\mathbf{t}^q_{\lambda}}{\mathbf{t}^q_{\lambda} + \mathbf{a}^q_{\lambda}}$$

$$\mathbf{a}^{hem}_{\lambda}(\Omega_0) = 1 - A^{hem}_{\lambda}(\Omega_0) \qquad \text{otherwise.}$$

(151)

Note that if we set $\mathbf{a}^{hem}_{\lambda} = \mathbf{a}^{hem}_{bs, \lambda}$ when expression (147) is violated, we get

$$\mathbf{a}^{hem}_{\lambda}(\Omega_0) = \mathbf{a}^{hem}_{bs, \lambda}(\Omega_0) \leq \mathbf{a}^{hem}_{bs, \lambda}(\Omega_0) + \frac{\mathbf{a}^q_{\lambda}}{\mathbf{t}^q_{\lambda}}[A^{hem}_{model, \lambda}(\Omega_0) - \mathbf{r}^{hem}_{bs, \lambda}(\Omega_0)]$$

$$= \mathbf{a}^{hem}_{model, \lambda}(\Omega_0)$$

(152)

It follows from Eq. (146) that $\mathbf{a}^{hem}_{model, \lambda} \leq 1 - A^{hem}_{model, \lambda}$ and, as a consequence, $\mathbf{a}^{hem}_{\lambda} \leq 1 - A^{hem}_{model, \lambda}$. This means that the uncertainty in $\mathbf{a}^{hem}_{\lambda}$ is comparable to the uncertainty in A^{hem}_{λ} for large LAI.

6.5.3.9 Compatibility of retrieved PAR-integrated BHR and FPAR

The proposed FPAR retrieval algorithm, described by Eq. (151), provides good agreement between two MISR products, the PAR -integrated BHR, A^{hem}_{PAR}, and FPAR. To show this, the following theorem is proved first:

Theorem: $\mathbf{a}^{hem}_{\lambda} \leq 1 - A^{hem}_{\lambda}$

Proof: Let $\varepsilon_{\lambda} = A^{hem}_{\lambda} - A^{hem}_{model, \lambda}$. Consider the situation when the inequality described by

expression (147) takes place. Then, starting with Eq. (141), the description of canopy absorptance, and using Eq. (146) and expression (147),

$$
\begin{aligned}
\mathbf{a}_\lambda^{hem}(\Omega_0) &= \mathbf{a}_{bs,\lambda}^{hem}(\Omega_0) + \frac{\mathbf{a}_\lambda^q}{\mathbf{t}_\lambda^q}[A_{model,\lambda}^{hem}(\Omega_0) + \varepsilon_\lambda - \mathbf{r}_{bs,\lambda}^{hem}(\Omega_0)] \\
&= \mathbf{a}_{model,\lambda}^{hem}(\Omega_0) + \frac{\mathbf{a}_\lambda^q}{\mathbf{t}_\lambda^q} \cdot \varepsilon_\lambda \\
&= 1 - A_\lambda^{hem}(\Omega_0) - \left\{ \mathbf{t}_{bs,\lambda}^{hem,\, q \equiv 1}(\Omega_0) - \frac{\mathbf{t}_\lambda^q + \mathbf{a}_\lambda^q}{\mathbf{t}_\lambda^q}[A_\lambda^{hem}(\Omega_0) - \mathbf{r}_{bs,\lambda}^{hem}(\Omega_0)] \right\} \\
&\quad + \varepsilon_\lambda - \frac{\mathbf{t}_\lambda^q + \mathbf{a}_\lambda^q}{\mathbf{t}_\lambda^q} \cdot \varepsilon_\lambda + \frac{\mathbf{a}_\lambda^q}{\mathbf{t}_\lambda^q} \cdot \varepsilon_\lambda
\end{aligned} \qquad . \quad (153)
$$

Since the term in braces must be non-negative [see Eq. (151)],

$$
\begin{aligned}
\mathbf{a}_\lambda^{hem}(\Omega_0) &= 1 - A_\lambda^{hem}(\Omega_0) - \left\{ \mathbf{t}_{bs,\lambda}^{hem,\, q \equiv 1}(\Omega_0) - \frac{\mathbf{t}_\lambda^q + \mathbf{a}_\lambda^q}{\mathbf{t}_\lambda^q}[A_\lambda^{hem}(\Omega_0) - \mathbf{r}_{bs,\lambda}^{hem}(\Omega_0)] \right\} \\
&\leq 1 - A_\lambda^{hem}(\Omega_0) \qquad \qquad \mathbf{QED}
\end{aligned} \qquad (154)
$$

Then, using Eq. (140),

$$
\begin{aligned}
FPAR(\Omega_0) &= \frac{\displaystyle\int_{400}^{700} \mathbf{a}_\lambda^{hem}(\Omega_0) e_\lambda^{hem}(\Omega_0) E_{0,\lambda} d\lambda}{\displaystyle\int_{400}^{700} e_\lambda^{hem}(\Omega_0) E_{0,\lambda} d\lambda} \\
&\leq 1 - \frac{\displaystyle\int_{400}^{700} A_\lambda^{hem}(\Omega_0) e_\lambda^{hem}(\Omega_0) E_{0,\lambda} d\lambda}{\displaystyle\int_{400}^{700} e_\lambda^{hem}(\Omega_0) E_{0,\lambda} d\lambda} = 1 - A_{PAR}^{hem}(\Omega_0)
\end{aligned} \qquad (155)
$$

Thus, the absorption within the canopy/soil system, described by $1 - A_{PAR}^{hem}$, can never be less than the absorption, *FPAR*, within the canopy only. This must always be true and the determination of FPAR using the algorithm described by Eq. (151) will guarantee it.

6.5.3.10 Generation of algorithm parameters in the CART file.

During standard processing to obtain biome type and LAI, the model hemispherical reflectances, A_λ^{hem} and A_λ^{dir}, expressed by Eqs. (91) and (94) respectively, are needed in the first comparison test of the LAI algorithm. This test evaluates possible solutions by comparing these model reflectances to the retrieved spectral hemispherically integrated reflectances (DHR and BHR). Since a large number of canopy/soil models are tested this requires that $A_{model,\lambda}^{hem}$ and $A_{model,\lambda}^{dir}$ be determined as efficiently as possible. Now, $A_{model,\lambda}^{hem}$ can be written as

$$A_{model,\lambda}^{hem}(\Omega_0) = f_\lambda^{dir}(\Omega_0) \cdot A_{model,\lambda}^{dir}(\Omega_0) + [1 - f_\lambda^{dir}(\Omega_0)] \cdot A_{model,\lambda}^{diff}(\Omega_0) \qquad (156)$$

where $A_{model,\lambda}^{diff}$ is defined analogously to $A_{model,\lambda}^{dir}$ in Eq. (94),

$$A_{model,\lambda}^{diff}(\Omega_0) \approx \mathbf{r}_{bs,\lambda}^{diff}(\Omega_0) + \mathbf{t}_\lambda^q \left(\frac{\rho_{eff,\lambda}^q}{1 - \rho_{eff,\lambda}^q \mathbf{r}_\lambda^q} \right) \mathbf{t}_{bs,\lambda}^{diff,\,q}(\Omega_0) \qquad (157)$$

and with

$$\mathbf{r}_{bs,\lambda}^{diff}(\Omega_0) = 1 - \mathbf{t}_{bs,\lambda}^{diff,\,q=1}(\Omega_0) - \mathbf{a}_{bs,\lambda}^{diff}(\Omega_0), \qquad (158)$$

defined analogously to $\mathbf{r}_{bs,\lambda}^{dir}$ in Eq. (128). The parameter f_λ^{dir} in Eq. (156) is the ratio of the direct irradiance on the canopy to the total radiance and is determined in the retrieval process for DHR and BHR. Thus, to minimize computation time, $A_{model,\lambda}^{dir}$ and $A_{model,\lambda}^{diff}$ are precomputed and stored directly in the CART file and $A_{model,\lambda}^{hem}$ is then computed using Eq. (156). For each biome type, only those models with values of LAI which pass this hemispherical reflectance comparison test can then proceed to the second test which is a comparison of the retrieved spectral BRF to the model spectral BRF. It follows from Eqs. (94) and (127) that the model BRF can be represented as

$$R_{model,\lambda}(\Omega, \Omega_0) \approx \pi w_{bs,\lambda}^{dir}(\Omega, \Omega_0) \mathbf{r}_{bs,\lambda}^{dir}(\Omega_0) + \pi w_\lambda^q(\Omega)[A_\lambda^{dir}(\Omega_0) - \mathbf{r}_{bs,\lambda}^{dir}(\Omega_0)] \qquad (159)$$

Because we use the retrieved DHR as A_λ^{dir}, this expression for $R_{model,\lambda}$ does not explicitly depend on soil reflectance. Again, for computational efficiency Eq. (159) can be rewritten as

$$R_{model,\lambda}(\Omega, \Omega_0) = W_1(\Omega, \Omega_0) + W_2(\Omega) \cdot A_\lambda^{dir}(\Omega_0) \qquad (160)$$

where

$$W_1(\Omega, \Omega_0) = \pi \cdot [w_{bs,\lambda}^{dir}(\Omega, \Omega_0) - w_\lambda^q(\Omega)] \cdot \mathbf{r}_{bs,\lambda}^{dir}(\Omega_0) \tag{161}$$

$$W_2(\Omega) = \pi \cdot w_\lambda^q(\Omega) \tag{162}$$

Like $A_{model,\lambda}^{dir}$ and $A_{model,\lambda}^{diff}$ the parameters W_1 and W_2 are also precomputed and stored in the CART file.

The calculation of FPAR requires the determination of the fraction of direct and diffuse incident radiation absorbed by the vegetation, $\mathbf{a}_\lambda^{hem}$. From Eq. (141), $\mathbf{a}_\lambda^{hem}$ is given by

$$\mathbf{a}_\lambda^{hem}(\Omega_0) = \mathbf{a}_{bs,\lambda}^{hem}(\Omega_0) + \frac{\mathbf{a}_\lambda^q}{\mathbf{t}_\lambda^q}[A_\lambda^{hem}(\Omega_0) - \mathbf{r}_{bs,\lambda}^{hem}(\Omega_0)] \tag{163}$$

where the model BRF, $A_{model,\lambda}^{hem}$, is replaced by the retrieved BRF, A_λ^{hem}. With

$$\mathbf{a}_{bs,\lambda}^{hem}(\Omega_0) = f_\lambda^{dir}(\Omega_0) \cdot \mathbf{a}_{bs,\lambda}^{dir}(\Omega_0) + [1 - f_\lambda^{dir}(\Omega_0)] \cdot \mathbf{a}_{bs,\lambda}^{diff}(\Omega_0), \tag{164}$$

$$\mathbf{r}_{bs,\lambda}^{hem}(\Omega_0) = f_\lambda^{dir}(\Omega_0) \cdot \mathbf{r}_{bs,\lambda}^{dir}(\Omega_0) + [1 - f_\lambda^{dir}(\Omega_0)] \cdot \mathbf{r}_{bs,\lambda}^{diff}(\Omega_0) \tag{165}$$

and $\mathbf{r}_{bs,\lambda}^{dir}$ and $\mathbf{r}_{bs,\lambda}^{diff}$ defined by Eqs. (128) and (158), respectively, $\mathbf{a}_\lambda^{hem}$ in Eq. (163) can be recast as

$$\mathbf{a}_\lambda^{hem}(\Omega_0) = f_\lambda^{dir}(\Omega_0) \cdot F_{1,\lambda}^{dir}(\Omega_0) + [1 - f_\lambda^{dir}(\Omega_0)] \cdot F_{1,\lambda}^{diff}(\Omega_0) + F_{2,\lambda} \cdot A_\lambda^{hem}(\Omega_0) \tag{166}$$

with

$$F_{1,\lambda}^{dir}(\Omega_0) = \mathbf{a}_{bs,\lambda}^{dir}(\Omega_0) - \frac{\mathbf{a}_\lambda^q}{\mathbf{t}_\lambda^q} \cdot [1 - \mathbf{t}_{bs,\lambda}^{dir,\,q=1}(\Omega_0) - \mathbf{a}_{bs,\lambda}^{dir}(\Omega_0)], \tag{167}$$

$$F_{1,\lambda}^{diff}(\Omega_0) = \mathbf{a}_{bs,\lambda}^{diff}(\Omega_0) - \frac{\mathbf{a}_\lambda^q}{\mathbf{t}_\lambda^q} \cdot [1 - \mathbf{t}_{bs,\lambda}^{diff,\,q=1}(\Omega_0) - \mathbf{a}_{bs,\lambda}^{diff}(\Omega_0)], \tag{168}$$

and

$$F_{2,\lambda} = \frac{\mathbf{a}_\lambda^q}{\mathbf{t}_\lambda^q}. \tag{169}$$

A non-negativity test must also be performed, as described in Eq. (151),

$$0 < A_\lambda^{hem}(\Omega_0) - \mathbf{r}_{bs,\lambda}^{hem}(\Omega_0) < \frac{\mathbf{t}_{bs,\lambda}^{hem,q=1}(\Omega_0) \cdot \mathbf{t}_\lambda^q}{\mathbf{t}_\lambda^q + \mathbf{a}_\lambda^q}, \tag{170}$$

which can be rewritten as

$$0 < A_\lambda^{hem}(\Omega_0) - \mathbf{r}_{bs,\lambda}^{hem}(\Omega_0) < f_\lambda^{dir}(\Omega_0) \cdot T_\lambda^{dir}(\Omega_0) + [1 - f_\lambda^{dir}(\Omega_0)] \cdot T_\lambda^{diff}(\Omega_0). \tag{171}$$

Here, $\mathbf{r}_{bs,\lambda}^{hem}$ is given by Eq. (165) and T_λ^{dir} and T_λ^{diff} are

$$T_\lambda^{dir}(\Omega_0) = \frac{\mathbf{t}_{bs,\lambda}^{dir,q=1}(\Omega_0) \cdot \mathbf{t}_\lambda^q}{\mathbf{t}_\lambda^q + \mathbf{a}_\lambda^q}, \tag{172}$$

$$T_\lambda^{diff}(\Omega_0) = \frac{\mathbf{t}_{bs,\lambda}^{diff,q=1}(\Omega_0) \cdot \mathbf{t}_\lambda^q}{\mathbf{t}_\lambda^q + \mathbf{a}_\lambda^q}. \tag{173}$$

Thus, seven parameters, $\mathbf{r}_{bs,\lambda}^{dir}$, $\mathbf{r}_{bs,\lambda}^{diff}$, T_λ^{dir}, T_λ^{diff}, $F_{1,\lambda}^{dir}$, $F_{1,\lambda}^{diff}$, and $F_{2,\lambda}$, are used by the FPAR algorithm and these are precomputed and stored in the CART file to maximize algorithm efficiency.

To compute $A_{model,\lambda}^{dir}$, $A_{model,\lambda}^{diff}$ and all the other algorithm parameters for the CART file, it is necessary that $\mathbf{t}_{bs,\lambda}^{dir,q}$, $\mathbf{a}_{bs,\lambda}^{dir}$, $\mathbf{t}_{bs,\lambda}^{diff,q}$, $\mathbf{a}_{bs,\lambda}^{diff}$, $\mathbf{t}_\lambda^q$, and $\mathbf{a}_\lambda^q$, the variables upon which the algorithm parameters are dependent, be evaluated at the MISR wavelengths. This is done by using the following expressions, based on §6.5.3.5, which describe the spectral dependence of these parameters,

$$\mathbf{t}_{bs,\lambda}^{dir,q}(\Omega_0) = \frac{1 - \varpi^* \cdot \mathbf{pt}_{bs}^{dir}(\Omega_0)}{1 - \varpi_\lambda \cdot \mathbf{pt}_{bs}^{dir}(\Omega_0)} \mathbf{t}_{bs}^{dir^*,q}(\Omega_0) \tag{174}$$

$$\mathbf{t}_{bs,\lambda}^{diff,q}(\Omega_0) = \frac{1 - \varpi^* \cdot \mathbf{pt}_{bs}^{diff}(\Omega_0)}{1 - \varpi_\lambda \cdot \mathbf{pt}_{bs}^{diff}(\Omega_0)} \mathbf{t}_{bs}^{diff^*,q}(\Omega_0) \tag{175}$$

$$\mathbf{t}_{bs,\lambda}^{dir,q\equiv1}(\Omega_0) = \frac{1 - \varpi^* \cdot \mathbf{pt}_{bs}^{dir}(\Omega_0)}{1 - \varpi_\lambda \cdot \mathbf{pt}_{bs}^{dir}(\Omega_0)} \mathbf{t}_{bs}^{dir^*,q\equiv1}(\Omega_0) \tag{176}$$

$$\mathbf{t}_{bs,\lambda}^{diff,\,q\equiv1}(\Omega_0) = \frac{1-\varpi^* \cdot \mathbf{pt}_{bs}^{diff}(\Omega_0)}{1-\varpi_\lambda \cdot \mathbf{pt}_{bs}^{diff}(\Omega_0)}\mathbf{t}_{bs}^{diff^*,\,q\equiv1}(\Omega_0) \tag{177}$$

$$\mathbf{t}_\lambda^q = \frac{1-\varpi^* \cdot \mathbf{pt}}{1-\varpi_\lambda \cdot \mathbf{pt}}\mathbf{t}^{q*} \tag{178}$$

$$\mathbf{a}_{bs,\lambda}^{dir}(\Omega_0) = \frac{1-\varpi^* \cdot \mathbf{pa}_{bs}}{1-\varpi_\lambda \cdot \mathbf{pa}_{bs}} \cdot \frac{1-\varpi_\lambda}{1-\varpi^*}\mathbf{a}_{bs}^{dir*}(\Omega_0) \tag{179}$$

$$\mathbf{a}_{bs,\lambda}^{diff}(\Omega_0) = \frac{1-\varpi^* \cdot \mathbf{pa}_{bs}}{1-\varpi_\lambda \cdot \mathbf{pa}_{bs}} \cdot \frac{1-\varpi_\lambda}{1-\varpi^*}\mathbf{a}_{bs}^{diff*}(\Omega_0) \tag{180}$$

$$\mathbf{a}_\lambda^q = \frac{1-\varpi^* \cdot \mathbf{pa}}{1-\varpi_\lambda \cdot \mathbf{pa}} \cdot \frac{1-\varpi_\lambda}{1-\varpi^*}\mathbf{a}^{q*} \tag{181}$$

where ϖ_λ is the spectral leaf albedo and $\mathbf{pt}_{bs}^{dir}$, $\mathbf{pt}_{bs}^{diff}$, $\mathbf{pt}$, $\mathbf{t}_{bs}^{dir,\,q*}$, $\mathbf{t}_{bs}^{diff,\,q*}$, $\mathbf{t}_{bs}^{dir^*,\,q\equiv1}$, $\mathbf{t}_{bs}^{diff^*,\,q\equiv1}$, $\mathbf{t}^{q*}$, $\mathbf{a}_{bs}^{dir*}$, $\mathbf{a}_{bs}^{diff*}$, $\mathbf{a}^{q*}$, $\mathbf{pa}_{bs}$, and $\mathbf{pa}$ are 13 model canopy coefficients which depend only on canopy structure (i.e., biome type, LAI, etc.) and not on wavelength or soil type. Those with asterisks indicate that they are evaluated at a leaf albedo value of ϖ^* (or, equivalently, at a wavelength with that value of leaf albedo) which is currently configured to a value of 0.02.

These 13 wavelength and soil independent canopy absorption and transmission parameters, along with the spectral leaf albedo ϖ_λ and the spectral soil reflectance patterns $\rho_{eff,\lambda}^q$, are also archived in the CART for reference purposes.

6.5.3.11 Biome parameters used in modeling the CART file

The canopy model parameter types and associated values for each biome class, used to compute the contents of the CART file, are listed in Table 11.

Table 11: Biome Canopy Model Parameters

Parameter	Grasses/ Cereal Crops	Shrublands	Broadleaf Crops	Savanna	Leaf Forests	Needle Forests
Plant LAI	0 - 7	0 - 7	0 - 7	0 - 7	0 - 7	0 - 7
Fractional Ground Cover	1.0	0.2 - 0.6	0.1 - 1.0	0.2 - 0.4	> 0.8	> 0.7
Understory LAI	n/a	n/a	n/a	0 - 5	0 - 2	0 - 2

Table 11: Biome Canopy Model Parameters (continued)

Parameter	Grasses/ Cereal Crops	Shrublands	Broadleaf Crops	Savanna	Leaf Forests	Needle Forests
Leaf Normal Orientation	erectophile	uniform	uniform	uniform/ erectophile	uniform/ planophile	uniform/ planophile
Stems, Trunks & Branches	n/a	5%	10%	10%	15 - 20%	15 - 20%
Leaf Size (m)	0.05	0.05	0.10	n/a	n/a	n/a
Crown Size (m)	n/a	n/a	n/a	4x2 8x4	6x4 12x8	4x2 8x4
Reference Leaf Albedo	0.1	0.1	0.1	0.1	0.1	0.1
Solar Zenith Angle (deg)	15 - 75	15 - 75	15 - 75	15 - 75	15 - 75	15 - 75
View Zenith Angle (deg)	15-75	15-75	15-75	15-75	15-75	15-75
View Azimuth Angle (deg)	0-180	0-180	0-180	0-180	0-180	0-180

Leaf water content in all cases was 0.025 m and leaf optical properties were simulated with the PROSPECT model *[32]*. For savanna, leaf forests, and needle forests fractional ground cover refers to the overstory, a range of LAI (0 - 3) was also considered for their understory, and the two leaf normal orientations in these biomes refer to over-and understory. The trunk, stem, and branch fractions are fraction of the canopy LAI and their optical properties are averages of those reported for boreal canopies.

6.5.4   Calculate NDVI-FPAR regression coefficients

Although the cause and effect relation between FPAR and NDVI can be established theoretically, its utility depends on its sensitivity to biome characteristics. For example, if all biomes have a similar or nearly similar NDVI-FPAR relationship, information on global land cover would be unnecessary when using such relationships for the estimation of FPAR. Since this clearly is not the case, we must first stratify the global land cover into biome types that have sufficiently different NDVI-FPAR relationships. This implies that traditional land cover classifications, based on botanical, ecological or functional metrics, may be unsuitable for FPAR estimations *[42]*. Therefore, a land cover classification that is compatible with the FPAR algorithm is embodied in the Biome Classification Map.

Based on Eq. (159), the canopy models summarized in Table 11, and the soil properties listed

in Table 12, directional-hemispherical reflectances in the red and near IR, and PAR absorptance were computed to derive simulated NDVI-FPAR relationships for each biome type.

Table 12: Soil Model Parameters for FPAR-NDVI Regression

| Parameter	Grasses/ Cereal Crops	Shrublands	Broadleaf Crops	Savanna	Leaf Forests	Needle Forests
Soil Type c=clay, s=sand	60c + 40s	20c + 80s	80c + 20s	60c + 40s	60c + 40s	60c + 40s
Reflectance	medium	bright	dark	medium	medium	medium

These relationships are shown in Figure 11, using base case values for the model canopy parameters (base case implies a typical value within the range of values specified in Table 11). In this figure, the notation "Bn" refers to Biome n, where n has the same numbering convention as *bio*. The abbreviation "ulai" refers to understory LAI. From these relationships, regression coefficients, F_0 and F_1, were derived for each biome type and dependent on solar zenith angle, such that

$$FPAR(bio, \mu_0) = F_0(bio, \mu_0) + F_1(bio, \mu_0) \cdot NDVI \tag{182}$$

Here, NDVI is defined as

$$NDVI = \frac{A_{NIR}^{dir} - A_{red}^{dir}}{A_{NIR}^{dir} + A_{red}^{dir}} \tag{183}$$

where A_{NIR}^{dir} and A_{red}^{dir} are DHR's in the near IR and red bands, respectively.
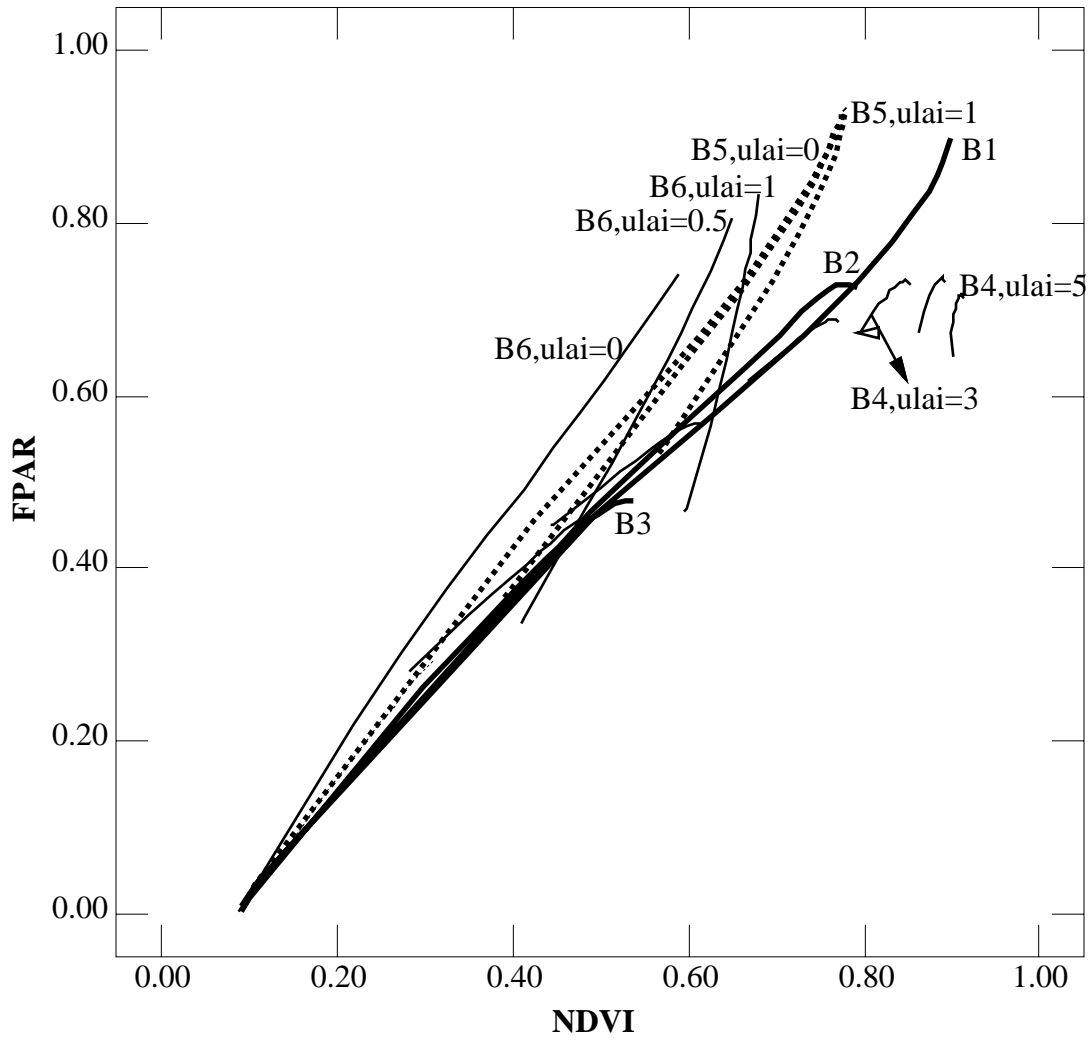
Figure 11. Relationships between FPAR and at-surface NDVI in the base case simulation

7. REFERENCES

[1] Andreae, M.O. (1995). Climatic effects of changing atmospheric aerosol levels. In *World Survey of Climatology* **16**, *Future Climates of the World*, A. Henderson-Sellers, ed., Elsevier, Amsterdam.

[2] Baret, F., S. Jacquemoud, and J.F. Hanocq (1993). The soil concept in remote sensing. *Remote Sens. Rev*., **7**, 65-82.

[3] Bass, L.P., A.M. Volocsvhenko, and T.A. Germogenova (1986). *Methods of Discrete Ordinates in Radiation Transport Problems*. Inst. Appl. Mathem., the USSR Academy of Sci., Moscow, 231 pp. (in Russian, with English abstract).

[4] Baum, B., B. Wielicki, P. Minnis, and L. Parker (1992). Cloud-property retrieval using merged HIRS and AVHRR data. *J. Appl. Met.* **31**, 351-369.

[5] Begue, A. and R.B. Myneni (1996). Relationships between NOAA-AVHRR vegetation indices and daily FAPAR established for sahelian vegetation canopies. *J. Geophys. Res*. (submitted, September 1995).

[6] Bortkovskii, R. S. (1987). *Air-Sea Exchange of Heat and Moisture During Storms.* Reidel, Dordrecht.

[7] Chandrasekhar, S. (1960). *Radiative Transfer*. Dover Publications, Inc., New York.

[8] Charlson, R.J., J. Langner, H. Rodhe, C.B. Leovy, and S.G. Warren (1991). Perturbation of the northern hemispheric radiative balance by backscattering from anthropogenic sulfate aerosols. *Tellus* **43AB**, 152-163.

[9] Clarke, A.D., and J.N. Porter (1991). Aerosol size distribution, composition, and CO_2 backscatter at Mauna Loa observatory. *J. Geophys. Res.* **96**, 5237-5247.

[10] Cox, C. and W. Munk (1954). Measurements of the roughness of the sea surface from photographs of the Sun's glitter. *J. Opt. Soc. of Am.* **44**, 838.

[11] d'Almeida, G. A., P. Koepke, and E. P. Shettle (1991). Atmospheric Aerosols: Global climatology and radiative characteristics. Deepak Publishing.

[12] Deshler, T., D.J. Hoffman, B.J. Johnson, and W.R. Rozier (1992). Balloonborne measurements of the Pinatubo aerosol size distribution and volatility at Laramie, Wyoming during the summer of 1991. *Geophys. Res. Lett.* **19**, 199-202.

[13] Diner, D.J. and J.V. Martonchik (1984a). Atmospheric transfer of radiation above an inhomogeneous non-lambertian reflective ground. I. Theory. *J. Quant. Spect. Rad. Trans*. **31**, 97-125.

[14] Diner, D.J. and J.V. Martonchik (1984b). Atmospheric transfer of radiation above an inhomogeneous non-lambertian reflective ground. II. Computational considerations and results. *J. Quant. Spect. Rad. Trans*. **32**, 279-304.

[15] Diner, D.J. and J. V. Martonchik (1985). Influence of aerosol scattering on atmospheric blurring of surface features. *IEEE Trans. Geosci. and Rem. Sens*. **GE-23**, 618.

[16] Dowling, D.R. and L.F. Radke (1990). A summary of the physical properties of cirrus clouds. *J. Appl. Met.* **29**, 970-978.

[17] Ferrare, R.A., R.S. Fraser, and Y.J. Kaufman (1990). Satellite measurements of large-scale air pollution: Measurements of forest fire smoke. *J. Geophys. Res.* **95**, 9911-9925.

[18] Germogenova, T.A. (1986). *The Local Properties of the Solution of the Transport Equation*. Nauka, Moscow, 272pp. (in Russian).

[19] Gordon, H.R. (1994). MODIS Normalized Water-leaving Radiance Algorithm Theoretical Basis Document (MOD 18), Version 2.

[20] Gordon, H.R. and M. Wang (1994a). Retrieval of water-leaving radiance and aerosol optical thickness over the oceans with SeaWiFS: A preliminary algorithm. *Appl. Opt.* **33**, 443-452.

[21] Gordon, H.R. and M. Wang (1994b). Influence of oceanic whitecaps on atmospheric correction of SeaWiFS. *Appl. Opt.* **33**, 7754-7763.

[22] Grant, I.P. and G.E. Hunt (1968). Solution of radiative transfer problems using the invariant S_n method. *Mon. Not. Roy. Astron. Soc.* **141**, 27-41.

[23] Gregg, W. W. and K.L. Carder (1990). A simple spectral solar irradiance model for cloudless maritime atmospheres. *Limnol. Oceanogr.* **35**, 1657.

[24] Hanel, G. (1976). The properties of atmospheric aerosol particles as functions of relative humidity at thermodynamic equilibrium with the surrounding moist air. *Adv. Geophys.* **19**, 73.

[25] Hansen, J. E. and L. D. Travis (1974). Light scattering in planetary atmospheres. *Space Sci. Rev.* **16**, 527.

[26] Hegg, D., T. Larson, and P-F. Yuen (1993). A theoretical study of the effect of relative humidity on light scattering by tropospheric aerosols. *J. Geophys. Res.* **98**, 18,435-18,439.

[27] Hofmann, D.J. (1990). Increase in the stratospheric background sulfuric acid aerosol mass in the past 10 years. *Science* **248**, 996-1000.

[28] Holben, B.N., T.F. Eck, I. Slutsker, D. Tanre, J.P. Buis, A. Setzer, E. Vermote, J.A. Reagan, and Y.A. Kaufman (1994). Multi-band automatic sun and sky scanning radiometer system for measurement of aerosols. *Sixth International Symposium on Physical Measurements and Sig-*

natures in Remote Sensing, p. 9.

[29] Hsiung, J. (1986). Mean surface energy fluxes over the global ocean. *J. Geophys. Res.* **C91**, 10585.

[30] Husar, R.B., L.L. Stowe, and J. Prospero (1996). Patterns of Tropospheric aerosols. Submitted to *Bull. Amer. Meteor. Soc.*

[31] Ignatov, A.M., L.L. Stowe, S.M. Sakerin, and G.K. Korotaev (1995). Validation of the NOAA/NESDIS satellite aerosol product over the north atlantic in 1989. *J. Geophys. Res*. **100**, 5123-5132

[32] Jacquemoud, S. and F.Baret (1990). PROSPECT: A model of leaf optical properties spectra. *Remote Sens. Environ.* **34**, 75-91.

[33] Jacquemoud, S, F. Baret, and J.F. Hanocq (1992). Modeling spectral and bidirectional soil reflectance. *Remote Sens. Environ.* **41**, 123-132.

[34] Kaufman, Y. J. (1984). Atmospheric effect on spatial resolution of surface imagery: errata. *Appl. Opt.* **23**, 4164-4172.

[35] Kiehl, J.T., and B.P. Briegleb (1993). The relative roles of surface aerosols and greenhouse gases in climate forcing. *Science* **260**, 311-314.

[36] Knyazikhin, Yu. and A. Marshak (1991). Fundamental equations of radiative transfer in leaf canopies and iterative methods for their solution, In: R.B. Myneni and J. Ross (Editors), *Photon-Vegetation Interactions: Applications in Plant Physiology and Optical Remote Sensing*. Springer-Verlag, Berlin, pp. 9-43.

[37] Knyazikhin, Yu., G. Mießen, O. Panfyorov, and Gravenhorst (1997). Small-scale study of three-dimensional distribution of photosynthetically active radiation in a forest. *Agric. For. Meteorol* (in press).

[38] Koepke, P. (1984). Effective reflectance of oceanic whitecaps. *Appl. Opt.* **23**, 1816.

[39] Kranigk, J. (1996). *Ein Model für den Strahlungstransport in Fichtenbeständen*. Cuvillier Verlag, Goettingen, 127pp. (in German).

[40] Li, X. and A.H. Strahler (1992). Geometrical-optical bidirectional reflectance modeling of the discrete crown vegetation canopy: Effect of crown shape and mutual shadowing. *IEEE Trans. Geosci. Remote Sens.* **30**, 276-292.

[41] Long, C. S., and L. L. Stowe (1994). Using the NOAA/AVHRR to study stratospheric aerosol optical thickness following the Mt. Pinatubo eruption. *Geophys. Res. Lett.* **21**, 2215-2218.

[42] Loveland, T.R., J.W. Merchant, D.O. Ohlen, and J.F. Brown (1991). Development of a

land cover characteristic data base for the conterminous U.S. *Photogramm. Eng. and Remote Sens*. **57**, 1453-1463.

[43] Merrill, J., E. Arnold, M. Leinin, and C. Weaver (1994). Mineralogy of aeolian dust reaching the North Pacific Ocean 2. Relationship of mineral assemblages to atmospheric transport patterns. *J. Geophys. Res.* **99**, 21025-21032.

[44] Minnis, P., P.W. Heck, and D.F. Young (1993). Inference of cirrus cloud properties using satellite-observed visible and Infrared radiances. Part II: Verification of theoretical cirrus radiative properties. *J. Atmos. Sci.* **50**, 1305-1322.

[45] Mishchenko, M. I. and L. D. Travis (1994). Light scattering by polydispersions of randomly oriented spheroids with sizes comparable to wavelengths of observation. *Appl. Opt.* **33**, 7206-7225.

[46] Mishchenko, M. I. and L. D. Travis (1996). Satellite retrieval of aerosol properties over the ocean using polarization as well as intensity of reflected sunlight. *J. Geophys. Res*. **102**, 16,989-17,013.

[47] Mishchenko, M. I., L. D. Travis, R. A. Kahn, and R. A. West (1996). Modeling phase functions for dust-like tropospheric aerosols using a shape mixture of randomly oriented polydisperse spheroids. *J. Geophys. Res*. **102**, 16,831-16,847.

[48] Monahan, E. C. (1971). Oceanic whitecaps. *J. Phys. Oceanogr.* **1**, 139.

[49] Monahan, E. C. and I. G. O'Muircheartaigh (1980). Optimal power-law description of oceanic whitecap coverage dependence on wind speed. *J. Phys. Oceanogr.* **10**, 2094.

[50] Myneni, R.B. (1991). Modeling radiative transfer and photosynthesis in three-dimensional vegetation canopies. *Agric. For. Meteorol*. **55**, 323-344.

[51] Myneni, R.B., G. Asrar, and F.G. Hall (1992). A three-dimensional radiative transfer method for optical remote sensing of vegetated land surfaces. *Remote Sens. Environ.* **41**, 105-121.

[52] Myneni, R.B., S. Maggion, J. Iaquinta, J.L. Privette, N. Gobron, B. Pinty, D.S. Kimes, M.M. Verstraete, and D.L. Williams (1995). Optical remote sensing of vegetation: Modeling, caveats, and algorithm. *Remote Sens. Environ.* **51**, 169-188.

[53] Nicodemus, F. E., J. C. Richmond, J. J. Hsia, I. W. Ginsberg, and T. Limperis (1977). *Geometrical Considerations and Nomenclature for Reflectance*, NBS Monograph **160**, National Bureau of Standards, U.S. Department of Commerce, Washington, D.C.

[54] O'Dowd, C.D., and M.H. Smith (1993). Physicochemical properties of aerosols over the northeast Atlantic: Evidence for wind-speed-related submicron sea-salt aerosol production. *J. Geophys. Res.* **98**, 1137-1149.

[55] Oker-Blum, P., J. Lappi, and H. Smolander (1991). Radiation regime and photosynthesis of coniferous stands. In *Photon Vegetation Interactions*, Myneni and Ross, eds., Springer-Verlag, Berlin, Germany, pp.501-535.

[56] Penner, J.E., R.E. Dickinson, and C.A. O'Neill (1992). Effects of aerosol from biomass burning on the global radiation budget. *Science* **256**, 1432-1434.

[57] Pinty, B., M. M. Verstraete, and R.E. Dickinson (1989). A physical model for predicting bidirectional reflectances over bare soils. *Remote Sens. Environ*. 27, 273-288.

[58] Pokrowski, G.I.(1929). Über die Helligkeitsverteilung am Himmel. *Physikal. Zeitschr*. **30**, 697-700 (in German).

[59] Privette, J.L. (1994). An efficient strategy for the inversion of bidirectional reflectance models with satellite remote sensing data. Ph.D. Thesis, University of Colorado, Boulder.

[60] Privette, J.L., R.B. Myneni, W.L. Emery, and C.J. Tucker (1994). Invertibility of a 1 D discrete ordinates canopy reflectance model. *Remote Sens. Environ.* **48**, 89-105.

[61] Pruppacker, H.R., and J.D. Klett (1978). Microphysics of Clouds and Precipitation, D. Reidel, pp.714.

[62] Rao, C.R.N., L.L. Stowe, and E.P. McClain (1989). Remote sensing of aerosols over the oceans using AVHRR data: Theory, practice and applications. *Int. J. Remote Sensing* **10**, 743-749.

[63] Ross, J. (1981). *The Radiation Regime and Architecture of Plant Stands*. Dr. W. Junk Publ., The Hague, The Netherlands, 391pp.

[64] Ross, J. and T. Nilson (1968). A mathematical model of radiation regime of plant cover, In: *Actinometry and Atmospheric Optics*. Valgus. Tallin (in Russian).

[65] Ross, J., Yu. Knyazikhin, A. Kuusk, A. Marshak, and T. Nilson (1992). *Mathematical Modeling of the Solar Radiation Transfer in Plant Canopies*. Gidrometeoizdat, St. Peterburg,195pp.(in Russian, with English abstract).

[66] Russell, P.B., T.J. Swissler, M.P. McCormick, W.P. Chu, J.M. Livingston, and T.J. Pepin (1981). Satellite and correlative measurements of the stratospheric aerosol II: Comparison of measurements made by SAM II, dustsondes, and an airborne lidar. *J. Atmos. Sci.* **38**, 1295-1302.

[67] Russell, P.B., M.P. McCormick, T.J. Swissler, J.M. Rosen, D.J. Hoffmann, and L.R. McMaster (1984). Satellite and correlative measurements of the stratospheric aerosol III: A Comparison of measurements by SAMII, SAGE, dustsondes, filters, impactors and lidar. *J. Atmos. Sci.* **41**, 1791-1800.

[68] Russell, P.B., J.M. Livingston, E.G. Dutton, R.F. Pueschel, J.A. Reagan, T.E. DeFoor,

M.A. Box, D. Allen, P. Pilewskie, B.M. Herman, S.A. Kinne, and D.J. Hoffman (1993). Pinatubo and Pre-Pinatubo optical depth spectra: Mauna Loa measurements, compositions, inferred particle size distributions, radiative effects, and relationship to LIDAR data. *J. Geophys. Res.* **98**, 22,969-22,985.

[69] Shettle, E.P. and R.W. Fenn (1979). Models for the aerosols of the lower atmosphere and the effects of humidity variations on their optical properties. Air Force Geophysics Laboratory, Hanscomb AFB, MA 01731, AFGL-TR-79-0214.

[70] Shultis, J.K. and R.B. Myneni (1988). Radiation transfer in vegetation canopies with anisotropic scattering. *J. Quant. Spectrosc. Radiat. Transfer* **39**, 115-129.

[71] Stowe, L.L., R.M. Carey, and P.P. Pellegrino (1992). Monitoring the Mt. Pinatubo aerosol layer with NOAA/11 AVHRR data. *Geophys. Res. Lett.* **19**, 159-162.

[72] Svenningsson, I.B., H.-C. Hansson, and A. Wiedensohler (1992). Hygroscopic growth of aerosol particles in the Po Valley. *Tellus* **44B**, 556-569.

[73] Mishchenko, M.I., W.B. Rossow, A. Macke, and A.A. Lacis (1996). Sensitivity of cirrus cloud albedo, bidirectional reflectance and optical thickness retrieval accuracy to ice particle shape. *J. Geophys. Res.* **101**, 16973-16985.

[74] Tarrason, L., and T. Iversen (1992). The influence of north American anthropogenic sulphur emissions over western Europe. *Tellus* **44B**, 114-132.

[75] Tegen, I., and I. Fung (1994). Modeling of mineral dust in the atmosphere: Sources, transport, and optical thickness. *J. Geophys. Res.* **99**, 22897-22914.

[76] Tegen, I., and I. Fung (1995). Contribution to the atmospheric mineral aerosol load from land surface modification. *J. Geophys. Res.* **100**, 18707-18726.

[77] van de Hulst, H. C. (1980). *Multiple light scattering*. Academic Press, NY, 739 pp.

[78] Vladimirov, V.V. (1963). Mathematical problems in the one-velocity theory of particle transport. AECL-1661, Chalk, River, Ontario, Canada.

[79] Wang, P.-H., M.P. McCormick, L.R. McMaster, W.P. Chu, T.J. Swissler, M.T. Osborn, P.B. Russell, V.R. Oberbeck, J. Livingston, J.M. Rosen, D.J. Hoffman, G.W. Grams, W.H. Fuller, and G.K. Yue (1989). SAGE II data validation based on retrieved aerosol model size distribution from SAGE II aerosol measurements. *J. Geophys. Res.* **94**, 8381-8393.

[80] Wang, M. (1991). Atmospheric corrections of the second generation ocean color sensors. Ph. D. dissertation, Univ. of Miami, FL.

[81] World Climate Programme WCP-112 (1984). A Preliminary Cloudless Standard Atmo-

sphere for Radiation Computation. IAMAP (International Association for Meteorology and Atmospheric Physics), Boulder, CO, pp.53.